ALLOSTERIC CONTROL OF FUNCTIONAL LINKERS

ALLOSTERIC MECHANISMS FOR THE cAMP-DEPENDENT CONTROL OF FUNCTIONAL INTER-DOMAIN LINKERS

By MADOKA AKIMOTO, M.S.

A Thesis Submitted to

the School of Graduate Studies in Partial Fulfilment

of the Requirements for

the Degree Doctor of Philosophy

McMaster University © Copyright by Madoka Akimoto, September 2015

Doctor of Philosophy (2015) **McMaster University**

(Chemical Biology) **Hamilton, Ontario**

Thesis Title: ALLOSTERIC MECHANISMS FOR THE cAMP DEPENDENT CONTROL OF FUNCTIONAL INTER-DOMAIN LINKERS

Abbreviated title: ALLOSTERIC CONTROL OF FUNCTIONAL LINKERS

Author: Madoka Akimoto, M.S. (University of Tokyo)

Supervisor: Professor Giuseppe Melacini

Number of Pages: xiv, 152

Lay Abstract:

Cyclic adenosine monophosphate or cAMP is a second messenger that is produced by cells to control the internal cellular metabolism in response to external stimuli. The goal of this thesis is to elucidate the structural and dynamical changes that translate the cAMP signal into a specific biological response necessary for the survival of the cell. We used Nuclear Magnetic Resonance (NMR) Spectroscopy to investigate how, under physiological solution conditions, the cAMP interacts with and modifies the cAMP-dependent protein kinase A (PKA) and the hyperpolarization-activated and cyclic nucleotide-gated channels (HCN). Knowledge of both structure and dynamics on both proteins is required in order to fully understand at a molecular level how cAMP works in the human heart. The elucidation of the structural and dynamical changes associated with cAMP-binding is expected to help define general rules applicable to the design of drugs for cardiovascular disorders.

Thesis Abstract:

The activation of Protein Kinase A (PKA) and of Hyperpolarization-activated and Cyclic Nucleotide-modulated channels (HCN) is controlled by cAMP through cAMP binding domains (CBDs), which serve as cAMP-dependent conformational switches to regulate downstream signaling pathways. The binding of the cAMP allosteric effector removes the auto-inhibition imposed by linkers that are adjacent to the CBDs of PKA and HCN. However, our understanding of how cAMP binding to the structured CBD controls the adjacent inhibitory linkers is currently limited. Herein, we investigate through NMR spectroscopy the interactions between the CBDs of HCN and PKA and the respective adjacent linkers. Chapters 2 and 3 of this thesis focus on the linkers N-terminal to PKA CBD-A and CBD-B, respectively, while Chapter 4 centers on the linker N-terminal to the HCN CBD. We show that in the case of PKA the linker N-terminal to CBD-A is flexible, but is coupled to the CBD-A through state active selective interactions. In the case of the CBD-B of PKA the state selective interactions with the linker N-terminal to it are to a large extent lost and replaced by state-selective inter-CBD interactions, which in turn control the conformational ensemble accessible to the inter-domain linker. Unlike PKA, in the case of HCN, the primary mechanism of cAMP-dependent linker control is through the state-selective destabilization of the structured tetrameric N-terminal linker. Overall, this thesis reports three distinct mechanisms through which linkers in HCN and PKA serve not only as simple covalent threads, but also as integral parts of the allosteric networks underlying auto-inhibition and cAMP dependent activation.

Acknowledgements:

First and foremost, I would like to express my deepest appreciation to Dr.Melacini, who guided me over the past few years with lots of patience and kindness. I am truly grateful for the opportunity that you gave me and the support that you provided me all the time.

To my committee members, Dr.Junop and Dr.Bishop. I will never forget the day you two gave me a big hug and advised me about the life. All the time, your suggestion and advice gave me a guide for the next steps in my projects.

I would like to express my gratitude towards the past and present lab members: Tyler, Julijana, Rajeevan, Geeta, Shruti, Moustafa, Bryan, Stephen, Melanie, Kody, Naeimeh, Avinash, Maryam, Olivia. Thank you for your friendship and support. I really enjoyed working with you.

To my mother Keiko Akimoto and father Akira Akimoto. Thank you for giving me the support that I needed it most. I could never find my way without your love and encouragement.

Lastly, I would like to say a big thank you to my husband, Takahiro. I could not have accomplished this without you.

Table of Contents

Chapter 2

Chapter 3

Chapter 4

Chapter 5

List of Figures

Chapter 1: General Introduction

Chapter 2: C-Linker Control by the PKA RIα CBD-A

Chapter 3: Inter-CBD Linker Control by the PKA RIα CBD-B

Chapter 4: Intracellular Linker Control by the HCN4 CBD

Chapter 5: Conclusions and Future Perspectives

List of Supplementary Figures

Chapter 2: C-Linker Control by the PKA RIα CBD-A

List of Tables

List of Abbreviations

BBR	base binding region
C	Catalytic subunit
cAMP	adenosine 3’5’ cyclic monophosphate
CBD	cyclic-AMP binding domain
CHESCA	chemical shift covariance analysis
CHESPA	chemical shift projection analysis
CPMG	Carr Purcell Meiboom Gill pulse sequence
cNTs	cyclic-nucleotides (cAMP and cGMP)
D/D	Dimerization docking domain
eCBD	Extended CBD
EPAC	exchange protein activated by cAMP
GPCR	G-protein coupled receptor
HCN	hyperpolarization modulated and cyclic-nucleotide gated
H/D	Hydrogen/Deuterium Exchange
H/H	Hydrogen/Hydrogen Exchange
HSQC	Hetero-nuclear single quantum coherence
IR	Intracellular region
IS	Inhibitor site
MD	molecular dynamics
NTHB	N terminal Helical Bundle
NMR	nuclear magnetic resonance
NOE	Nuclear Overhauser Effect
PKA	protein kinase A
PBC	Phosphate binding cassette
PF	Protection Factor
PRE	Paramagnetic Relaxation Enhancement
R	Regulatory subunit
RA	RIα(91-244)
RMSD	Root Mean Square Deviation
SASA	Solvent Accessible Surface Area
SI	Supplementary information
SVD	Singular value decomposition
STD	Saturation transfer difference
TR	Transmembrane region

Chapter 1

General Introduction

1.1 Physiology of cAMP Signalling

1.1.1 cAMP-Dependent Signalling Pathways and Allostery

Cell-to-cell communication relies on the conversion of extracellular stimuli into tightly regulated intracellular responses. A key step in this transduction process is the relay of the external signals by second messengers, including cAMP (Figure 1). cAMP acts by binding to regulatory proteins and causing conformational changes that modulate specific cellular functions, but the conformational switches controlled by cAMP are only partially understood despite their critical relevance for the treatment of cardiovascular and neuronal disorders (1–5). Increased intracellular cAMP concentrations are generated in response to hormones stimulating numerous G-protein-coupled receptors that activate adenylyl cyclase (Figure 1). In mammals, a pivotal receptor for cAMP is the archetypical cAMP-dependent protein kinase (PKA) (6). However, cAMP also functions independently of PKA by activating two other major

and more recently discovered cAMP-receptors, i.e. the hyperpolarization-activated and cyclic nucleotide-gated ion channels (HCN) (7), which generate cardiac and neuronal electrical rhythmicity, and the exchange protein activated by cAMP (EPAC) (2, 8, 9), which is a guanine-nucleotide-exchange factor (Figure 1). PKA, HCN and EPAC together mediate the majority of cAMP responses (10, 11), and regulate multiple cellular processes ranging from ion-channel gating to cell growth and adhesion that in turn control major physiological

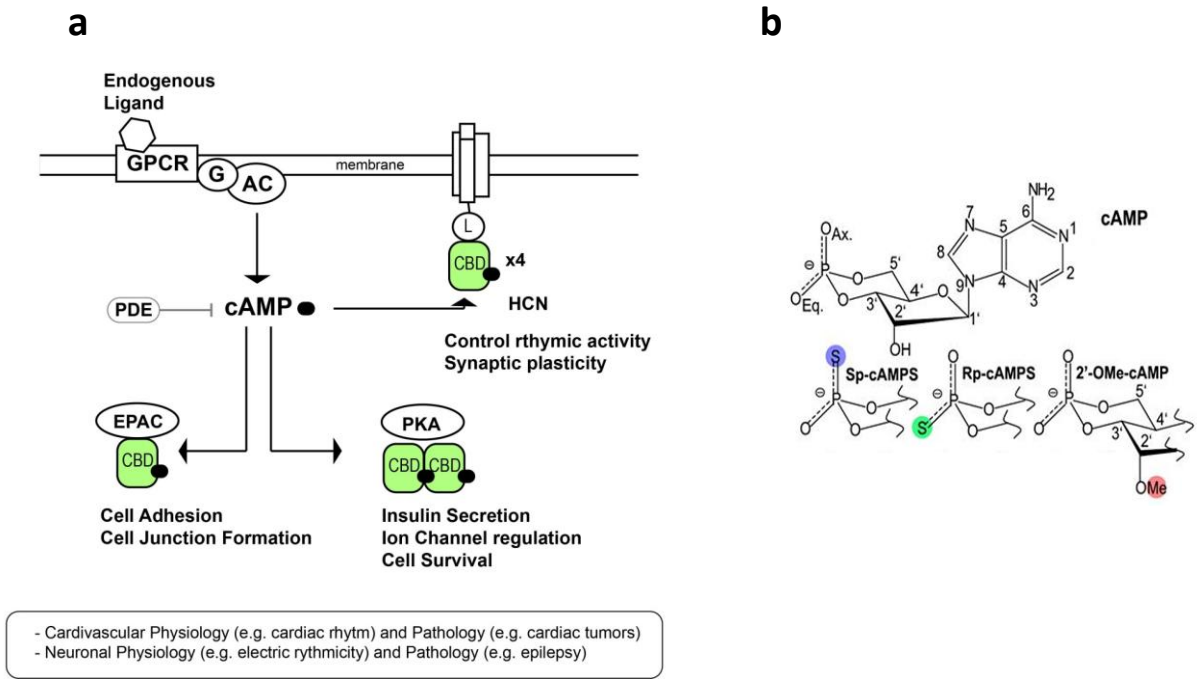

Figure 1: a) Simplified scheme illustrating cyclic-nucleotide mediated signalling. cAMP is generated through the binding of a primary messenger molecule to a G-protein coupled receptor (GPCR), which in turn activates the α-subunit of the G-protein that binds adenylyl cyclase (AC). AC catalyzes the conversion of ATP into cAMP. The cAMP-Binding Domain (CBDs) are highlighted in green. This thesis focuses on the CBDs of PKA and HCN. b) Covariance structure of cAMP and related modification of cAMPwas adapted and modified from Selvaratnam et al. (2011), ref 32

phenotypes (2, 7, 10, 12). For example, cAMP plays a key role in the chain of reactions by which the β-adrenergic agonists affect the rate of the heart beat (1, 13, 14). Cardiac pacemaker activity is controlled by the intracellular Ca^{2+}clock and the surface membrane voltage clock (15). PKA is a key regulator of the former (16–18), while HCN is part of the latter

(10, 19). The cAMP-mediated activation of PKA by epinephrine results in the phosphorylation of troponin-I, which alters the cardiac relaxation, and of phospholamban, which shortens the contraction period (1, 20). In addition, cAMP activates EPAC and HCN as well. EPAC activation stimulates Ras proteins that induce myocyte hypertrophy (21), while HCN channel opening promotes the acceleration of the cardiac rhythm (7). Given the central role of the allosteric control by cAMP in cardiovascular physiology, defective cAMP-dependent allostery is expected to lead to cardiovascular pathology. For example, incorrect cAMP signal translation by PKA and EPAC has been linked to acute ischemic stress, cardiac tumors and cardiac hypertrophy (16–18), while several HCN mutations are known to cause arrhythmias (10, 19).

1.1.2 Pharmacological Relevance of Allostery in Drug Design

Traditional drug discovery efforts, either through screening or rational drug design, have often focused on targeting the binding sites for classical endogenous ligands (i.e. orthosteric sites), or the actual pore of channels. However, in the past decade the drug discovery focus has shifted towards allosteric sites because, compared to orthosteric sites, they enhance the selectivity for therapeutic targeting (22–26). Orthosteric sites are subject to evolutionary pressure and hence exhibit a highly specific function. Therefore, inhibitors targeting orthosteric sites often bind without selectivite at multiple homologous targets within the same protein family, resulting in poor efficacy. In contrast, drugs targeting allosteric sites are likely to exhibit higher selectivity, given the lesser evolutionary pressure for conservation at loci remote from the active sites (22, 23). In addition, other allosteric *versus* orthosteric site advantages are that the former are less affected than the latter by mutations leading to drug

resistance and often they do not require the competitive displacement of endogenous ligands by potential drug leads (26).

1.1.3 Tapping the Pharmacological Potential of cAMP Signalling Through a Comprehensive Approach to Human cAMP Receptors

Allosteric *versus* orthosteric targeting is a promising approach also for tapping the pharmacological potential of cAMP-receptors in humans, i.e. PKA, HCN and EPAC. For example, in the case of PKA inhibition, the competitive inhibitor H89, which binds directly to the highly conserved catalytic site of PKA (27), inhibits several other kinases causing multiple side-effects that are absent when PKA inhibition is obtained through allosteric inhibitors. These include cAMP analogs that target more selectively less conserved sites of PKA, such as those in the cAMP-Binding Domains (CBDs). As a result, hundreds of cAMP analogs have been screened for PKA antagonism (28), but to date the only known cAMP antagonist in PKA is the Rp-cAMPS phosphorothioate analog of cAMP.

Targeting of other cAMP-dependent signalling systems is likely to benefit from the added selectivity offered by allosteric sites. For example, the HCN channel pore-binding drug, ivabradine, which is used for the symptomatic management of stable angina pectoris (29), is associated with side effects in luminous phenomena due to poor selectivity. These examples illustrate the therapeutic potential of targeting the allosteric sites in the cAMP-binding domains (CBD) of human cAMP-receptors. However, the CBD is itself a ubiquitous conformational switch (Figure. 1). The ubiquity of the CBD opens a wide range of therapeutic opportunities, but at the same time it also poses a major selectivity challenge. In order to tap the pharmaceutical

potential of the CBD, it is therefore critical to comparatively analyze eukaryotic CBDs. A comprehensive map of the allosteric hot spots that are unique to each CBD will aid in the design of novel therapeutics targeting PKA, HCN and EPAC.

1.1.4 Comparative Analysis of Human cAMP-Binding Domains (CBDs) to Explore Selectivity Options despite Structural Homology

The elucidation of the molecular basis for selective drug targeting requires the full clarification at a structural and dynamical level of how the cAMP signal is translated by HCN, PKA and EPAC. Each protein alone would not be able to fully account for the complex regulatory effects of cAMP. To understand the structural and dynamical basis for the translation of the cAMP-signal by HCN and PKA with the purpose of developing comprehensive models of cAMP-dependent allosteric activation, agonism and antagonism, the comparative analysis of these molecular mechanisms in CBDs are required for the development of selective CBD effectors that may serve as drug leads for the treatment of cardiovascular, metabolic and neurological diseases.

1.2 Structural Biology of Human cAMP Receptors

In this section we will introduce the structural biology of the human cAMP receptors focusing primarily on the PKA and HCN systems, which were investigated extensively in this thesis. For further details on the structural biology of other human cAMP sensors, such as EPAC, we refer to prior published work (30–33). The structural organizations of PKA and HCN will be

introduced through a progressive 'zoom in' approach, starting from the general domain architecture and continuing with the details of the cAMP-binding domain (CBD) structures.

1.2.1 The PKA Domain Architecture

In the PKA holoenzyme, two catalytic (C) subunits are bound to a dimeric regulatory subunit (R2) (Figure 2). Upon binding to cAMP, each R-subunit undergoes a conformational change, releasing the C-subunit that becomes available to phosphorylate target proteins (34). There are a total of four isoforms of the R-subunit (RIα, RIβ, RIIα, and RIIβ) and three isoforms of the C-subunit (Cα, Cβ, Cγ) (35–37). Each of these isoforms varies slightly in sequence and exhibits a different tissue distribution, but they all share a similar domain organization. The R-subunit is composed of an N-terminal dimerization/docking (D/D) domain, followed by a linker that includes an auto-inhibitory segment, called Inhibitor Site (IS), and is C-terminally connected to two tandem CBDs (CBD-A and B) (Figure 2). While CBD-B regulates the access of cAMP to CBD-A, the linker and CBD-A mediate the key inhibitory interactions with C (38). With C binds, CBD-A adopts the 'H' conformation (38, 39), but switches to the 'B' state with cAMP binds (28). Further details of these structures will be discussed in Chapter 2.

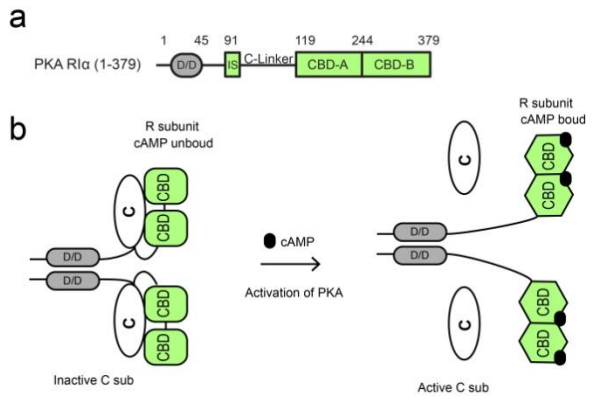

Figure 2: a) Domain organization of PKA R subunit b) Schematic model for the activation of PKA by cAMP. When cAMP binds the CBDs, structural and dynamic changes occur that lead to the C-subunit release from the R-subunit.

1.2.2 The HCN Domain Architecture

Four homologous HCN variants are known to date (HCN1-4) that share a similar multi-domain organization with an N-terminal trans-membrane region (TR) and a C-terminal intracellular region (IR) (40–43) (Figure 3a). The TR forms a tetrameric ion channel with each subunit in the tetramer composed of six helices (i.e. S1-6), two of which (S5 and S6) are at the core of the ion pore. The IR includes a linker that connects S6 to a C-terminal CBD (Figure 3b). In the absence of cAMP, the IR does not form tetramers and results in tonic inhibition of the HCN channel (7). Upon cAMP binding, the CBD undergoes conformational and/or dynamical changes that cause the linker to form a tetramer, which in turn releases channel inhibition and promotes pore opening (44). The CBD emerges, therefore, as the central controlling unit of HCN, as in the case of PKA. The CBDs of HCN and PKA share a conserved structural architecture.

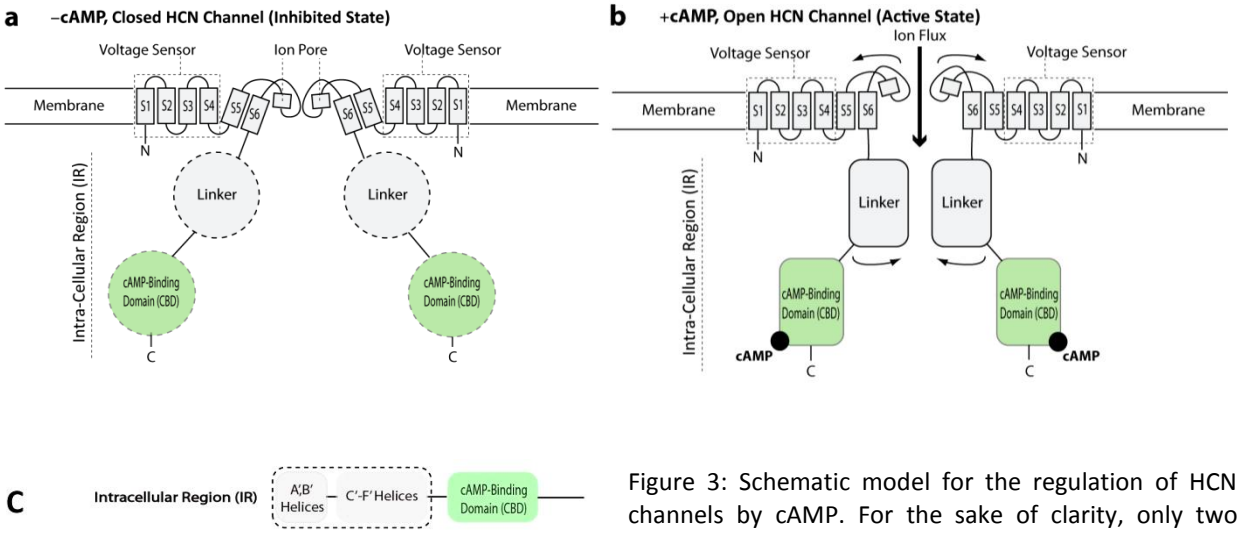

Figure 3: Schematic model for the regulation of HCN channels by cAMP. For the sake of clarity, only two subunits of the holo-tetramer are displayed. In the absence of cAMP, the intracellular region (IR) is not tetrameric and stabilizes the closed conformation of the HCN channel (a). When cAMP binds the CBD, structural and dynamical changes occur that lead to tetramerization of the linker and promote the open conformation of the HCN pore (b). (c) Domain organization of the HCN IR.

1.2.3 The CBD Structural Architecture

Human CBDs share a general secondary structure architecture (12, 41, 45) with a contiguous β-subdomain forming a well-defined eight-stranded β-barrel and a non-contiguous all α-helical subdomain (Figure 4). The β-subdomain comprises a relatively rigid β-core with two pivotal cAMP recognition elements: the PBC (phosphate-binding cassette) and the BBR (base-binding region). The PBC is located between β-strands 6 and 7 and contains a short α-helix (α5), which interacts with the phosphate moiety of the cAMP molecule. The BBR comprises the antiparallel strands β4-β5 and typically interacts with the adenine base of the cAMP molecule. The α-subdomain includes some of the most dynamic regions of the CBD. The helices at the N-terminus of the β-subdomain are referred to as the N-terminal helical bundle (NTHB spanning α1-α4) or the N3A motif (spanning α2-α4), whereas the helices C-terminal to the β-subdomain are referred to as the B-C helices (spanning α6-α7) or Lid, which provide an additional base-binding element, commonly known as the lid, and undergo distinct conformational changes upon cAMP binding.

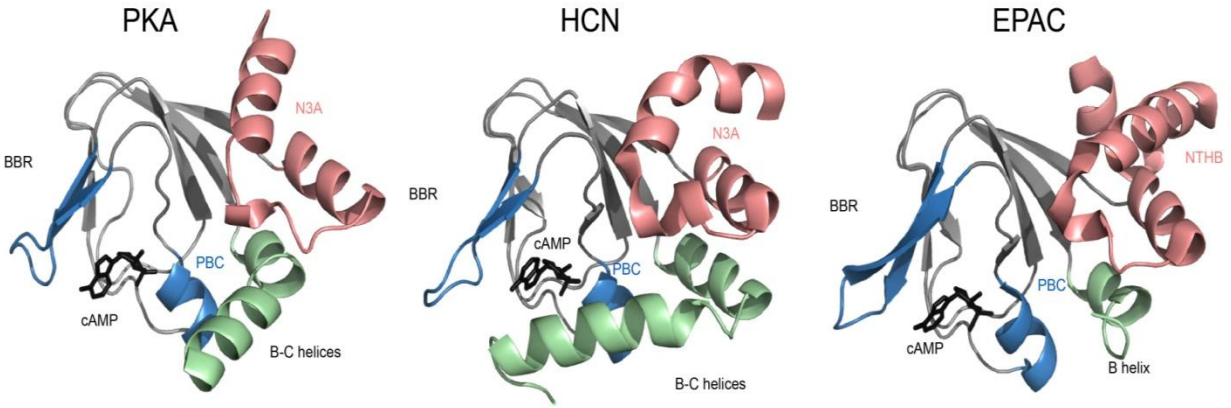

Figure 4: cAMP-Binding Domain (CBD) Structure of PKARIα-A (PDB 1RGS), HCN4 (PDB 3OTF) and EPAC2 (PDB 3CF6). cAMP is shown as black sticks. Four key regions are labelled as N3A or NTHB (red), BBR (blue), PBC (blue) and B-C helices (green).

1.2.4 PKA *versus* HCN Similarities and Differences

The cAMP-binding elements of PKA, EPAC and HCN are structurally homologous (41, 46, 47). These eukaryotic CBDs bind cAMP through three conserved key recognition elements (48), i.e. the PBC, the BBR and the lid and they all share a similar secondary and tertiary structure (Figure 4). Despite these structural similarities among CBDs, several marked functional differences have been reported:

a) The regulatory subunit of PKA binds cAMP with association constants that are approximately three orders of magnitude higher than those measured for EPAC and HCN (48).

b) HCN responds differently from PKA to the Rp-cAMPS analog, which is referred to here as Rp. Rp is an agonist for HCN, while it is an antagonist for both EPAC and PKA. This observation suggests that the pathways suppressed by Rp are obligatory for the propagation of the cAMP signal in EPAC and PKA, but are dispensable in HCN (49, 50).

c) Molecular Dynamics (MD) simulations in HCN indicate that cAMP causes long-range perturbations resulting in an overall quenching of dynamics for the N-terminal helices (51, 52). This is in contrast to the EPAC CBD, for which the dynamics of the N-terminal helical bundle is enhanced when cAMP binds (53, 54).

These multiple independent lines of evidence suggest that the cAMP-dependent allosteric mechanisms of PKA, EPAC and HCN CBDs are significantly different from each other. These differences are not easily accounted for by the available structures of cAMP complexes. Here, we hypothesize that the functional differences observed among eukaryotic CBDs reflect

differences in their dynamic profiles. Some of the most dynamic sites in both PKA and HCN are the linkers, which will be the focus of the next section.

1.3 Functional Linkers

Linkers are defined as polypeptide segments connecting fully folded protein domains. Unlike the adjacent domains, linkers are often flexible and only partially structured. Despite the dynamic nature of linkers, recent studies have shown that domain linkers can play essential functional roles (55–57). For example, in the Src kinase family, the repression of the kinase activity by the regulatory domain is eliminated upon a mutation in the linker region of the regulatory subunit. This observation proves that the linker plays a crucial role in the coupling of the regulatory SH2 and SH3 domains to the catalytic domain (58). Another example is provided by the deletion of four amino acids from the linker connecting two sub-domains of phosphorylated smooth-muscle myosin, which leads to the termination of its actin translocating activity (59). This example suggests that not only the composition of the linker is critical for its function, but also the length is important. In general, altering the length of linkers, which are connecting the domains, has been shown to affect protein stability, folding rates and domain–domain orientation. Overall, linkers of structured proteins have been hypothesized to play a pivotal role in tuning physiological function(60).

1.3.1 Linkers in PKA

The regulatory subunit of PKA RIα contains three linker regions: 1) The N-linker (45-90) between the dimerization/docking domain and the inhibitory site; 2) The C-Linker (91-118) includes the inhibitory site and connects it to CBD-A; 3) The B-C hinge helices connecting CBD-A to CBD-B (226-251). The N-linker plays an important role in defining the quaternary structure of the R:C holoenzyme and is ordered differently in the RIα-, RIβ- and RIIβ-subunits following their binding to the C-subunit (35). The isoform-specific positioning of the N-linker contributes in unique ways to the organization of each tetrameric holoenzyme. The C-linker preceding CBD-A includes the key kinase inhibitory element. Under resting conditions, the C linker docks into the active site of the catalytic subunit (C), is well-structured and clearly resolved in the crystal structure of the R:C complex (38). However, upon cAMP binding, the kinase is released and the C-linker becomes more solvent-exposed and partially flexible. Hence, in the R:cAMP$_2$ complex, only partial electron density is observed for the linker and several linker residues that are resolved are also affected by crystal packing (28, 61). As to the third type of linker in PKA RIα, its inter-CBD location implies that its structure and dynamic profile are to a large extent dictated by the interactions mediated by the CBDs. In the C-subunit bound conformation (38), the two CBDs are well separated and the RIα subunit adopts an extended dumbbell shape ("open inter-CBD topology") (Figure 5). Due to extension of the inter-CBD linker, the center of mass of CBD-B moves over 60 Å away from the position it occupies in the cAMP-bound structure (Figure 5). In the latter, the two CBDs are in contact and adopt a "closed inter-CBD topology", leading to a kinked C hinge helix in the linker.

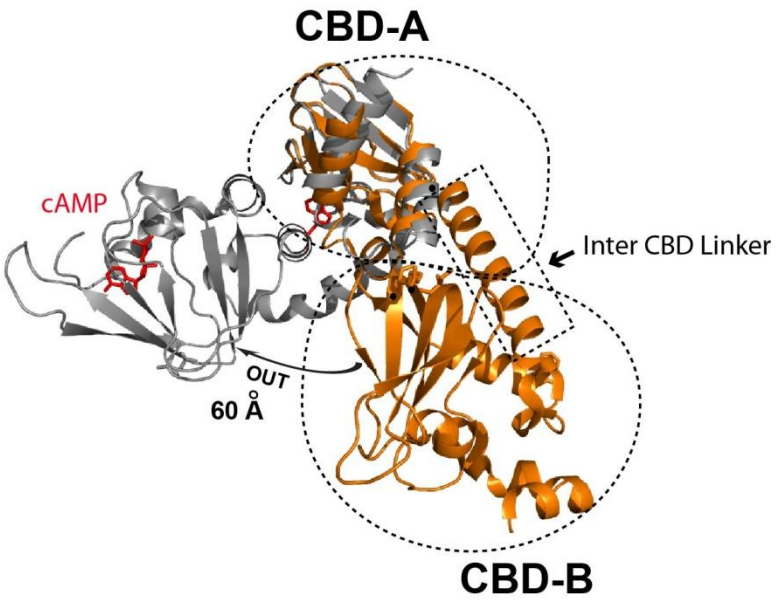

Figure 5: cAMP bound (gray) and C subunit bound structure (orange) of PKA RIα subunit, PDB codes 1RGS and 2QCS, respectively.

1.3.2 Linkers in HCN

HCN contains two flexible linker regions: 1) The so-called "C-linker" comprising the six N-terminal helices (i.e. A'-F') between S6 and the CBD; 2) An unstructured segment following the CBD (41, 42). The C-linker region is the primary site of tetramerization within the intracellular region (IR) of HCN. The C-linker region is also involved in the coupling of ligand binding to the opening of the pore (Figure 3). The flexible region following the CBD is less conserved among the HCN isoforms and mediates critical protein-protein interactions. For example, the tetratricopeptide repeat containing the Rab8b interacting protein (TRP1P8b) binds this region tightly and is considered to be involved in the endocytosis of HCN channels (62). In addition, the p38Map kinase is known to phosphorylate a Tyr residue in this region, leading to the modulation of the HCN voltage dependence in the hippocampus (63). Hence, both linkers adjacent to the HCN CBD play pivotal functions.

Given the critical functional role of linkers in HCN and PKA, one of the primary goals of this thesis is to understand how the cAMP signal allosterically propagates from the structured CBD to the partially unstructured adjacent linkers. Considering the dynamic nature of linkers, the elucidation of the cAMP-dependent allosteric networks that extend beyond the CBD to the linkers cannot rely only on classical methods of structure determination, which are typically utilized for globular protein with well-defined conformations. The investigation of the structural dynamics of linkers requires a more comprehensive and multifaceted experimental design, as discussed more extensively in the following section.

1.4 General Experimental Design to Investigate the Structure and Dynamics of Linkers

1.4.1 Sample Preparation

1.4.1.1 Selection of Construct Boundaries

Successful protein NMR experiments rely on well-designed protein constructs containing the functional region(s) of interest (64). In addition, depending on the purpose of the experiments to be performed, a variety of protein constructs may be necessary. For example, the shortest PKA construct examined so far consists of residues 119-244 of the CBD-A domain in the PKA RIα regulatory subunit, *i.e.* PKA RIα (119-244) (30, 65–67). This constructs exhibits nM binding affinity for cAMP, and has been identified as a minimal binding unit for cAMP. PKA RIα (119-244) has proven useful for studying conformational changes and dynamics upon binding with cAMP and different analogs (30, 65–67). However, it lacks the catalytic subunit binding region (inhibitory region) and adjacent linker region, and therefore lacks key

allosteric features present in the PKA regulatory subunit. To address this issue, a construct containing the inhibitory and linker regions was designed, *i.e.* PKA RIα (91-244), which is the minimal RIα construct that can bind to both the catalytic subunit and cAMP with affinities comparable to full length RIα. As such, it is an excellent model for the biological interactions involving PKA. However, the PKA RIα (91-244) construct undergoes self-association at high concentrations. Therefore, a somewhat shorter PKA RIα (96-244) construct was used to obtain high concentration protein samples for use in low-sensitivity NMR experiments such as triple resonance NMR experiments.

Although the PKA RIα (96-244) construct is not capable of binding the catalytic-subunit, its HSQC spectrum is similar to that of PKA RIα (91-244). Furthermore, to study inter-CBD interactions, a longer construct, PKA RIα (119-379), was used (68), which contains both the CBD-A and CBD-B domains of PKA RIα. Indeed, PKA RIα (119-379) has proven to be an excellent construct for understanding CBD domain cross-talk, and also for studying the role of the CBD-A lid, which is located in the N-terminal segment of the CBD-B domain. Once a set of constructs are designed to address the functional question of interest, the next step is the optimization of their preparation.

1.4.1.2 Optimization of Protein Yields

High protein yields are of course desirable as this allows one to obtain multiple NMR samples from a single purified batch of protein repetitive protein preparations, and permitting execution of multiple NMR analyses on protein samples with consistent solution conditions. In

this respect, it is necessary that the low protein yields encountered with some CBDs be improved by optimizing the protein expression conditions through multiple approaches, which include:

(a) Codon-optimization of the protein-encoding DNA sequence;

(b) Incorporation of a cleavable solubility tag in the encoded protein construct;

(c) Employing various *E. coli* strains for expression.

The PKA RIα (91-244) construct initially resulted in a low protein yield (0.5 mg per liter M9 medium), but by using a new DNA clone whose sequence was codon-optimized through proprietary algorithms that replace rare codons and optimize GC content to stabilize the mRNA, the protein yield was increased 20-fold compared to the initial protein preparation. Furthermore, to enhance protein solubility during expression, the PKA constructs were expressed with an N-terminal small ubiquitin-related modifier (SUMO) tag. Additional means of optimizing the protein expression conditions include adjustments of:

(I) The cell culture density;

(II) The concentration of inducing reagent added to induce protein expression,

(III) Incubation temperature and time for which protein expression is allowed to proceed after induction.

However, even after expression yields are optimized, another challenge that often remains is the preparation of apo proteins, i.e. unbound from metabolites that are endogenous to *E. coli*, such as cAMP.

1.4.1.3 cAMP Removal and R:C Complex Preparation

The cAMP-free (apo) form of CBDs is a key component of the comparative NMR analyses aimed at understanding the molecular basis of cAMP-dependent binding and allostery. The apo CBD often closely represents the auto-inhibited state of the CBD and it provides a reference spectrum to evaluate the perturbations caused by cAMP. However, the preparation of apo CBDs poses experimental challenges when the Kd is < μM, because cAMP is endogenous to *E. coli.* and CBDs that are over-expressed in *E. coli* can easily bind with cAMP. This is a potential complication, since the residual cAMP-bound CBD will shift the apo/bound state equilibrium enough to alter the NMR spectral analysis results. It is therefore critical to establish, before further NMR analyses, whether cAMP-bound CBD is present in the samples purified from *E. coli.* One simple but effective means of detecting the presence of residual cAMP-bound CBD is by acquiring {^{1}H,^{15}N}-HSQC spectra. For example, in the case of HCN, where the cAMP binding affinity is in the μM range (44, 69), the equilibrium between apo and cAMP-bound states exhibits a mixture of fast-exchange and slow-exchange dynamics, depending on the residues and the magnitude of the respective cAMP-dependent chemical shift change. In this case, we can use the slow-exchanging residues to detect the presence of residual cAMP-bound CBD in the apo sample by checking for the presence of a second set of {^{1}H,^{15}N}-HSQC cross peaks that would be generated for these residues by the residual cAMP-bound CBD. For the PKA R-subunit, however, the CBD constructs examined by NMR typically exhibit high binding affinities for cAMP (Kd << μM) (30), and as a result, the purified PKA construct is always a mixture of cAMP-bound and apo states even after extensive dialysis or size exclusion purification. Therefore, to remove residual cAMP from the PKA R-subunit, the PKA RIα

constructs are first unfolded using 8 M urea and the residual cAMP is removed via size exclusion column (SEC) or PD10 desalting column. The unfolded PKA is then refolded by extensive dialysis, and any aggregated protein is eliminated by further SEC purification. To confirm that the refolded PKA is indeed in its apo state, {^{1}H,^{15}N}-HSQC analysis is then performed to check the slow-exchanging residues for the absence of {^{1}H,^{15}N}-HSQC cross peaks arising from the cAMP-bound state. Alternatively, residual cAMP-bound CBD can be detected using 260/280 nm absorbance ratio measurements. Once CBD constructs in their apo form are prepared, the comparative analysis designed to investigate cAMP-allostery is implemented through a combination of bioassays, unfolding and NMR studies.

1.4.2 Bioassay

Although low MW protein segments result in increased NMR sensitivity and resolution relative to higher MW constructs, and hence have the potential to provide access to a wealth of dynamical and structural information on CBDs, it is critical to validate the functional relevance of NMR results through bioassays. In order to verify whether a model based on truncated NMR constructs still applies to the respective full-length protein, a useful approach relies on mutations that are analyzed both at the level of truncated constructs by NMR and at the level of longer constructs and/or larger complexes by bioassays. In addition, if the effect of a mutation on a function is not obvious based on examination of available structures, but it is clearly explained by NMR, this exercise reveals the unique added value provided by dynamic NMR investigations relative to traditional purely structural studies. Hence, it is critical to

complement biophysical (e.g. NMR, unfolding, etc.) with biochemical (e.g. enzymatic assays) approaches.

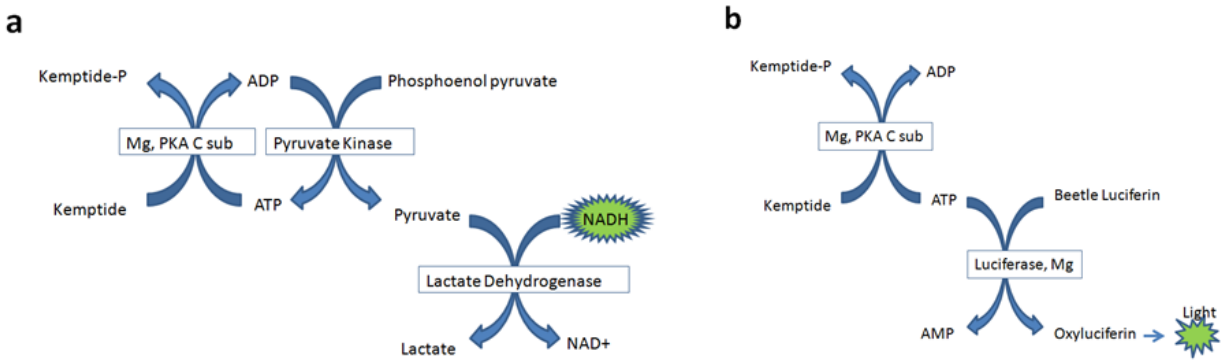

Figure 6: PKA enzymatic assay, a) Cook assay: the increase of ADP in the kinase reaction solution is detected by the absorbance decrease at 340nm due to NADH loss. Mg represents magnesium and PKA C sub represents catalytic subunit of PKA. b) The luciferase reaction: the reaction between Beetle luciferin and ATP is catalyzed by luciferase resulting in oxyluciferin, which allows the quantification of the amount of residual ATP in the reaction mixture.

(70), which detects the amount of Mg-ADP generated through phosphorylation by coupling it to the pyruvate kinase and lactic dehydrogenase reactions (Figure 6). Alternatively, kinase activity can be measured through ATP detecting assays (71), which quantify the amount of ATP remaining in the solution following a kinase reaction using Luciferin. In the case of HCN, the voltage and cyclic nucleotide dependence of ion channel opening is typically gauged through electrophysiology, such as a patch clamp experiments (41), which can control active or inactive state of channel by voltage and intra electrode content, is commonly used to confirm the voltage dependent potassium channel activity.

1.4.3 Equilibrium Unfolding Studies

Unfolding studies at equilibrium are a robust tool to map the free energy landscape that defines allosteric systems. Two approaches to measure unfolding free energies are hydrogen-exchange, which relies on thermal fluctuations to induce transient local or global unfolding (30, 72), and chemical unfolding, which relies on a denaturant such as urea to induce unfolding that is monitored by available spectroscopic probes, for example by intrinsic fluorescence (72–74). Both methods have been applied to CBDs. For instance, hydrogen-deuterium exchange rates measured for residues in the inner β strands of PKA CBD-A report on transient global unfolding events (72). This result was established by comparing the ΔG of unfolding estimated from the protection factors with the ΔG of unfolding measured through urea unfolding monitored by intrinsic fluorescence. The ability to measure free energies of global unfolding ($\Delta G_{unfolding}$) by hydrogen-exchange is useful in several applications involving ligand binding, allostery and inter-domain communication. Ligand-dependent changes in $\Delta G_{unfolding}$ provide an assessment of both absolute and relative ligand affinities (i.e. Kd values), including low Kd values in the nM range that are more challenging to measure through other methods. Variations of $\Delta G_{unfolding}$ upon domain or linker deletion are useful to gauge the free energy of inter-domain or linker-domain interactions.

1.4.4 NMR Spectroscopy as a Tool to Investigate Structure and Dynamics

While low resolution biophysical studies such as equilibrium unfolding are excellent tools to start mapping the free energy landscape of allosteric transitions, they do not provide

an atomic resolution picture of allostery, nor do they sense the dynamics underlying allosteric control. For mapping dynamics at atomic resolution, we complemented bioassays and unfolding investigations with NMR spectroscopy.

NMR is uniquely suited for the characterisation of biomolecular dynamics at an atomic or the residue resolution. In addition, NMR provides a single tool to comprehensively probe internal motions and conformational fluctuations over a wide range of time scales, ranging from ps to min (75, 76). Furthermore, NMR is also useful when proteins resist attempts at crystallization. Because NMR studies are performed in solution, this method offers a convenient means of monitoring changes in protein structure under near physiological conditions.

NMR is an ideal technique to investigate cAMP-dependent allostery as it is exquisitely sensitive to the dynamical and structural variations underlying allosteric processes. These include dynamic changes together with subtle, but functionally critical, rearrangements of charge distributions and/or hydrophobic core packing. Furthermore, it is now clear that the functions of CBDs are more adequately rationalized by an ensemble of multiple conformations in equilibrium with each other rather than by a single structure. Such intrinsic conformational heterogeneity typical of CBDs limits the resolution of their crystal structures and leads to high B-factors. As a result, it is often not possible to identify by X-ray crystallography meaningful differences between different functional states of CBDs. For instance, no significant differences were detected by X-ray between the crystal structures of the HCN CBD in the apo form and bound to cAMP (77), despite the clearly different ion channel activities. However, marked apo *versus* holo differences are clearly observed for the HCN CBD by NMR, which lead to a mechanism of HCN inhibition. It appears therefore that, while CBD crystal structures provide an

invaluable initial framework for further biophysical investigations aimed at characterizing the nature of the cAMP dependent allostery, NMR is essential to investigating the highly dynamic systems regulated by cAMP.

1.4.5 NMR Spectroscopy as a Tool to Investigate Non-Covalent Interactions

NMR is an excellent tool not only to map dynamics at atomic resolution and over multiple time scales, but also for mapping weak but functionally relevant interactions. Two robust NMR measurements that are widely used in this respect are chemical shift changes and paramagnetic relaxation enhancement (PRE) experiments (78). Chemical shifts are highly informative but they include contributions from both direct non-covalent interactions and indirect allosteric effects. One approach to separate these two contributions is the Chemical shift covariance analysis (CHESCA) (32). CHESCA is an effective method for mapping functionally relevant allosteric networks, including those in dynamic and partially unstructured regions. CHESCA relies on the covariance analysis of NMR chemical shifts to identify and functionally categorize allosteric networks of residues eliciting concerted responses to a series of analogs of the allosteric effector ligand. The CHESCA approach is useful to understand how the allosteric signals propagate to flexible linker regions. However, it is advisable to confirm the CHESCA results with independent measurements, such as paramagnetic relaxation enhancement (PRE) experiments. PRE is a valuable method to probe long-range transient interactions between a spin label and the rest of the protein. The location of the spin-label can be guided by the CHESCA results, which identify sites that are not part of the CHESCA allosteric network, but at

the same time are in the vicinity of the linker residues involved in interactions with CBDs. Hence, CHESCA and PREs are two methods that are highly synergistic.

1.5 Goal of the Thesis and Main Results

The biophysical and biochemical approaches outlined above were utilized in this thesis to understand how cAMP binding to a folded CBD results in the allosteric control of an adjacent N-terminal linker, which spans critical functional sites but is only partially structured and dynamic. This central question was addressed here for three different eukaryotic CBDs: the PKA RIα CBD-A and B as well as the HCN4 CBD. Detailed reports of the results obtained for these three systems are available in Chapters 2, 4 and 3, respectively. However, we include below brief summaries for each chapter.

1.5.1 C-Linker Control by the PKA RIα CBD-A

Protein kinase A (PKA) is a prototype of multi-domain signaling proteins functioning as allosteric conformational switches (37). Allosteric transitions have been the subject of extensive structural and dynamic investigations focusing mainly on folded domains. However, the current understanding of the allosteric role of partially unstructured linkers flanking globular domains is limited. Here, we show that a dynamic linker in the regulatory subunit (R) of PKA serves not only as a passive covalent thread, but also as an active allosteric element that controls activation of the kinase subunit (C) by tuning the inhibitory pre-equilibrium of a minimally populated intermediate (apo R). Apo R samples both C-binding competent (inactive) and

incompetent (active) conformations within a nearly degenerate free energy landscape and such degeneracy maximally amplifies the response to weak (~2RT), but conformation selective interactions elicited by the linker. Specifically, the R linker that in the R:C complex docks in the active site of C, in apo R preferentially interacts with the C-binding incompetent state of the adjacent cAMP-binding domain (CBD). These unanticipated findings imply that the formation of the inter-molecular R:C inhibitory interface occurs at the expense of destabilizing the intra-molecular linker/CBD interactions in R. A direct implication of this model, which was not predictable solely based on protein structure, is that the disruption of a linker/CBD salt bridge in the R:C complex unexpectedly leads to increased affinity of R for C. The linker includes therefore sites of R:C complex frustration and frustration-relieving mutations enhance the kinase inhibitory potency of R without compromising its specificity.

1.5.2 Inter-CBD Linker Control by the PKA RIα CBD-B

Protein Kinase A (PKA) is the major receptor for the cAMP second messenger in eukaryotes (37). cAMP binds to two tandem cAMP-binding domains (CBD-A and B) within the regulatory subunit of PKA (R) leading to the release of the active catalytic subunit (C). While CBD-A is required for PKA inhibition and activation, CBD-B functions as a "gatekeeper" domain that modulates the control exerted by CBD-A (38). Preliminary evidence suggests that CBD-B dynamics is critical for its gatekeeper function (36). In order to test this hypothesis, here we investigate by NMR the two-domain construct RIα (91-379) in its apo, $cAMP_2$ and C-bound forms. Our comparative NMR analysis led us to a double conformational selection model in which each apo CBD dynamically samples both active and inactive states independently of the

adjacent CBD within a nearly degenerate free energy landscape. Such degeneracy is critical to explain the sensitivity of CBD-B to weak interactions with C and its high affinity for cAMP. Binding of cAMP eliminates this degeneracy, as it selectively stabilizes the active conformation within each CBD and inter-CBD contacts, which require both cAMP and W260 contributed by CBD-B to cap cAMP bound to CBD-A. The inter-CBD interface is dispensable for intra-CBD conformational selection, but is indispensable for full activation of PKA as it occludes C-subunit recognition sites within CBD-A. In addition, the two structurally homologous cAMP-bound CBDs exhibit marked differences in their residual dynamics profiles, supporting the notion that conservation of structure does not necessarily imply conservation of dynamics.

1.5.3 Intracellular Linker Control by the HCN4 CBD

Hyperpolarization-activated cyclic nucleotide-gated (HCN) ion channels control neuronal and cardiac electrical rhythmicity (10). There are four homologous isoforms (HCN1-4) sharing a common multi-domain architecture that includes an N-terminal transmembrane tetrameric ion channel followed by a cytoplasmic "C-linker," which connects a more distal cAMP-binding domain (CBD) to the inner pore (42). Channel opening is primarily stimulated by transmembrane elements that sense membrane hyperpolarization, while cAMP reduces the voltage required for HCN activation by promoting tetramerization of the intracellular C-linker, which in turn relieves auto-inhibition of the inner pore gate. Although binding of cAMP has been proposed to relieve auto-inhibition by affecting the structure of the C-linker and CBD, the nature and extent of these cAMP-dependent changes remain limitedly explored (40, 42). Here, we used NMR to probe the changes caused by the binding of cAMP and of cCMP, a partial

agonist, to the apo-CBD of HCN4 (79). Our data indicate that the CBD exists in a dynamic two-state equilibrium, whose position as gauged by NMR chemical shifts correlates with the V½ voltage measured through electrophysiology. In the absence of cAMP, the most populated CBD state leads to steric clashes with the activated or "tetrameric" C-linker, which becomes energetically unfavoured. The steric clashes of the apo tetramer are eliminated either by cAMP binding, which selects for a CBD state devoid of steric clashes with the tetrameric C-linker and facilitates channel opening, or by a transition of apo-HCN to monomers or dimer of dimers, in which the C-linker becomes less structured, and channel opening is not facilitated.

1.6 References:

1. Levick, J.R. 2013. An Introduction to Cardiovascular Physiology. Elsevier Science.

2. Bos, J.L. 2006. Epac proteins: multi-purpose cAMP targets. Trends Biochem. Sci. 31: 680–686.

3. Serezani, C.H., M.N. Ballinger, D.M. Aronoff, and M. Peters-Golden. 2008. Cyclic AMP: master regulator of innate immune cell function. Am. J. Respir. Cell Mol. Biol. 39: 127–132.

4. Stork, P.J., and J.M. Schmitt. 2002. Crosstalk between cAMP and MAP kinase signaling in the regulation of cell proliferation. Trends Cell Biol. 12: 258–266.

5. Shabb, J.B. 2001. Physiological substrates of cAMP-dependent protein kinase. Chem. Rev. 101: 2381–2411.

6. Krebs, E.G. 1993. Nobel Lecture. Protein phosphorylation and cellular regulation I. Biosci. Rep. 13: 127–42.

7. Wainger, B.J., M. DeGennaro, B. Santoro, S.A. Siegelbaum, and G.R. Tibbs. 2001. Molecular mechanism of cAMP modulation of HCN pacemaker channels. Nature. 411: 805–810.

8. De Rooij, J., F.J. Zwartkruis, M.H. Verheijen, R.H. Cool, S.M. Nijman, A. Wittinghofer, and J.L. Bos. 1998. Epac is a Rap1 guanine-nucleotide-exchange factor directly activated by cyclic AMP. Nature. 396: 474–477.

9. Kawasaki, H., G.M. Springett, N. Mochizuki, S. Toki, M. Nakaya, M. Matsuda, D.E. Housman, and A.M. Graybiel. 1998. A family of cAMP-binding proteins that directly activate Rap1. Science. 282: 2275–2279.

10. Postea, O., and M. Biel. 2011. Exploring HCN channels as novel drug targets. Nat. Rev. Drug Discov. 10: 903–14.

11. McPhee, I., L.C.D. Gibson, J. Kewney, C. Darroch, P.A. Stevens, D. Spinks, A. Cooreman, and S.J. MacKenzie. 2005. Cyclic nucleotide signalling: a molecular approach to drug discovery for Alzheimer's disease. .

12. Bos, J.L. 2003. Epac: a new cAMP target and new avenues in cAMP research. Nat. Rev. cell Biol. 4: 733–738.

13. Kuschel, M., Y.Y. Zhou, H. Cheng, S.J. Zhang, Y. Chen, E.G. Lakatta, and R.P. Xiao. 1999. G(i) protein-mediated functional compartmentalization of cardiac beta(2)-adrenergic signaling. J. Biol. Chem. 274: 22048–22052.

14. Lochner, A., S. Genade, E. Tromp, T. Podzuweit, and J.A. Moolman. 1999. Ischemic preconditioning and the beta-adrenergic signal transduction pathway. Circulation. 100: 958–966.

15. Lakatta, E.G., V.A. Maltsev, and T.M. Vinogradova. 2010. A coupled SYSTEM of intracellular Ca2+ clocks and surface membrane voltage clocks controls the timekeeping mechanism of the heart's pacemaker. Circ. Res. 106: 659–673.

16. Tanaka, K. 2001. Alteration of second messengers during acute cerebral ischemia - adenylate cyclase, cyclic AMP-dependent protein kinase, and cyclic AMP response element binding protein. Prog. Neurobiol. 65: 173–207.

17. Kirschner, L.S., J.A. Carney, S.D. Pack, S.E. Taymans, C. Giatzakis, Y.S. Cho, Y.S. Cho-Chung, and C.A. Stratakis. 2000. Mutations of the gene encoding the protein kinase A type I-alpha regulatory subunit in patients with the Carney complex. Nat. Genet. 26: 89–92.

18. Casey, M., C.J. Vaughan, J. He, C.J. Hatcher, J.M. Winter, S. Weremowicz, K. Montgomery, R. Kucherlapati, C.C. Morton, and C.T. Basson. 2000. Mutations in the protein kinase A R1alpha regulatory subunit cause familial cardiac myxomas and Carney complex. J. Clin. Invest. 106: R31–8.

19. Milanesi, R., M. Baruscotti, T. Gnecchi-Ruscone, and D. DiFrancesco. 2006. Familial sinus bradycardia associated with a mutation in the cardiac pacemaker channel. N. Engl. J. Med. 354: 151–157.

20. Katz, A.M., and B.H. Lorell. 2000. Regulation of cardiac contraction and relaxation. Circulation. 102: IV69–74.

21. Métrich, M., A. Lucas, M. Gastineau, J.L. Samuel, C. Heymes, E. Morel, and F. Lezoualc'h. 2008. Epac mediates β-adrenergic receptor-induced cardiomyocyte hypertrophy. Circ. Res. 102: 959–965.

22. Keov, P., P.M. Sexton, and A. Christopoulos. 2011. Allosteric modulation of G protein-coupled receptors: a pharmacological perspective. Neuropharmacology. 60: 24–35.

23. Conn, P.J., A. Christopoulos, and C.W. Lindsley. 2009. Allosteric modulators of GPCRs: a novel approach for the treatment of CNS disorders. Nat. Rev. Discov. 8: 41–54.

24. Hardy, J. a., and J. a. Wells. 2004. Searching for new allosteric sites in enzymes. Curr. Opin. Struct. Biol. 14: 706–715.

25. Wenthur, C.J., P.R. Gentry, T.P. Mathews, and C.W. Lindsley. 2014. Drugs for allosteric sites on receptors. Annu. Rev. Pharmacol. Toxicol. 54: 165–84.

26. Fang, Z., C. Grütter, and D. Rauh. 2013. Strategies for the selective regulation of kinases with allosteric modulators: exploiting exclusive structural features. ACS Chem. Biol. 8: 58–70.

27. Davies, S.P., H. Reddy, M. Caivano, and P. Cohen. 2000. Specificity and mechanism of action of some commonly used protein kinase inhibitors. Biochem. J. 351: 95–105.

28. Su, Y., W.R. Dostmann, F.W. Herberg, K. Durick, N.H. Xuong, L. Ten Eyck, S.S. Taylor, and K.I. Varughese. 1995. Regulatory subunit of protein kinase A: structure of deletion mutant with cAMP binding domains. Science. 269: 807–813.

29. DiFrancesco, D. 2010. The role of the funny current in pacemaker activity. Circ. Res. 106: 434–446.

30. Das, R., V. Esposito, M. Abu-Abed, G.S. Anand, S.S. Taylor, and G. Melacini. 2007. cAMP activation of PKA defines an ancient signaling mechanism. Proc. Natl. Acad. Sci. U. S. A. 104: 93–98.

31. Das, R., M.T. Mazhab-Jafari, S. Chowdhury, S. SilDas, R. Selvaratnam, and G. Melacini. 2008. Entropy-driven cAMP-dependent allosteric control of inhibitory interactions in exchange proteins directly activated by cAMP. J. Biol. Chem. 283: 19691–703.

32. Selvaratnam, R., S. Chowdhury, B. VanSchouwen, and G. Melacini. 2011. Mapping allostery through the covariance analysis of NMR chemical shifts. Proc. Natl. Acad. Sci. U. S. A. 108: 6133–6138.

33. Mazhab-Jafari, M.T., R. Das, S. a. Fotheringham, S. SilDas, S. Chowdhury, and G. Melacini. 2007. Understanding cAMP-dependent allostery by NMR spectroscopy: Comparative analysis of the EPAC1 cAMP-binding domain in its apo and cAMP-bound states. J. Am. Chem. Soc. 129: 14482–14492.

34. Berman, H.M., L.F. Ten Eyck, D.S. Goodsell, N.M. Haste, A. Kornev, and S.S. Taylor. 2005. The cAMP binding domain: an ancient signaling module. Proc. Natl. Acad. Sci. U. S. A. 102: 45–50.

35. Zhang, P., A.P. Kornev, J. Wu, and S.S. Taylor. 2015. Discovery of allostery in PKA signaling. Biophys. Rev. 7: 227–238.

36. Vigil, D., D.K. Blumenthal, W.T. Heller, S. Brown, J.M. Canaves, S.S. Taylor, and J. Trewhella. 2004. Conformational differences among solution structures of the type I??, II?? and II?? protein kinase A regulatory subunit homodimers: Role of the linker regions. J. Mol. Biol. 337: 1183–1194.

37. Taylor, S.S., C. Kim, D. Vigil, N.M. Haste, J. Yang, J. Wu, and G.S. Anand. 2005. Dynamics of signaling by PKA. Biochim. Biophys. Acta. 1754: 25–37.

38. Kim, C., C.Y. Cheng, S.A. Saldanha, and S.S. Taylor. 2007. PKA-I holoenzyme structure reveals a mechanism for cAMP-dependent activation. Cell. 130: 1032–1043.

39. Kim, C., N.H. Xuong, and S.S. Taylor. 2005. Crystal structure of a complex between the catalytic and regulatory (RIalpha) subunits of PKA. Science. 307: 690–696.

40. Robinson, R.B., and S.A. Siegelbaum. 2003. Hyperpolarization-activated cation currents: from molecules to physiological function. Annu. Rev. Physiol. 65: 453–480.

41. Biel, M., A. Schneider, and C. Wahl. 2002. Cardiac HCN channels: structure, function, and modulation. Trends Cardiovasc. Med. 12: 206–212.

42. Zagotta, W.N., N.B. Olivier, K.D. Black, E.C. Young, R. Olson, and E. Gouaux. 2003. Structural basis for modulation and agonist specificity of HCN pacemaker channels. Nature. 425: 200–205.

43. Rehmann, H., A. Wittinghofer, and J.L. Bos. 2007. Capturing cyclic nucleotides in action: snapshots from crystallographic studies. Nat. Rev. cell Biol. 8: 63–73.

44. Lolicato, M., M. Nardini, S. Gazzarrini, S. Moller, D. Bertinetti, F.W. Herberg, M. Bolognesi, H. Martin, M. Fasolini, J.A. Bertrand, C. Arrigoni, G. Thiel, and A. Moroni. 2011. Tetramerization dynamics of C-terminal domain underlies isoform-specific cAMP gating in hyperpolarization-activated cyclic nucleotide-gated channels. J. Biol. Chem. 286: 44811–44820.

45. Kannan, N., J. Wu, G.S. Anand, S. Yooseph, A.F. Neuwald, J.C. Venter, and S.S. Taylor. 2007. Evolution of allostery in the cyclic nucleotide binding module. Genome Biol. 8: R264.

46. Borland, G., B.O. Smith, and S.J. Yarwood. 2009. EPAC proteins transduce diverse cellular actions of cAMP. Br. J. Pharmacol. 158: 70–86.

47. Kannan, N., J. Wu, G.S. Anand, S. Yooseph, A.F. Neuwald, J.C. Venter, and S.S. Taylor. 2007. Evolution of allostery in the cyclic nucleotide binding module. Genome Biol. 8: R264.

48. Boulton, S., M. Akimoto, B. Vanschouwen, K. Moleschi, R. Selvaratnam, R. Giri, and G. Melacini. 2014. Tapping the translation potential of cAMP signalling: molecular basis for selectivity in cAMP agonism and antagonism as revealed by NMR. Biochem. Soc. Trans. 42: 302–307.

49. Rehmann, H., F. Schwede, S.O. Doskeland, A. Wittinghofer, and J.L. Bos. 2003. Ligand-mediated activation of the cAMP-responsive guanine nucleotide exchange factor Epac. J. Biol. Chem. 278: 38548–38556.

50. Rehmann, H., B. Prakash, E. Wolf, A. Rueppel, J. de Rooij, J.L. Bos, and A. Wittinghofer. 2003. Structure and regulation of the cAMP-binding domains of Epac2. Nat. Struct. Biol. 10: 26–32.

51. Zhou, L., and S.A. Siegelbaum. 2007. Gating of HCN channels by cyclic nucleotides: residue contacts that underlie ligand binding, selectivity, and efficacy. Structure. 15: 655–670.

52. Berrera, M., S. Pantano, and P. Carloni. 2006. cAMP Modulation of the cytoplasmic domain in the HCN2 channel investigated by molecular simulations. Biophys. J. 90: 3428–3433.

53. Das, R., M. Abu-Abed, and G. Melacini. 2006. Mapping allostery through equilibrium perturbation NMR spectroscopy. J. Am. Chem. Soc. 128: 8406–8407.

54. VanSchouwen, B., R. Selvaratnam, F. Fogolari, and G. Melacini. 2011. Role of dynamics in the autoinhibition and activation of the exchange protein directly activated by cyclic AMP (EPAC). J. Biol. Chem. 286: 42655–42669.

55. Ma, B., C.J. Tsai, T. Haliloglu, and R. Nussinov. 2011. Dynamic allostery: linkers are not merely flexible. Structure. 19: 907–917.

56. Gokhale, R.S., and C. Khosla. 2000. Role of linkers in communication between protein modules. Curr. Opin. Chem. Biol. 4: 22–7.

57. Blumenschein, T.M. a, D.B. Stone, R.J. Fletterick, R. a. Mendelson, and B.D. Sykes. 2005. Calcium-dependent changes in the flexibility of the regulatory domain of troponin C in the troponin complex. J. Biol. Chem. 280: 21924–21932.

58. Briggs, S.D., and T.E. Smithgall. 1999. SH2-kinase linker mutations release Hck tyrosine kinase and transforming activities in Rat-2 fibroblasts. J. Biol. Chem. 274: 26579–83.

59. Ikebe, M., T. Kambara, W.F. Stafford, M. Sata, E. Katayama, and R. Ikebe. 1998. A hinge at the central helix of the regulatory light chain of myosin is critical for

phosphorylation-dependent regulation of smooth muscle myosin motor activity. J. Biol. Chem. 273: 17702–7.

60. George, R. a, and J. Heringa. 2002. An analysis of protein domain linkers: their classification and role in protein folding. Protein Eng. 15: 871–879.

61. Wu, J., J.M. Jones, X. Nguyen-Huu, L.F. Ten Eyck, and S.S. Taylor. 2004. Crystal structures of RIalpha subunit of cyclic adenosine 5’-monophosphate (cAMP)-dependent protein kinase complexed with (Rp)-adenosine 3',5'-cyclic monophosphothioate and (Sp)-adenosine 3',5'-cyclic monophosphothioate, the phosphothioate analogues of cA. Biochemistry. 43: 6620–6629.

62. Saponaro, A., S.R. Pauleta, F. Cantini, M. Matzapetakis, C. Hammann, C. Donadoni, L. Hu, G. Thiel, L. Banci, B. Santoro, and A. Moroni. 2014. Structural basis for the mutual antagonism of cAMP and TRIP8b in regulating HCN channel function. Proc. Natl. Acad. Sci. U. S. A. 111: 14577–82.

63. Poolos, N.P., J.B. Bullis, and M.K. Roth. 2006. Modulation of h-Channels in Hippocampal Pyramidal Neurons by p38 Mitogen-Activated Protein Kinase. J. Neurosci. 26: 7995–8003.

64. B. Vanschouwen, M. Akimoto, Boulton S., K. Moleschi, R. Giri, and G. Melacini. 2015. CRCnetBASE - Assessing Cyclic Nucleotide Binding Domain Allostery and Dynamics by NMR Spectroscopy. Cyclic Nucleotide Signaling. 165-190.

65. Das, R., and G. Melacini. 2007. A model for agonism and antagonism in an ancient and ubiquitous cAMP-binding domain. J. Biol. Chem. 282: 581–593.

66. Das, R., M. Abu-Abed, and G. Melacini. 2006. Mapping allostery through equilibrium perturbation NMR spectroscopy. J. Am. Chem. Soc. 128: 8406–8407.

67. Abu-Abed, M., R. Das, L. Wang, and G. Melacini. 2007. Definition of an electrostatic relay switch critical for the cAMP-dependent activation of protein kinase A as revealed by the D170A mutant of RIalpha. Proteins. 69: 112–124.

68. McNicholl, E.T., R. Das, S. SilDas, S.S. Taylor, and G. Melacini. 2010. Communication between tandem cAMP binding domains in the regulatory subunit of protein kinase A-I?? as revealed by domain-silencing mutations. J. Biol. Chem. 285: 15523–15537.

69. Chow, S.S., F. Van Petegem, and E.A. Accili. 2012. Energetics of cyclic AMP binding to HCN channel C terminus reveal negative cooperativity. J. Biol. Chem. 287: 600–606.

70. Cook, P.F., M.E. Neville, K.E. Vrana, F.T. Hartl, and R. Roskoski. 1982. Adenosine cyclic 3’,5'-monophosphate dependent protein kinase: kinetic mechanism for the bovine skeletal muscle catalytic subunit. Biochemistry. 21: 5794–5799.

71. Singh, P., B.J. Harden, B.J. Lillywhite, and P.M. Broad. 2004. Identification of kinase inhibitors by an ATP depletion method. Assay Drug Dev. Technol. 2: 161–9.

72. Das, R., S. Chowdhury, M.T. Mazhab-Jafari, S. SilDas, R. Selvaratnam, and G. Melacini. 2009. Dynamically driven ligand selectivity in cyclic nucleotide binding domains. J. Biol. Chem. 284: 23682–23696.

73. León, D. a, W.R. Dostmann, and S.S. Taylor. 1991. Unfolding of the regulatory subunit of cAMP-dependent protein kinase I. Biochemistry. 30: 3035–3040.

74. Canaves, J.M., D.A. Leon, and S.S. Taylor. 2000. Consequences of cAMP-binding site mutations on the structural stability of the type I regulatory subunit of cAMP-dependent protein kinase. Biochemistry. 39: 15022–15031.

75. Palmer, A.G. 2004. NMR characterization of the dynamics of biomacromolecules. Chem. Rev. 104: 3623–3640.

76. Kleckner, I.R., and M.P. Foster. 2011. An introduction to NMR-based approaches for measuring protein dynamics. Biochim. Biophys. Acta. 1814: 942–68.

77. Taraska, J.W., M.C. Puljung, N.B. Olivier, G.E. Flynn, and W.N. Zagotta. 2009. Mapping the structure and conformational movements of proteins with transition metal ion FRET. Nat. Methods. 6: 532–537.

78. Liu, Z., Z. Gong, X. Dong, and C. Tang. 2015. Transient protein-protein interactions visualized by solution NMR. Biochim. Biophys. Acta. .

79. Zong, X., S. Krause, C.C. Chen, J. Kruger, C. Gruner, X. Cao-Ehlker, S. Fenske, C. Wahl-Schott, and M. Biel. 2012. Regulation of hyperpolarization-activated cyclic nucleotide-gated (HCN) channel activity by cCMP. J. Biol. Chem. 287: 26506–26512.

Chapter 2

C-Linker Control by the PKA RIα CBD-A

2.1 Author's Preface

The work presented in this chapter has previously been published and is reproduced here with permission from the Proceedings of the National Academy of Sciences USA. Full citation is as follows:

Akimoto, M., R. Selvaratnam, E.T. McNicholl, G. Verma, S.S. Taylor, and G. Melacini. 2013. Signaling through dynamic linkers as revealed by PKA. *Proc. Natl. Acad. Sci. U. S. A.* 110: 14231–6.

I conducted most of the experiments necessary for the manuscript. Dr. Rajeevan Selavaratnam validated the CHESCA analysis. Eric Tyler McNicholl and Geeta Verma purified catalytic subunit of PKA. S.S.Taylor provided the plasmids. I co-wrote the manuscript with Dr. Giuseppe Melacini.

2.2 Introduction

Regulation of signaling systems often relies on multi-domain proteins, which function as conformational switches controlled by allosteric effectors (1–13). The structural and dynamic changes experienced by folded domains during effector-dependent allosteric transitions have been extensively investigated (1–21). However, the current understanding of the allosteric role of partially unstructured linkers is at best scant. Although the role of covalent linkage in colocalization of protein domains is well known, it has recently been hypothesized that linkers, although generally quite flexible, have evolved to serve not simply as passive covalent threads connecting one domain to the next (i.e., "beads on-a-string" model), but also as active components of functionally relevant allosteric networks (22–25). To test this hypothesis, here we have investigated the allosteric role of a critical linker in the regulatory subunit (R) of protein kinase A (PKA). This linker bridges the inhibitory site (IS) and a critical cAMP-binding domain (CBD) of R [i.e., RIα (119-244) or CBD domain A (CBDA), ref. 26, Fig. 1A]. The R construct spanning the IS, the linker, and CBD-A [i.e., RIα (91-244) or RA in short, Fig. 1A] exhibits affinities for the catalytic subunit of PKA (C) and for cAMP as well as structures that are similar to those observed for longer RIα constructs (26–29). RA therefore inhibits C in a cAMP-dependent manner (27–29) and constitutes a functional regulatory unit. In addition, a similar R construct is also found fused to the RET oncogene kinase (30).

The structures of RA have been solved both in complex with C and cAMP (Fig. 1 B–E), providing the first picture of an R:C complex and revealing that CBD-A is composed of a structurally invariant β-subdomain and a more dynamic α-subdomain (27, 28, 31, 32). The α-subdomain tertiary structure changes dramatically depending on whether RA is bound to C or

to cAMP (Fig. 1 B–D). When bound to C, CBD-A adopts a conformation denoted as "H" (inhibited Holoenzyme or inactive, analogous to "T" in the original MWC model, ref. 4) state (Fig. 1 C and E) (31). In the H state, the inhibitory region docks in the active site of the kinase, and the α-subdomain of CBD-A provides additional contacts with C that result in an extended R:C interface, covering ~3,000 $Å^2$ (Fig. 1 C and E) (31). When bound to cAMP, CBD-A adopts a conformation denoted as "B" (active cAMP-Bound, analogous to "R" in the original MWC model, ref. 4) state (Fig. 1 B and D) (32). In apo RA, the H and B states coexist in a dynamic equilibrium (28), but their C *vs*. cAMP selectivity patterns are markedly different due to the H *vs*. B differences at the level of the α-subdomain. The C subunit exhibits higher affinity for the H- rather than the B state, whereas cAMP binds the B state more tightly than the H state, i.e., H and B represent the inactive and active forms of RA, respectively. As a result of the B selectivity of cAMP, cAMP binding to apo RA lowers the population of the H state, causing an effective weakening of the R:C interface and leading to the activation of PKA.

Whereas the crystal structures of the H and B states of RA (28, 31, 32) have been pivotal in understanding the cAMP-dependent activation of PKA, the allosteric role of the flexible RA linker [i.e., RIα (99-118)] remains elusive due to lack of electron density and to crystal packing for several linker residues (28, 32, 33). Does the RA linker control the cAMP-dependent activation of PKA? If so, how does cAMP affect the RA linker? Here, we address these questions using solution NMR and fluorescence and we propose a model showing that the RA linker, although dynamic and only partially structured, tunes the H *vs*. B equilibrium of apo RA. Using a thermodynamic linkage model tested through kinase bioassays, we also show that the position of the apo RA equilibrium is a key determinant of the

cAMP-dependent activation of PKA, although apo R is only transiently populated in vivo. In addition, the covariance analysis of NMR chemical shifts reveals that the RA linker is an active element of the cAMP-dependent allosteric networks controlling kinase function. Our results illustrate potentially general principles explaining how flexible linkers exploit weak but conformation-selective interactions to control enzymatic activity and to be in turn controlled by allosteric effectors.

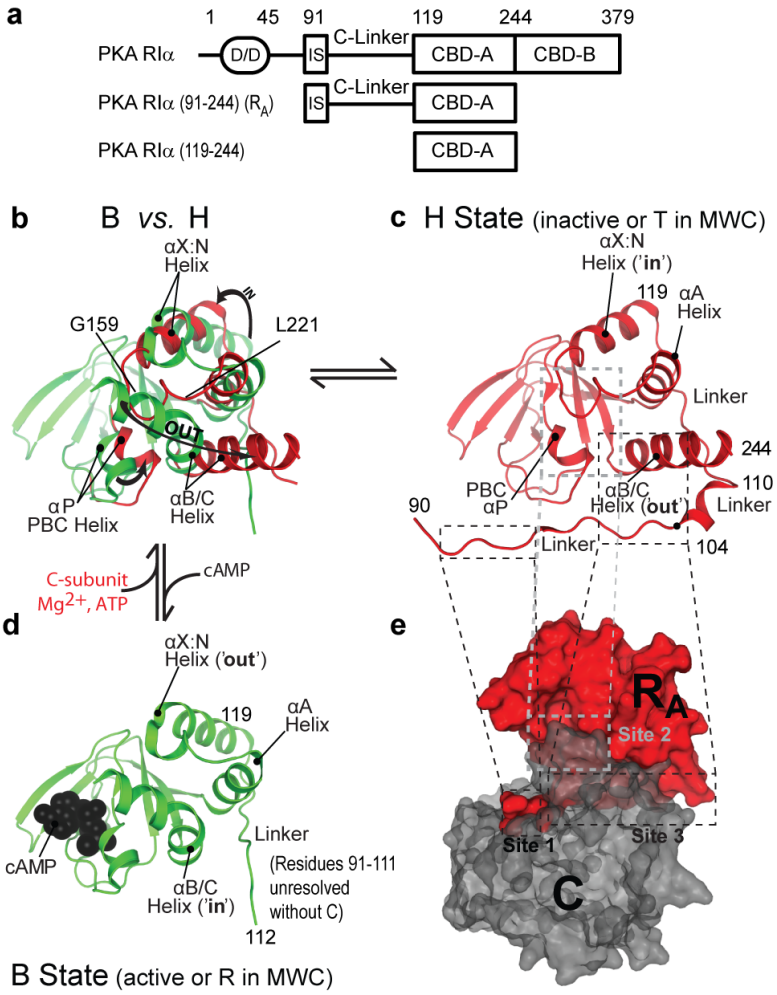

Figure 1: Construct design and architecture of PKA RIα and structures. (A) Domain organization of the RIα subunit of PKA (B–D) Structures of RIα (91-244) of PKA bound to either the C-subunit (H state, ref. 31, red) (C) or cAMP (B state, ref. 32, green) (D). (B) Superimposition of the H and B conformations. (E) Surface representation of the RIα (91-244):C holoenzyme structure with the C subunit shown in gray.

2.3 Results

2.3.1 The Impact of the Linker on the Globular cAMP-Binding Domain of RA Is Comparable to That of cAMP-Binding.

To probe the relevance of the RIα (91-118) linker, we compared the effects of linker deletion and of cAMP-binding. For this purpose, we measured both the apo RIα (91-244) *vs*. apo RIα (119-244) chemical shift differences (Fig. 2A, red bars) and the apo RIα (119-244) *vs*. cAMP-bound RIα (119-244) chemical shift map (Fig. 2A, black bars). Fig. 2A shows that both linker deletion and cAMP binding cause pervasive perturbations spanning the whole CBD-A [i.e., RIα (119-244)]. Although the extensive impact of cAMP binding is fully consistent with the long-range conformational changes expected for the H-to-B transition (Fig. 1B), the marked ppm variations caused by the linker deletion were somewhat unexpected because the linker is known to be only minimally structured based on prior H/D MS data (34). The lack of well-defined secondary structure in the linker is confirmed by the probability profiles derived from the secondary NMR chemical shifts (Fig. S1 A and B). Furthermore, the linker appears mostly flexible in the picosecond–nanosecond timescale, as indicated by the HN-NOE data (Fig. S1C). Given that the linker is only partially structured and flexible, it is likely that it interacts only weakly with CBD-A. To reconcile the weakness of the linker/CBD-A interactions with the pervasiveness of the linker effects on CBD-A (Fig. 2A), we propose a hypothesis based on two key notions. First, the linker/CBD-A interactions, although weak, are state-selective, i.e., the linker preferentially interacts with either the B or the H state of CBD-A. Second, the B and H free energies of apo RA are nearly degenerate (i.e.,$G_B \sim G_H$). The energetic degeneracy of the B and H states maximizes the sensitivity of the relative B *vs*. H populations to weak state-selective

interactions, as predicted by the theory of molecular sensors (35) and as illustrated for a simple two-state thermodynamic model in Fig. 2B. Fig. 2B shows that, when starting from a situation approaching free-energy degeneracy ($\Delta_{B,H}G$ = 0 kcal/mol) with equal populations for both states ($x_H = x_B = 0.5$), a state-selective interaction equivalent to as little as RT (~0.6 kcal/mol) results in a population change of ~50%. Weak but state-selective interactions of the linker have therefore the potential to cause global changes similar to those observed in Fig. 2A, provided that the B and H free energies in apo RA do not excessively deviate from near degeneracy (Fig. 2B, gray zone). To test this hypothesis we investigated further apo RA (36).

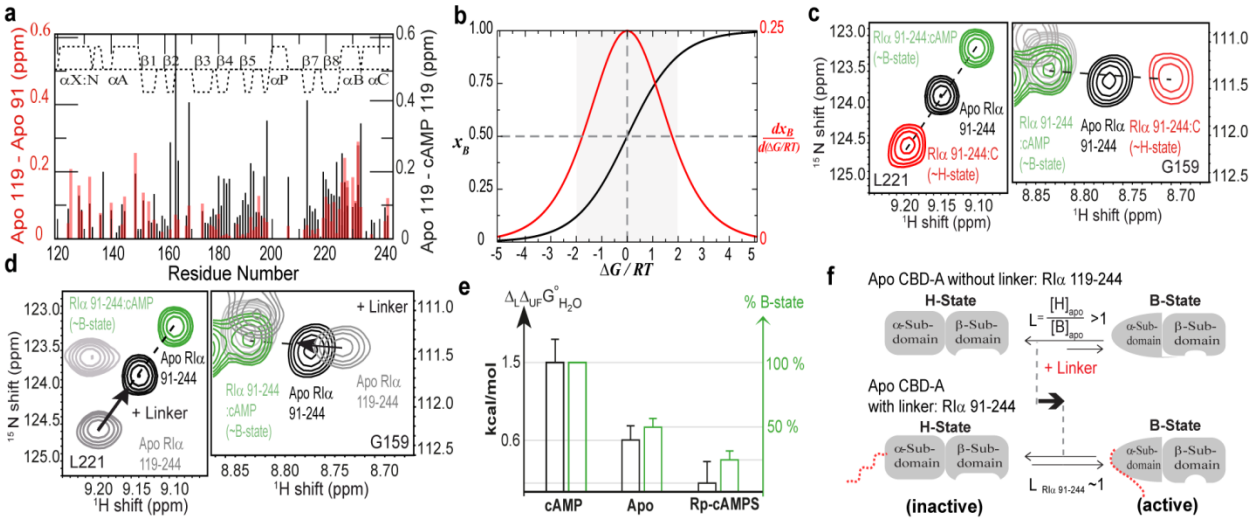

Figure 2: *RIα (91-118) linker shifts the B vs. H equilibrium of apo CBD-A toward the B state.* (A) apo RIα (119-244) vs. apo RIα (91-244) (red) and apo *vs*. cAMP-bound RIα (119-244) (black) chemical shift differences. (B) B-state molar fraction (x_B) *vs*. ΔG/RT (black) computed for a two-state equilibrium, where $\Delta G = G_H - G_B$. The red curve is the first derivative of x_B *vs*. ΔG/RT. (C) Representative H–N correlation peaks for apo, cAMP-, and C-bound RIα (91-244). (D) As C with C-bound RIα (91-244) replaced by apo RIα (119-244). Arrows indicate the effect of linker addition on the H vs. B equilibrium. (E) Correlation between the percent of B state in CBD-A and $\Delta_L\Delta_{UF}G^\circ_{H2O}$, which quantifies the strength of the linker–CBD interactions (Table S1). (F) Scheme for the linker-induced shift of the CBD-A H *vs*. B equilibrium.

2.3.2 The B and H States of apo CBD-A Are Nearly Degenerate and Thus the B and H Populations Are Highly Sensitive to Weak State-Selective Interactions Such as Those Between the Linker and CBD-A.

To assess the relative B *vs*. H populations of apo RA, we compared the HN correlation spectra of apo RA to those of the same construct bound to either C or cAMP, which approximate the H and B states, respectively (Fig. 2C). For several residues that are remote from the C- and cAMP-binding interfaces (Fig. S2 C and D), the apo, C-, and cAMP-bound cross-peaks exhibit a clearly linear pattern with the apo state observed in the middle of the two bound states (Fig. 2C). This linear pattern is conserved in longer R constructs (Fig. S2 A and B) and is indicative of fast chemical exchange (37) between the B and H states in apo RA. The central position of the apo cross-peaks (Fig. 2C) points to comparable B and H populations, i.e., near degeneracy of the B and H states. This finding provides initial support of our hypothesis about the sensitivity of CBD-A to weak state-selective interactions.

To test if the linker is able to provide state-selective interactions and consequently to modify the state populations, we compared the hetero-nuclear single quantum coherence (HSQC) spectra of apo and cAMP-bound RIα (91-244) with that of apo RIα (119-244), without the linker segment (Fig. 2D). Again a linear pattern was observed, with the peaks of apo RIα (119-244) shifted away from those of cAMP-bound RIα (91-244), which represents the B state (Fig. 2D). This observation suggests that the deletion of the (91-118) linker causes a consistent decrease in the population of the B state, pointing to B-selective linker/CBD-A interactions. To independently confirm this result and quantify the strength of the linker/CBD-A interactions, we measured the free energy of unfolding of both RIα (119-244) and RIα (91-244), each in the

apo, cAMP- and Rp-cAMPS–bound states (Fig. S3). The RpcAMPS analog is a well-known reverse-agonist of PKA that is selective for the H state of CBD-A and therefore it is useful to promote the stabilization of the inactive H state (Fig. S2E) (28).

2.3.3 The Linker Preferentially Interacts with the B- Rather than the H State of CBD-A.

The urea-unfolding profiles in Fig. S3 fully confirm the chemical shift-based results of Fig. 2D, indicating that the linker selectively interacts with the B- as opposed to the H state of CBD-A. The urea-induced unfolding of RA was monitored through intrinsic fluorescence and, because all of the Trp residues present in the RA constructs (i.e., W188 and W222) are confined to CBD-A (38), the fluorescence data of Fig. S3 report primarily on the unfolding of the globular CBD-A. Fig. S3A illustrates that in the presence of excess cAMP, whereby RA populates mainly the B state, the deletion of the (91-118) linker destabilizes CBD-A by about 1.5 kcal/mol (Table S1). However, when RA is bound to the Rp-cAMPS reverse-agonist and populates primarily the H state, the removal of the (91-118) linker does not result in any significant destabilization of CBD-A (Fig. S3B and Table S1), indicating that the interactions of the linker with the H state of CBD-A are negligible compared with those between the linker and the B state of CBD-A.

As a further control for the B *vs*. H selectivity in the linker/CBD-A interactions, we also examined the urea-induced unfolding of apo RA with state populations that are intermediate between those of the cAMP- and Rp-cAMPS-bound states (Fig. 2C and Fig. S3C). As expected, the variation in the free energy of unfolding caused by the linker deletion in apo RA is in between the corresponding values observed in the presence of cAMP and Rp-cAMPS (Fig. 2E and Table S1), further confirming the B *vs*. H selectivity of the linker/CBD-A interactions. Such state-selective interactions contribute a change in the B *vs*. H free-energy difference of ~1.4

kcal/mol (Fig. 2E and Table S1), which is slightly larger than 2RT ~ 1.2 kcal/mol (Fig. 2B) and corresponds to an approximately one-order of-magnitude variation in the B *vs*. H equilibrium constant (Fig.2F). Further proof of the B *vs*. H preferential interaction of the linker is provided by paramagnetic relaxation enhancements (PREs) (Fig. S4 D–F). The B-selective linker/CBD-A interactions lead to two major implications discussed below, i.e. (i) the RA linker is an active element of the cAMP-dependent allosteric networks of RA and (ii) the RA linker tunes both kinase inhibition and activation.

2.3.4 The cAMP-Dependent Allosteric Networks of RA Extend Beyond the Globular Domain to Sites Within the Linker Region

Because both cAMP and the linker interact preferentially with the B- as opposed to the H state of CBD-A (Fig. 2F), we anticipate that the allosteric networks controlled by cAMP reach sites in the linker region as well. To test this prediction, we implemented for RA the chemical shift covariance analysis (CHESCA), which has been shown to be effective in mapping effector-dependent networks in other allosteric systems based on a small library of agonist and antagonists (39). This library includes cAMP, the reverse-agonist Rp-cAMPS, the partial agonist 2'-OMe-cAMP, and the agonist Sp-cAMPS (27, 40). Based on the residue-specific chemical shift changes caused by these ligands (Fig. S4 A and B), we computed a residue *vs*. residue correlation matrix (Fig. 3A). Fig. 3A clearly indicates that several correlations occur between the flexible linker region and the globular CBD-A (red highlight), providing initial support of our hypothesis about the coupling between cAMP and the linker. A further confirmation of this hypothesis is provided by agglomerative clustering (AC), which reveals that the largest residue

cluster derived from the correlation matrix of Fig.3A spans both CBD-A and several sites within the linker region (Fig. 3 A and B).

The AC residue cluster spanning both the linker and CBD-A (Fig. 3 A and B) underlies the cAMP-dependent activation of PKA, because the linear chemical shift correlations defining such network exhibit a point distribution that correlates well with PKA function: the active (i.e., cAMP and Sp-cAMPS) and inactive (i.e., apo and Rp-cAMPS) forms of RA are well separated (Fig. 3 C and D), with the partial agonist 2'-OMe-cAMP found in between these two sets (Fig. 3 C and D). Because the PKA activation profiles of these cAMP analogs were originally measured for the full-length R subunit (40), the CHESCA results (Fig. 3 C and D) support the relevance of the RA construct used in these NMR analyses. Note that the AC cluster underlying the cAMP dependent activation of PKA includes the RA residues used in Fig. 2C (i.e., L221 and G159), confirming the suitability of these residues to monitor the B *vs*. H equilibrium independently of potentially obscuring binding effects. The results from the AC analysis are also more formally and more generally confirmed by the singular value decomposition (SVD) (Fig. S4C and Table S2) of the chemical shift matrix (SI Text) (39).

Overall, the CHESCA of RA (Fig. 3 and Fig. S4) corroborates our hypothesis that, although flexible, the RA linker is not simply a passive covalent thread between the inhibitory sites and CBD-A, but an active element of the functional allosteric network of RA. In particular, Fig. 3A reveals that several residues in the 112-116 linker region define a contiguous segment involved in extensive correlations with multiple CBD-A residues, suggesting that at least some of these residues may contribute to the preferential B *vs*. H interactions of the linker with CBD-A. This prediction was tested using two representative and previously undescribed point

mutations targeting the 112-116 site, i.e., R113A and I116A. These mutants are expected to cause a loss of B-selective interactions and therefore to result in a shift of the apo RA equilibrium away from the B state. Such expected equilibrium shift was observed in the HSQC spectra of both mutants, showing that the peaks of apo R113A-RA and of apo I116A-RA shift away from those measured for cAMP-bound wt-RA (Fig. S5E).

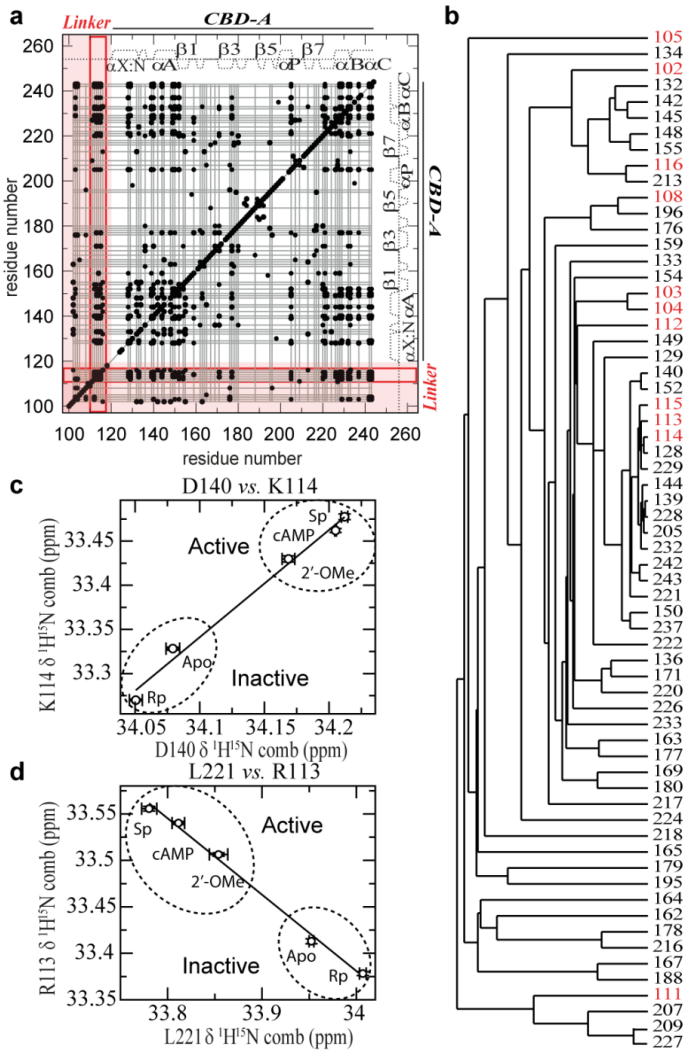

Figure 3: cAMP-dependent allosteric network of R reaches the linker region.(A) Chemical shift correlation matrix of RIα (91-244). Black dots identify residue pairs with absolute correlation coefficients ≥0.98. Grid lines connect residues in the largest agglomerative cluster (cluster 1). The linker region is highlighted in red. Key CBD-A/linker correlations are boxed by red lines. (B) Cluster 1 dendrogram. Residues linked through the dendrogram are labeled. Linker residues are in red. (C and D) Representative interresidue chemical shift correlations involving the linker region.

The B-state selective linker/CBD-A interactions mediated by R113 appear significant enough to result in B *vs*. H differential solvent exposure, as probed by H/H exchange (Fig. S5 A–D). The H/H exchange spectra were acquired for both the cAMP- and the Rp-cAMPS-bound forms of RA, which promote the stabilization of the B and H states of CBD-A, respectively (Fig. S5 A–D). The comparative cAMP *vs*. Rp-cAMPS H/H analysis reveals that residues 111-114 are more exposed in the Rp-cAMPS-bound form than in the presence of cAMP (Fig. S5 B and D, dotted box), confirming that R113 and the adjacent residues define a key site for the B-selective interaction of the linker with CBD-A. In agreement with these findings, the side chain of R113 forms multiple salt bridges with CBD-A residues (i.e., D146 and D149) in several crystal structures solved in the presence of cAMP or the Sp-cAMPS agonist (Fig. S6 E–G) (28, 33).

The salt bridges between R113 and D146/D149 detected in the crystal structures of Fig. S6 E–G are most likely preserved also in solution for the B state of RA, as confirmed by the H/H data of Fig. S5 A–D showing that several residues in the 141-150 region are more exposed in the Rp-cAMPS–bound form than in the presence of cAMP, similarly to what is observed for R113. However, it would have been challenging to establish the B-state selectivity of the linker/CBD-A contacts solely based on the crystal structures, because R113 is affected by crystal packing (28, 33) and R113 interacts with CBD-A also in the RA:C complex (Fig. S6 C and D) (31). In addition, the linker/CBD-A interface is significantly more extended in the RA:C complex (Fig. 1C) than in the RA:cAMP complex (Fig. 1D). In the former the linker becomes more structured by docking into the active site of C (Fig. 1E), whereas in the latter no electron density was observed for residues 91-111 of the linker (Fig. 1D). However, R113 mediates B-selective interactions, which are likely to be a feature shared by all PKA R-subunit isoforms because this

residue is conserved (Fig. S6A). Such state selective linker/CBD-A interactions loci are critical to tune the position of the B *vs*. H equilibrium in apo RA, as schematically illustrated in Fig. 4A.

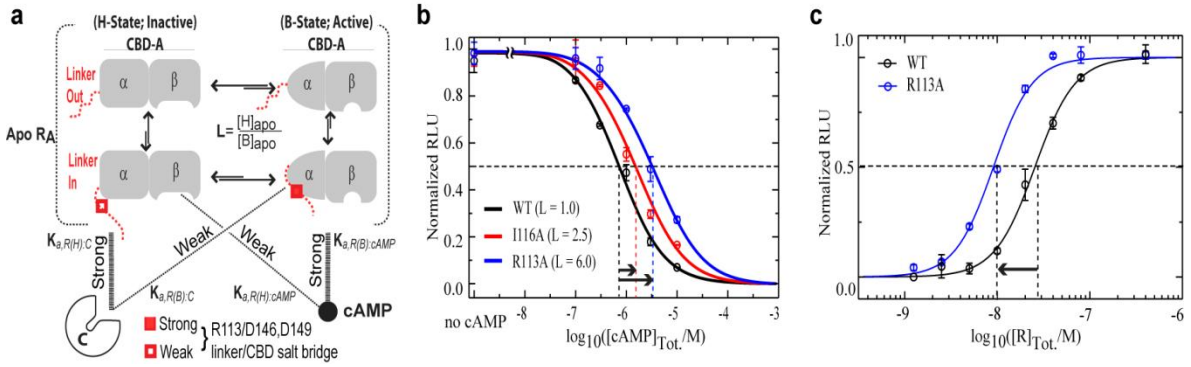

Figure 4: Linker controls both inhibition and activation of PKA by modulating the B vs. H equilibrium of apo CBD-A. (A) Thermodynamic model of cAMP dependent activation of PKA. The linker (red) is dynamic and samples conformations in which it is fully solvent exposed ("linker out" and conformations in which it transiently approaches the well-folded CBD-A ("linker in"), preferentially interacting with the B state of CBD-A (gray) and shifting the overall H vs. B apo equilibrium toward its midpoint (i.e., L = $[H]_{apo}/[B]_{apo}$ ~ 1). The H and B conformations exhibit high affinity for C and cAMP, respectively (thick lines), but weaker cross-interactions occur (thin dotted lines) (Table S3). The α- and β-subdomains of CBD-A are shown schematically in both the inactive (H) and active (B) conformations. (B) PKA activation by cAMP for wt RIα (91-244) (black circles) and the I116A (red circles) and R113A (blue circles) mutants, which weaken the B-selective interaction of the linker with CBD-A. Data were fit by activation curves (solid lines) computed based on the thermodynamic model in A (SI Text). (C) PKA inhibition by wt (black) and R113A (blue) RIα (91-244).

2.3.5 The RA Linker Tunes both Kinase Inhibition and Activation.

To evaluate how the B *vs*. H equilibrium of apo RA affects the cAMP dependent activation of PKA, we developed a thermodynamic linkage model (Fig. 4A), which takes into account not only the selectivity of C and cAMP for the H and B states, respectively, but also the possibility of weaker cross-interactions (i.e., C:B state and cAMP:H state, Table S3 and Eq. S1–S10). This model reproduces well the experimental profile for the cAMP-dependent activation of C inhibited by wt RA (Fig. 4B) and predicts that, although the apo form of the PKA R subunit is only transiently and minimally populated in vivo, the position of the B *vs*. H

equilibrium of apo R (i.e., $L = [H]_{apo}/[B]_{apo}$) is a key determinant of PKA inhibition and activation. As L increases, the average affinity of R for C (Ka,R:C) and the EC50 for the cAMP-dependent activation of PKA are both predicted to increase (Eq. S5 and Fig. S5F). These predictions were experimentally tested using the R113A mutant, which leads to increased L values, as proved by NMR (Fig. S5E). As expected based on the NMR data, the R113A mutation in the linker leads to several-fold increased EC50 and Ka, R:C values relative to wt (Fig. 4B and C and Fig. S5F), further confirming the thermodynamic model of Fig. 4A and the role of the linker in tuning both kinase inhibition and activation.

2.4 Discussion

Our results directly support the notion that the dynamic RA linker serves the function of tuning the inhibition and the activation of PKA through weak but state-selective interactions, such as those mediated by R113 and I116, whose impact is amplified by the free energy near degeneracy of apo RA. Considering that both residues are remote from the R:C and R:cAMP interfaces (Fig. S6 B and I) the effect of these sites on PKA activation is remarkable. Also unexpected was the enhanced stability of the RA:C holoenzyme resulting from the R113A mutation (Fig. 4C), despite the loss of the salt bridges mediated by the R113 guanidinium in RA:C (Fig. S6 C and D). These linker/H-state contacts are not affected by crystal packing and the apparently counterintuitive enhancement in the affinity of RA for C caused by the R113A RA mutation is explained considering that the salt bridges formed by R113 in C-bound wt RA (H state; Fig. S6 C and D) are weaker than those generated by R113 in the B state of apo wt RA (Fig. 5A and Fig. S6 E–G). Consequently, the R113A mutation causes only a marginal increase in the

free energy of the RA:C complex, but a more significant increase in the free energy of apo RA, which samples the B state as well (Fig. 5). The overall net effect of the R113A mutation in RA is to increase the magnitude of the binding free energy for the RA:C complex (Fig. 5), i.e., R113A RA is a more potent kinase inhibitor than wt RA, as observed in Fig. 4C.

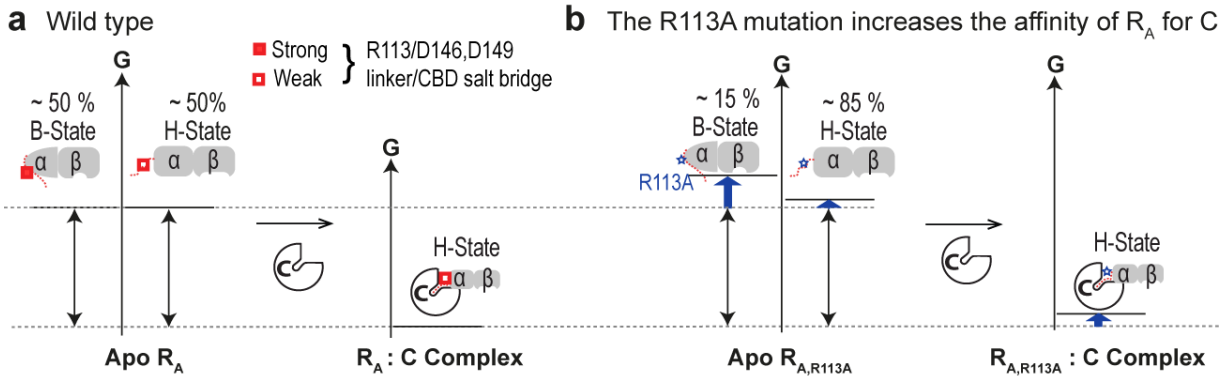

Figure 5: Effect of the R113A R_A linker mutation on the binding free energy of the R_A:C kinase-inhibitory complex. (A) Free-energy changes occurring upon formation of the wt R_A:C complex. The C subunit selects primarily for the H state of apo wt R_A. (B) As in A but for the R113A R_A:C complex. In apo R113A R_A, the H state is more populated than in apo wt R_A, because R113 forms stable salt bridges in the B- but not in the H state of apo wt R_A. For clarity, the weak cross-interactions between C and the B state of apo R_A are not shown.

The enhanced stability of the R113A RA:C complex *vs*. the wt RA:C complex (Figs. 4C and 5) suggests that the interactions mediated by the R113 guanidinium in the wt RA:C complex (Fig. S6 C and D) are frustrated, although the contacts between the R113 guanidinium and the H state of CBD-A are partially stabilized by the C subunit as the IS at the N terminus of the linker is recruited into the active site of the kinase (Fig. 1 C and E). The local structural frustration (41) originating from the RA linker within the inhibitory RA:C complex is absent in cAMP-bound RA, because cAMP selects for the B state of CBD-A. Therefore, we conclude that structurally

frustrated linkers have evolved to assist small molecules, such as cAMP, in effectively disrupting large (~3,000 Å^2) protein–protein interfaces, such as that in the RA:C complex.

In conclusion, we have shown that the dynamic linker of the functional RA construct of PKA (Fig. 1A) controls the position of the active *vs*. inactive conformational equilibrium of the apo cAMP-binding domain A (CBD-A). The active *vs*. inactive near degeneracy of the apo CBD-A amplifies the functional impact of weak but state-selective linker/CBD-A interactions, e.g., salt bridges between R113 in the linker and D146/D149 in CBD-A, which are preferentially formed in the B state (active) rather than the H state (inactive) of CBD-A. These state-selective linker/CBD-A interactions result in an effective coupling between the linker and CBD-A. We have shown both theoretically and experimentally that such linker/CBD-A coupling leads to two previously unanticipated consequences. First, the cAMP-dependent allosteric networks of RA unexpectedly extend well beyond the folded CBD-A domain to the more flexible linker. Second, the effect of the linker on the minimally populated apo RA intermediate is critical to tune not only the cAMP sensitivity of kinase activation (EC50), but also kinase inhibition (IC50). This is because the RA inhibitory interface, which selects for the H state of CBD-A, is formed at the expense of locally destabilizing the intramolecular linker/CBD-A interactions; i.e., the linker includes discrete sites of local structural frustration in the RA:C inhibitory complex. Such frustration has evolved to assist the disruption of large protein–protein interfaces by small allosteric ligands and, when relieved by deletion mutations (e.g., R113A), leads to an R construct with enhanced kinase inhibitory potency without affecting the R:C interface. Overall, our results imply that not all multi-domain proteins are adequately described by a beads-on-a-string model because selected linkers provide an additional level of functional

regulation that goes beyond the colocalization of different structural modules, suggesting that multi-domain systems are not only the product of gene fusion but of a higher degree of evolution. In addition, although the results presented here apply to the monomeric deletion RIα constructs used, they provide a necessary first step toward the full assessment of the role of the linker interactions in longer RIα constructs and in the quaternary structure of PKA.

2.5 Materials and Methods

Details for protein expression and purification, NMR data acquisition for the RIα (91-244), holoenzyme RIα (91-244):C complex, and for RIα (91-379), thermodynamic modeling and measurements of PKA inhibition, and cAMP dependent activation are provided in SI Text. RIα (119-244) were expressed and purified according to previously published protocols (42–44). All spectra were recorded at a temperature of 306 K on a Bruker AV 700 spectrometer equipped with TCI cryoprobe. All spectra were processed with NMRpipe (45) using linear prediction, unless otherwise specified, and a resolution-enhancing 60° shifted sine-squared bell window function. The NMR spectra were analyzed with Sparky (46) using Gaussian line-fitting. Assignments were obtained either through triple-resonance 3D experiments [i.e. HNCO, HNCA, HN(CO)CA, CBCA(CO)NH, and HNCACB] (47) and/or through spectral comparisons, if no ambiguities were present. HN NOE data were acquired as previously reported (48, 49) and processed without linear prediction. A 10-s recycle delay was used to include a 5-s proton saturation period. Data were collected in 10 sets of saturated and unsaturated interleaved spectra. All spectra were co-added before processing using NMRpipe, resulting in a total of 40 scans per serial file for each NOE experiment (with and without ^{1}H saturation). The steady-state

NOE values were computed as the ratio of the intensities in saturated to unsaturated spectra. The error on the NOE values were gauged based on the SD between fit heights in replicate spectra. Some of the least sensitive NMR experiments were acquired using the RIα (96-244) construct, which is more soluble than RIα (91-244) but preserves very similar spectra, i.e., 94% of RIα (96-244) HSQC peaks are overlapped with those of RIα (91-244). The secondary structure probabilities were determined using the secondary chemical shifts via the PECAN software (50). Combined chemical shift changes in Fig. 2A were measured as $\sqrt{(\Delta\delta^1H^2+0.2^2\Delta\delta^{15}N^2)}$. In Fig. 2E, the percent of B state was assessed using four residues that sense the position of the H *vs*. B equilibrium (i.e., V115, G178, G223, and L221) and assuming that the RIα (91-244):C and RIα (91-244):cAMP complexes represent the H and B states, respectively.

Uniformly ^{15}N-labeled RIα (91-244) was concentrated to 10 µM in 50 mM Mops (pH 7), 100 mM NaCl, 10 mM $MgCl_2$, 5 mM DTT, 0.02 mM ^{15}N-acetyl-glycine, 0.02% sodium azide, and 5% ^2H_2O. Because the apo state and the four ligand-bound states (i.e., Rp-cAMPS-, Sp-cAMPS-, cAMP-, and 2'-OMe-cAMP bound states) were used as the five perturbation sets for CHESCA, stock solutions of Rp-cAMPS, Sp-cAMPS, 2'OMe-cAMP (BIOLOG), and cAMP (Sigma) were prepared using the same buffer as for the protein solution. Starting from the apo samples, stock solutions of the cyclic nucleotide ligands (25 mM) were titrated into the protein solution to full saturation (the final concentrations of ligands were 3 mM). Sensitivity-enhanced ^1H ^{15}N-HSQC spectra with 256 (t1) and 1024 (t2) complex points and spectral widths of 31.82 and 14.06 ppm for the ^{15}N and ^1H dimensions, respectively, were recorded with 128 scans and a recycle delay of 1.70 s. The ^1H and ^{15}N carrier frequencies were set at the water resonance and in the middle of the amide region, respectively. The combined ^{15}N and ^1H chemical shifts (δ^1H +

0.2xδ^{15}N) from the HSQC spectra of apo and Rp-cAMPS-, Sp-cAMPS-, cAMP-, and 2'-OMe-cAMP-bound RIα (91-244) referenced to ^{15}N-acetylglycine were compiled into a chemical shift matrix, which was then analyzed using AC and SVD, according to previously published protocols (39). All nodes in the dendrogram of Fig. 3B correspond to correlation coefficients with absolute values ≥0.98.

2.6 Acknowledgement

We thank Dr. F. Fogolari, Dr. D. Blumenthal, Dr. A. Kornev, Dr. M. Keshwani, L. Matthews, B. VanSchouwen, and M. Elgamal for helpful discussions, and the Canadian Institute of Health Research (G.M.) and the National Sciences and Engineering Research Council (G.M.) for financial support. We are also grateful to Prof. Brian E. McCarry (1946-2013) for his contributions to the NMR Facilities of McMaster University used for this work.

2.7 References

1. Kuriyan J, Eisenberg D (2007) The origin of protein interactions and allostery in colocalization. Nature 450(7172):983–990.
2. Ruschak AM, Kay LE (2012) Proteasome allostery as a population shift between interchanging conformers. Proc Natl Acad Sci USA 109(50):E3454–E3462.
3. Vendruscolo M (2011) Protein regulation: The statistical theory of allostery. Nat Chem Biol 7(7):411–412.
4. Changeux JP, Edelstein SJ (2005) Allosteric mechanisms of signal transduction. Science 308(5727):1424–1428.
5. Gardino AK, et al. (2009) Transient non-native hydrogen bonds promote activation of a signaling protein. Cell 139(6):1109–1118.
6. Kern D, Zuiderweg ER (2003) The role of dynamics in allosteric regulation. Curr Opin Struct Biol 13(6):748–757.
7. Aghazadeh B, Lowry WE, Huang XY, Rosen MK (2000) Structural basis for relief of autoinhibition of the Dbl homology domain of proto-oncogene Vav by tyrosinephosphorylation. Cell 102(5):625–633.
8. Long D, Brüschweiler R (2011) Atomistic kinetic model for population shift and allostery in biomolecules. J Am Chem Soc 133(46):18999–19005.
9. Smock RG, Gierasch LM (2009) Sending signals dynamically. Science 324(5924):198–203.
10. Tzeng SR, Kalodimos CG (2009) Dynamic activation of an allosteric regulatory protein. Nature 462(7271):368–372.
11. Boehr DD, Nussinov R, Wright PE (2009) The role of dynamic conformational ensembles in biomolecular recognition. Nat Chem Biol 5(11):789–796.
12. Religa TL, Sprangers R, Kay LE (2010) Dynamic regulation of archaeal proteasome gate opening as studied by TROSY NMR. Science 328(5974):98–102.
13. Hayashi I, Wilde A, Mal TK, Ikura M (2005) Structural basis for the activation of microtubule assembly by the EB1 and p150Glued complex. Mol Cell 19(4):449–460.
14. Berman HM, et al. (2005) The cAMP binding domain: An ancient signaling module. Proc Natl Acad Sci USA 102(1):45–50.
15. Popovych N, Sun S, Ebright RH, Kalodimos CG (2006) Dynamically driven protein allostery. Nat Struct Mol Biol 13(9):831–838.
16. Manley G, Loria JP (2012) NMR insights into protein allostery. Arch Biochem Biophys 519(2):223–231.

17. Masterson LR, et al. (2010) Dynamics connect substrate recognition to catalysis in protein kinase A. Nat Chem Biol 6(11):821–828. 18. Ishiyama N, et al. (2010) Dynamic and static interactions between p120 catenin and E-cadherin regulate the stability of cell-cell adhesion. Cell 141(1):117–128.

19. Tzeng SR, Kalodimos CG (2012) Protein activity regulation by conformational entropy. Nature 488(7410):236–240.

20. Dhulesia A, Gsponer J, Vendruscolo M (2008) Mapping of two networks of residues that exhibit structural and dynamical changes upon binding in a PDZ domain protein. J Am Chem Soc 130(28):8931–8939.

21. Marlow MS, Dogan J, Frederick KK, Valentine KG, Wand AJ (2010) The role of conformational entropy in molecular recognition by calmodulin. Nat Chem Biol 6(5):352–358.

22. Sarkar P, Saleh T, Tzeng SR, Birge RB, Kalodimos CG (2011) Structural basis for regulation of the Crk signaling protein by a proline switch. Nat Chem Biol 7(1):51–57.

23. Ahmad A, et al. (2011) Heat shock protein 70 kDa chaperone/DnaJ cochaperone complex employs an unusual dynamic interface. Proc Natl Acad Sci USA 108(47):18966–18971

24. Ma B, Tsai CJ, Haliloglu T, Nussinov R (2011) Dynamic allostery: Linkers are not merely flexible. Structure 19(7):907–917.

25. Zhuravleva A, Gierasch LM (2011) Allosteric signal transmission in the nucleotidebinding domain of 70-kDa heat shock protein (Hsp70) molecular chaperones. Proc Natl Acad Sci USA 108(17):6987–6992.

26. Kornev AP, Taylor SS, Ten Eyck LF (2008) A generalized allosteric mechanism for cisregulated cyclic nucleotide binding domains. PLOS Comput Biol 4(4):e1000056.

27. Anand GS, et al. (2010) Cyclic AMP- and (Rp)-cAMPS-induced conformational changes in a complex of the catalytic and regulatory (RIα) subunits of cyclic AMP-dependent protein kinase. Mol Cell Proteomics 9(10):2225–2237

28. Badireddy S, et al. (2011) Cyclic AMP analog blocks kinase activation by stabilizing inactive conformation: Conformational selection highlights a new concept in allosteric inhibitor design. Mol Cell Proteomics 10:M110.004390.

29. Huang LJ, Taylor SS (1998) Dissecting cAMP binding domain A in the RIalpha subunit of cAMP-dependent protein kinase. Distinct subsites for recognition of cAMP and the catalytic subunit. J Biol Chem 273(41):26739–26746.

30. Bongarzone I, et al. (1993) Molecular characterization of a thyroid tumor-specific transforming sequence formed by the fusion of ret tyrosine kinase and the regulatory subunit RI α of cyclic AMP-dependent protein kinase A. Mol Cell Biol 13(1):358–366.

31. Kim C, Xuong NH, Taylor SS (2005) Crystal structure of a complex between the catalytic and regulatory (RIalpha) subunits of PKA. Science 307(5710):690–696.

32. Su Y, et al. (1995) Regulatory subunit of protein kinase A: Structure of deletion mutant with cAMP binding domains. Science 269(5225):807–813.

33. Wu J, Jones JM, Nguyen-Huu X, Ten Eyck LF, Taylor SS (2004) Crystal structures of RIalpha subunit of cyclic adenosine 5'-monophosphate (cAMP)-dependent protein kinase complexed with (Rp)-adenosine 3',5'-cyclic monophosphothioate and (Sp)-adenosine 3',5'-cyclic monophosphothioate, the phosphothioate analogues of cAMP. Biochemistry 43(21):6620–6629.

34. Hamuro Y, et al. (2004) Mapping intersubunit interactions of the regulatory subunit (RIalpha) in the type I holoenzyme of protein kinase A by amide hydrogen/deuterium exchange mass spectrometry (DXMS). J Mol Biol 340(5):1185–1196.

35. Vallée-Bélisle A, Ricci F, Plaxco KW (2009) Thermodynamic basis for the optimization of binding-induced biomolecular switches and structure-switching biosensors. Proc Natl Acad Sci USA 106(33):13802–13807.

36. Das R, Abu-Abed M, Melacini G (2006) Mapping allostery through equilibrium perturbation NMR spectroscopy. J Am Chem Soc 128(26):8406–8407.

37. Palmer AG, 3rd (2004) NMR characterization of the dynamics of biomacromolecules. Chem Rev 104(8):3623–3640.

38. Leon DA, Canaves JM, Taylor SS (2000) Probing the multidomain structure of the type I regulatory subunit of cAMP-dependent protein kinase using mutational analysis: Role and environment of endogenous tryptophans. Biochemistry 39(19):5662–5671.

39. Selvaratnam R, Chowdhury S, VanSchouwen B, Melacini G (2011) Mapping allostery through the covariance analysis of NMR chemical shifts. Proc Natl Acad Sci USA 108(15):6133–6138.

40. Christensen AE, et al. (2003) cAMP analog mapping of Epac1 and cAMP kinase. Discriminating analogs demonstrate that Epac and cAMP kinase act synergistically to promote PC-12 cell neurite extension. J Biol Chem 278(37):35394–35402.

41. Ferreiro DU, Hegler JA, Komives EA, Wolynes PG (2011) On the role of frustration in the energy landscapes of allosteric proteins. Proc Natl Acad Sci USA 108(9):3499–3503.

42. Das R, Melacini G (2007) A model for agonism and antagonism in an ancient and ubiquitous cAMP-binding domain. J Biol Chem 282(1):581–593.

43. Das R, et al. (2007) cAMP activation of PKA defines an ancient signaling mechanism. Proc Natl Acad Sci USA 104(1):93–98.

44. Das R, et al. (2009) Dynamically driven ligand selectivity in cyclic nucleotide binding domains. J Biol Chem 284(35):23682–23696.

45. Delaglio F, et al. (1995) NMRPipe: A multidimensional spectral processing system based on UNIX pipes. J Biomol NMR 6(3):277–293.

46. Goddard TD, Kneller DG (2006) Sparky 3 (Univ California, San Francisco).

47. Sattler M, Schleucher J, Griesinger C (1999) Heteronuclear multidimensional NMR experiments for the structure determination of proteins in solution employing pulsed field gradients. Prog Nucl Magn Reson Spectrosc 34:93–158.

48. Renner C, Schleicher M, Moroder L, Holak TA (2002) Practical aspects of the 2D 15N-[1h]-NOE experiment. J Biomol NMR 23(1):23–33.

49. Das R, et al. (2008) Entropy-driven cAMP-dependent allosteric control of inhibitory interactions in exchange proteins directly activated by cAMP. J Biol Chem 283(28): 19691–19703.

50. Eghbalnia HR, Bahrami A, Wang L, Assadi A, Markley JL (2005) Probabilistic identi-fication of spin systems and their assignments including coil-helix inference as output (PISTACHIO). J Biomol NMR 32(3):219–233.

2.8 Supplementary Information: Material Methods

Protein Expression and Purification: Bovine RIα (91-244) was subcloned into a pTriEX vector as a rare codon optimized fusion construct with His_6-SUMO connected to the N-terminus of RIα by a TEV cleavable linker RIα (91-244) was then expressed in the Escherichia coli strain BL-21(DE3). Cells were grown in M9 minimal media and induced with 0.5 mM Isopropyl β-D-1-thiogalactopyranoside at an optical density of 0.6-0.9 (λ=600 nm), and further incubated at 18-20 degree for 16 hrs. After harvesting, the cells were re-suspended in the lysis buffer (50 mM MOPS, pH 7 with 100 mM NaCl) and lysed by French Press. The cell lysate was centrifuged and the supernatant was further purified by Ni-NTA affinity chromatography with wash buffer (50 mM MOPS, pH 7 with 0.5 M NaCl and 20 mM imidazole) and elution buffer (50 mM MOPS, pH 7 with 0.5 M NaCl and 250 mM imidazole). The His_6-SUMO was cleaved by His6-tagged TEV protease prior to a second Ni^{2+} column purification to remove both the cleaved His6-SUMO and TEV. The cleaved protein was purified by gel filtration on a Superdex 75 column. Uniformly ^{13}C and ^{15}N labeled RIα (96-244) subcloned into the pRSET vector was expressed and purified according to the previously described protocols for RIα (119-244). To prepare the apo sample, the purified protein was unfolded with 8 M Urea and refolded by dialysis against a 20 mM MOPS buffer (pH 7 containing 100 mM KCl, 5 mM β-ME and 0.5 mM EDTA) with two buffer exchanges. After refolding the protein was further purified through size exclusion chromatography. All mutants were prepared by site directed mutagenesis.

H/H Exchange: The H/H exchange rates between water and the backbone amide protons were measured using the CLEANEX-PM-FHSQC experiment (1) for Rp-cAMPS- and cAMP-bound ^{15}N-labeled RIα (91-244). For this purpose, the protein was concentrated to 10

μM in 50 mM MOPS (pH 7), 100 mM NaCl, 10 mM $MgCl_2$, 5 mM DTT, 0.02 % sodium azide and 5 % ^2H_2O. For the cAMP- and Rp-cAMPS-bound states, 1 mM cAMP and 1 mM Rp-cAMPS were added to the protein samples, respectively. The ^1H and ^{15}N carrier frequencies were set at the water resonance and in the middle of the amide region, respectively. A total of 88 scans were accumulated with an inter-scan delay of 2 s and an RF strength of 6.9 kHz for the CLEANEX-PM mixing block, which minimizes offset effects. The mixing time was 80 ms.

Urea Unfolding: Apo RIα (91-244) and apo RIα (119-244) were incubated for 3 hours at room temperature with increasing concentrations of urea (0-8 M). For the cAMP- and Rp-cAMPS-bound samples, 100-fold excess cAMP and Rp-cAMPS in the assay buffer (50 mM MOPS, pH 7 containing 100 mM NaCl, 10 mM $MgCl_2$) were used. The final protein concentration was 5 μM. All fluorescence measurements were performed with a TECAN infinite M200. The samples were excited at 293 nm and the resulting emission spectra were followed from 335 nm to 365 nm. The fluorescence intensity ratio (353 nm/340 nm) was used to follow the shift in wavelength caused by the unfolding of the cAMP-binding domain A (CBD-A)(2). Unfolding curves (Fig. S3) were calculated using the following equation: $X_U=(R_{obs}-R_N)/(R_U-R_N)$, where X_U is the fraction of unfolded protein, Robs is the observed ratio of intensity at various urea concentrations. R_N and R_U are Robs of the fully folded and unfolded states, respectively. A two-state model was used to calculate the free energy of unfolding ΔG according to $\Delta G_{unfolding}=-RTln(X_U/X_N)$ with $X_N + X_U = 1$, where X_N is the fraction of native protein. ΔG^{H2O} and m were calculated using the equation $\Delta G=\Delta G^{H2O}+m[Urea]$, where ΔG^{H2O} is the free energy of unfolding in the absence of denaturant.

NMR of the Holoenzyme RIα (91-244):C Complex: ^{2}H,^{15}N-labeled RIα (91-244) was prepared using deuterated M9 media. The C-subunit of PKA was expressed and purified from the Escherichia coli strain BL-21(DE3) according to established protocols (3). Holoenzyme was formed overnight by mixing PKA C and apo ^{2}H,^{15}N-labeled RIα (91-244) at a 1.2:1 ratio and purified by gel filtration to separate the RIα (91-244):C complex from the free RIα (91-244). The holoenzyme sample was then concentrated to 0.2 mM in 50 mM MOPS (pH 7), 100 mM NaCl, 10 mM $MgCl_2$, 5 mM DTT, 1 mM AMP-PNP, 0.02 % sodium azide and 5 % $^{2}H_2O$. Transverse-relaxation optimized spectroscopy (TROSY) 2D experiments with 80 (t1) and 1024 (t2) complex points and spectral widths of 31.82 ppm and 15.94 ppm for the ^{15}N and ^{1}H dimensions, respectively, were recorded with 12 scans and a recycle delay of 1.70 s.

NMR of RIα (91-379): ^{2}H,^{15}N-labeled RIα (91-379) was prepared using deuterated M9 media. The apo sample was prepared according to the previously described protocols for the RIα (91-244). apo ^{2}H,^{15}N-labeled RIα (91-379) was concentrated to 0.2 mM in 50 mM Mops (pH 7), 100 mM NaCl, 10 mM $MgCl_2$, 5 mM DTT, 0.02mM^{15}N-acetylglycine, 0.02% sodium azide, and 5% $^{2}H_2O$. For the cAMP-bound states, 1 mM cAMP was added to the protein samples. Holoenzyme was formed according to the protocol for the holoenzyme sample of RIα (91-244) as described above.The holoenzyme sample was then concentrated to 0.2 mM in 50 mM Mops (pH 7), 100 mM NaCl, 10 mM $MgCl_2$, 5 mM DTT, 1 mM 5'-Adenylyl imidodiphosphate (AMP-PNP), 0.02% sodium azide, and 5% $^{2}H_2O$. TROSY 2D experiments with 80 (t1) and 1024 (t2) complex points and spectral widths of 31.82 and 15.94 ppm for the ^{15}N and ^{1}H dimensions, respectively, were recorded with 80 scans and a recycle delay of 1.70 s.

Spin labeling and Paramagnetic Relaxation Enhancement analysis: Ala109Cys PKA RIα (91-244) was prepared according to the protocol used for wt RIα (91-244), but during the purification of the mutant, DTT or β-mercaptoethanol was added to the buffer. The spin label 1-oxyl-2,2,5,5-tetra-methyl-pyrroline-3-methyl-16 methanethiosulfonate (MTSL) was covalently attached to the free cysteine residue in the mutant Ala109Cys PKA RIα (91-244). The reducing reagent was exchanged using a PD10 column before the addition of MTSL. The reduced mutated PKA RIα (91-244) was incubated with a 3-fold molar excess of MTSL for 3 hours at room temperature. After the excess MTSL was removed using a PD10 column, 2 mM Rp-cAMPS was added to 10 μM apo mutated PKA RIα (91-244). To prepare the cAMP-bound sample, 2 mM cAMP was added to 10 μM apo mutated PKA RIα (91-244). The PRE ^{1}H transverse relaxation rates were obtained from two time-points measurements (4) for both the cAMP- and the Rp-cAMPS-bound sample. The detection block for the PRE experiments was a sensitivity enhanced $^{1}H^{15}N$ HSQC with 256 (t1) and 1024 (t2) complex points and spectral widths of 31.82 ppm and 14.06 ppm for the ^{15}N and ^{1}H dimensions, respectively. 96 scans were recorded with a recycle delay of 1.50 s. The variation in the PRE relaxation delay (ΔT) was optimized to 5.9 ms. After recording the data for the paramagnetic state, 5 mM DTT was added to obtain the diamagnetic control for both the cAMP- and the Rp-cAMPS-bound samples. The diamagnetic sample was incubated at room temperature for 1 hour, after which we repeated the same experiments carried out for the paramagnetic sample. The HN Γ2 rates were then quantified as previously described (4).

Measurement of PKA Holoenzyme Activation by cAMP: The activity of recombinant purified C-subunit was determined by a luminescent kinase assay (Kinase-Glo; Promega) that

quantifies decrements in ATP due to kinase activation. The PKA holoenzyme was exposed (5 min, 20°C) to cAMP (0.1–10 μM), after which 5 μM Kemptide and 4 μM ATP were added and allowed to react for 60 min in 50 μL assay buffer (Tris-HCl 40 mM pH 7.5, BSA 0.1 mg/ml and $MgCl_2$ 20 mM). Reactions were stopped by adding 50 μL of the Ultra-Glo Luciferase reagent (Promega), which was incubated for an additional 10 min at room temperature. Luminescence was measured with a TECAN infinite M200 microplate luminometer.

Inhibition of PKA activity by RIα (91-244): The catalytic subunit (4 nM) was incubated with different concentrations of RIα (91-244) for 10 min at room temperature. A mixture of Kemptide 50 μM and 10 μM ATP were added to 50 μL assay buffer (Tris-HCl 40 mM pH 7.5, BSA 0.1 mg/ml and $MgCl_2$ 20 mM) to start the phosphorylation reaction. A mixture of the catalytic subunit (4 nM) and 10 μM ATP without Kemptide was prepared as a positive control sample in 50 μL assay buffer. After 60 min, the reaction was stopped by adding 50 μL of the Ultra-Glo Luciferase solution (Promega) to the reaction solution and incubating for 10 min. Luminescence was measured with a TECAN ULTRA Evolution spectrophotometer. Normalized Relative Luminescence Units (RLU) were calculated by subtracting the luminescence of the free catalytic subunit sample from that of all sample's and dividing by the luminescence of the positive control, which was also corrected by subtracting the luminescence of the free catalytic subunit.

2.9 Supplementary Information: SVD analysis of the chemical shift matrix

The SVD analysis indicates that the first two principal components (PCs) alone account for more than 90% of the total variance (Table S2) and Fig. S4c shows the PC1 *vs*. PC2 map of

the residue-specific scores (black circles) and of the perturbation-specific loadings (red diamonds). The loadings with the largest component along PC1 correspond to differences between active and inactive forms of R¬A, which are all ligand-bound (e.g. cAMP – Rp-cAMPS, Fig. S4c), indicating that PC1 reports primarily on allosteric activation as opposed to binding. Unlike PC1, the second PC reports mainly on binding rather than activation, since the loading with the largest component along PC2 corresponds to differences between the apo and the Rp-cAMPS-bound states (Fig. S4c), which are both inactive. The SVD scores for the residues in the largest AC cluster (Fig. 3b) are distributed mostly along PC1 (Fig. S4c, grey filled circles), confirming that the AC network, which includes the linker, is functionally linked to the cAMP-dependent allosteric activation of PKA.

2.10 Supplementary Information: Thermodynamic Modeling of the cAMP Dependent Activation of PKA

The first step in the thermodynamic model of the cAMP-dependent activation of PKA is to consider that in the absence of cAMP (apo form) the inhibiting R-subunit construct RIα (91-244) exists as an equilibrium between the inhibiting (inactive) conformation, denoted as H, and the active conformation, denoted as B. If L is defined as the equilibrium constant for the H *vs*. B equilibrium in the apo form:

$$L = [H]_{apo}/[B]_{apo} \qquad (S1)$$

then the $[H]_{total}/[B]_{total}$ ratio in the presence of cAMP defines an apparent equilibrium constant L_{app}. computed as:

$$L_{app.} = L (1 + K_{a,R(H):cAMP} [cAMP]) / (1 + K_{a,R(B):cAMP} [cAMP]) \quad (S2)$$

where [cAMP] is the concentration of free cAMP, while $K_{a,R(H):cAMP}$ and $K_{a,R(B):cAMP}$ are the association constants between cAMP and RIα (91-244) in the H and B conformations, respectively. The apparent equilibrium constant L_{app} is then used to compute the overall molar fractions of the H and B conformations, i.e. x_H and x_B, at any given concentration of cAMP as:

$$x_H = L_{app.} / (1 + L_{app.}) \quad (S3)$$

$$x_B = 1 - xH \quad (S4)$$

The molar fractions of the H and B conformations are in turn utilized for calculating the conformation-average association constant between RIα (91-244) and the catalytic subunit of PKA (i.e. C):

$$K_{a,R:C} = x_H K_{a,R(H):C} + x_B K_{a,R(B):C} \quad (S5)$$

where $K_{a,R(H):C}$ and $K_{a,R(B):C}$ are the association constants between C and RIα (91-244) in the H and B conformations, respectively. It should be noted that equations S1-S5 can also be derived by differentiating with respect to [C] the binding polynomial based on the thermodynamic linkage model of Fig. 4a: $Q = L(1+ K_{a,R(H):C} [C]) (1+ K_{a,R(H):cAMP} [cAMP]) + (1+ K_{a,R(B):C} [C]) (1+ K_{a,R(B):cAMP} [cAMP])$. In principle, $K_{a,R:C}$ computed according to equation (S5) should be downscaled to account for the competing effect of the Kemptide substrate binding to C. However, the downscaling factor caused by the competitive binding of Kemptide is (1 + [Kemptide]/$K_{d,Kemptide:C}$), which is negligible considering that $K_{d,Kemptide:C}$ is estimated at ~300 μM (5) and that under our experimental conditions [Kemptide] ≤ 5 μM. We therefore relied on

equation (S5) for the calculation of the $K_{a,R:C}$ association constant, which was then used to compute the average fraction of inhibited C, i.e. bound to RIα (91-244), or $<\nu>$ at any given concentration of cAMP as:

$$<\nu> = \{ \beta - \sqrt{(\beta^2 - 4[R]_{tot.}[C]_{tot.})} \} / (2[C]_{tot.}) \qquad (S6)$$

where $\beta = [R]_{tot.} + [C]_{tot.} + (1/K_{a,R:C})$ and $[R]_{tot.}$ and $[C]_{tot.}$ are the total concentrations of RIα (91-244) and C, respectively.

Equations (S1-S6) were used to compute $<\nu>$ at different concentrations of free cAMP. However, the concentrations of free cAMP are often not experimentally available and only the total concentrations of cAMP are measured. To circumvent this problem the concentration of free cAMP can be computed from the total concentration of cAMP through the following approximations. First, we consider that under the experimental conditions used for the measurement of the activation of PKA:

$$[R]_{tot.} > [C]_{tot.} >> K_{d,R:C} \qquad (S7)$$

The inequalities in (S7) imply that in the absence of cAMP essentially all C is bound to R and excess free R is present in the amount of:

$$[R]_{free} \approx [R]_{tot.} - [R:C] \qquad (S8)$$

with $[R:C] \approx [C]_{tot}$ at the beginning of the cAMP titration[1]. The excess free R acts as a high affinity sink for cAMP that depletes the cAMP pool available for targeting the R:C complex,

[1] The concentration of [R:C] for subsequent points in the cAMP titration is estimated based on the computation of $<\nu>$ for the preceding total cAMP concentration considered.

which exhibits a lower affinity for cAMP. However, the high affinity sink effect arising from the excess free R can be easily modeled once $[R]_{free}$ and $K_{a,R:cAMP}$ are known:

$$[cAMP]_{free} = [cAMP]_{tot} - 0.5\{ \gamma - \sqrt{(\gamma^2 - 4[R]_{free}[cAMP]_{tot.})} \} \quad \text{(S9)}$$

where $\gamma = [R]_{free} + [cAMP]_{tot.} + (1/K_{a,R:cAMP})$ and

$$K_{a,R:cAMP} = xH_{,apo}\, K_{a,R(H):cAMP} + x_{B,apo}\, K_{a,R(B):cAMP} \quad \text{(S10)}$$

Equations (S9) and (S10) allow the computation of $[cAMP]_{free}$ starting from $[cAMP]_{tot}$.

In conclusion, using equations (S1-S10) the fraction of C bound to R (i.e. $<\nu>$) is computed for each $[cAMP]_{tot}$ value considered. $[cAMP]_{tot}$ was varied between a minimum of 1 nM and a maximum of 1 mM and the resulting calculated $<\nu>$ *vs*. $[cAMP]_{tot}$ function was utilized to model the experimental RLU (Relative Luminescence Units) profile, assuming that the $<\nu>$ computed at the minimum and maximum $[cAMP]_{tot}$ correspond to the maximum and minimum measured RLU values, respectively. Overall the computation of $<\nu>$ *vs*. $[cAMP]_{tot}$ based on equations (S1-S10) relies on five key thermodynamic constants: $K_{a,R(H):cAMP}$ and $K_{a,R(B):cAMP}$, which together define the affinity and the H *vs*. B selectivity of cAMP for RIα (91-244), $K_{a,R(H):C}$ and $K_{a,R(B):C}$, which together define the affinity and the H *vs*. B selectivity of C for RIα (91-244), and L, which, although is an exquisite property of the apo form, is also a key determinant of the cAMP-dependent activation of PKA. Table S1 summarizes the values of these five key thermodynamic parameters that reproduce the experimental data of Fig. 4 and are consistent with the available dissociation constants independently measured by stopped flow kinetic measurements (6). It should be noted that, although this two-state mechanism is the simplest model we could propose to fit the experimental data of Fig. 4, we cannot rule out that more

complex models (with more than two states) may apply as well. For instance, it is possible the apo and C-bound H-states may differ, as C-binding might quench the dynamics at the R:C interface, including part of the cAMP phosphate binding cassette.

2.11 Supplementary References

1. Huang H, Melacini G (2006) High-resolution protein hydration NMR experiments: Probing how protein surfaces interact with water and other non-covalent ligands. Anal Chim Acta 564(1):1–9.
2. Leon DA, Canaves JM, Taylor SS (2000) Probing the multidomain structure of the type I regulatory subunit of cAMP-dependent protein kinase using mutational analysis: Role and environment of endogenous tryptophans. Biochemistry 39(19):5662–5671.
3. Slice LW, Taylor SS (1989) Expression of the catalytic subunit of cAMP-dependent protein kinase in Escherichia coli. J Biol Chem 264(35):20940–20946.
4. Iwahara J, Tang C, Marius Clore G (2007) Practical aspects of (1)H transverse paramagnetic relaxation enhancement measurements on macromolecules. J Magn Reson 184(2):185–195.
5. Masterson LR, Mascioni A, Traaseth NJ, Taylor SS, Veglia G (2008) Allosteric cooperativity in protein kinase A. Proc Natl Acad Sci USA 105(2):506–511.
6. Anand GS, et al. (2010) Cyclic AMP- and (Rp)-cAMPS-induced conformational changes in a complex of the catalytic and regulatory (RIα) subunits of cyclic AMP-dependent protein kinase. Mol Cell Proteomics 9(10):2225–2237.
7. Dao, K.K.,et al. (2006) Epac1 and cAMP-dependent protein kinase holoenzyme have similar cAMP affinity, but their cAMP domains have distinct structural features and cyclic nucleotide recognition. J. Biol. Chem. 281:21500–21511.

2.12 Supplementary Figures

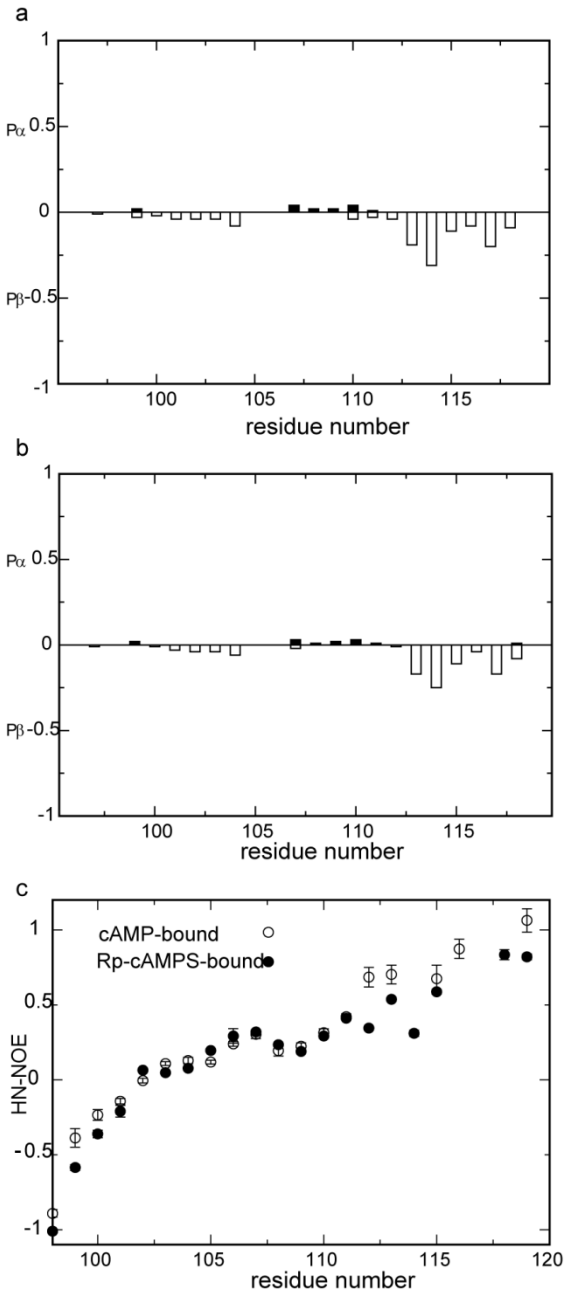

Figure S1: Lack of well-defined secondary structure in the linker as confirmed by the secondary structure probabilities of the RIα linker (97-120) computed based on the observed chemical shifts using the PECAN software (7) for (a) cAMP-bound and (b) Rp-cAMPS-bound RIα. The α-helix and β-strand probabilities are reported as positive and negative values, respectively. The RIα (96-244) construct was used because of its solubility at the concentrations required for the acquisition of triple resonance experiments. (c) The linker appears quite flexible in the ps-ns time-scale, as indicated by the HN-NOEs measured for the RIα linker (97-120) residues in cAMP-bound (open circles) and Rp-cAMPS-bound (filled circles) RIα (96-244). This construct was used because of its solubility at the concentrations required for the measurement of reliable HN-NOE values.

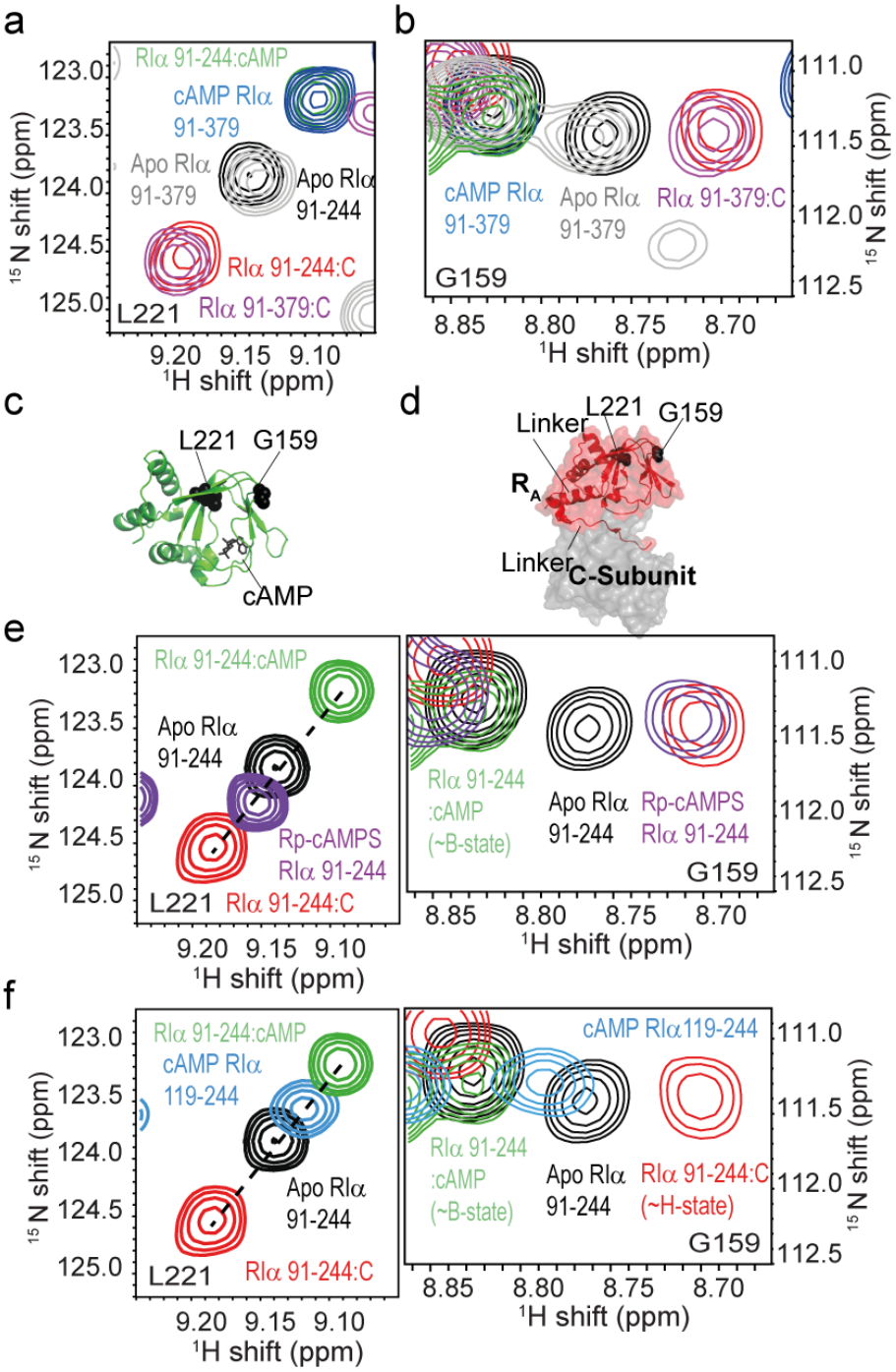

Figure S2: Position of the H vs. B equilibrium of CBD-A in apo, cAMP- and C-bound RIα (91-244) and RIα 91-379 as sensed by the HSQC peak of L221 (a) and G159 (b). Whenever R is bound to C, TROSY spectra were acquired. Location of L221, G159 relative to the C-subunit (c) and cAMP (d) binding interfaces in H and B conformation. Representative H-N correlation peaks for Rp-cAMPS bound RIα (91-244) (purple) (e) or cAMP bound RI α (119-244) (cyan) (F).

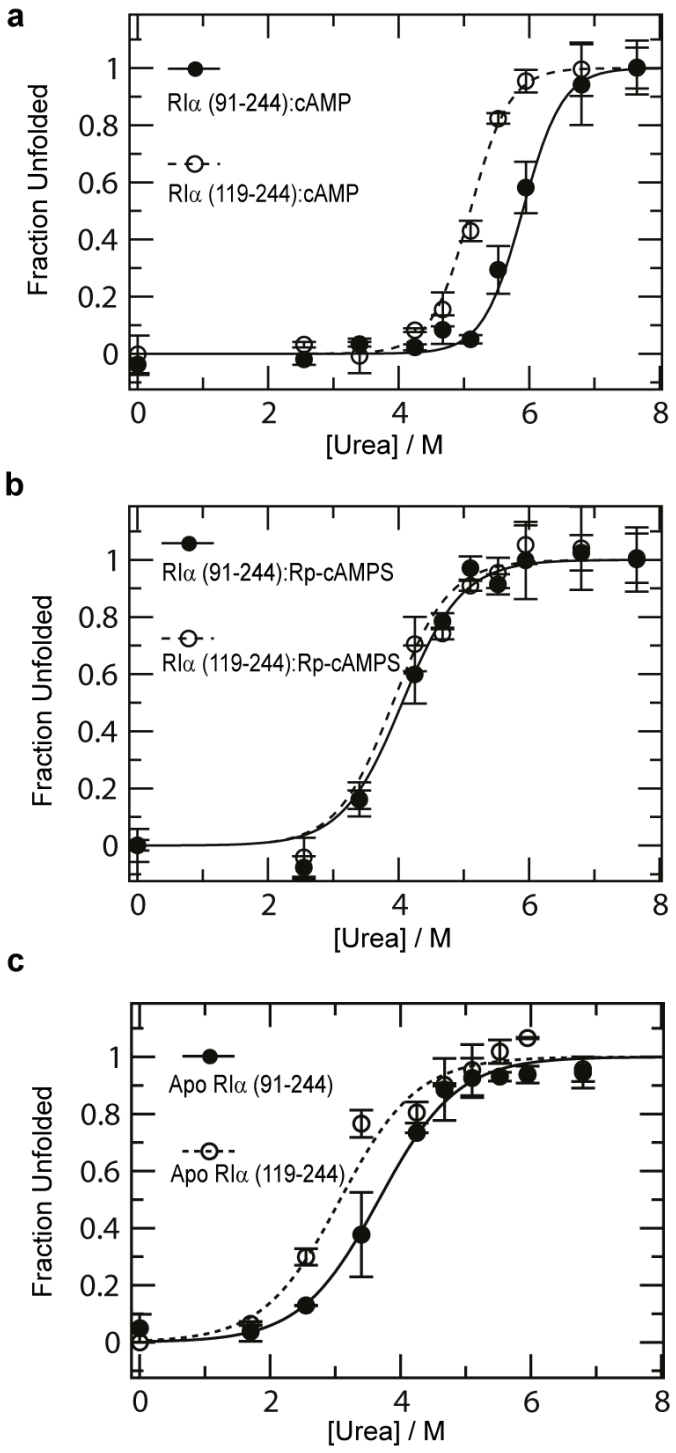

Figure S3: Effect of the RIα (91-118) linker deletion on the urea-induced unfolding of CBD-A bound to either cAMP (A) or the reverse-agonist Rp-cAMPS (B) or in the apo state (C). Symbol legends are embedded in the figure. Fluorescence data report primarily on the unfolding of the globular CBD-A. Boundaries of CBDA are defined by its non-contiguous α-subdomain with three N-terminal helices starting from residue 119 and a C-terminal helix ending at residue 244 (Fig. 1C), as shown through local spatial pattern alignment methods

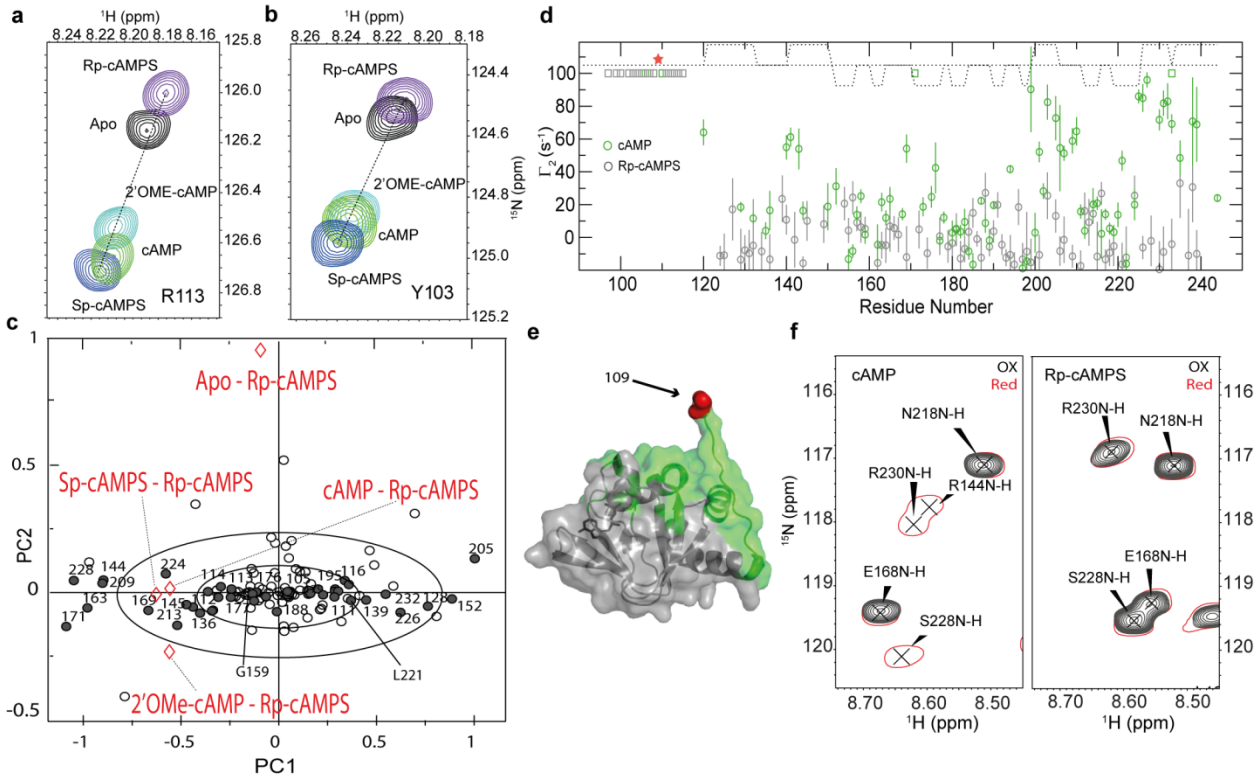

Figure S4: CHEmical Shift Covariance Analysis (CHESCA) and the comparison of PRE profiles observed for cAMP- and Rp-cAMPS-bound RIα (91-244). (a, b) Representative cross-peaks from the HSQC spectra used for CHESCA: Apo, cAMP, 2'-OMe-cAMP, Sp-cAMPS and Rp-cAMPS-bound RIα (91-244). (c) SVD of the chemical shift matrix referenced to the Rp-cAMPS-bound state (9). Since the first two principal components (PCs) alone account for more than 90% of the total variance (Table S2), the PC1 vs. PC2 map of the residue-specific scores (black circles) and of the perturbation-specific loadings (red diamonds) is shown. Ellipsoids at one and two standard deviations for the first two principal components are displayed with solid black lines. PC1 reports primarily on allosteric activation as opposed to binding. Unlike PC1, the second PC reports mainly on binding rather than activation. The scores for the residues in the largest AC cluster (Fig. 3b) are distributed mostly along PC1 (grey filled circles), confirming that this network is functionally linked to the cAMP-dependent allosteric activation of PKA. (d) HN Γ2 rates quantified for a sample with a nitroxide at the 109 position (indicated by a red star). Green circles refer to the cAMP-bound state, whereas black circles are for the Rp-cAMPS-bound state. Squares indicate disappearance of peaks in the oxidized state, which is observed in the linker region (97-118). Overall, the PREs observed in the presence of cAMP are markedly higher than those detected with the Rp-cAMPS reverse-agonist, as expected based on the B vs. H preferential interactions of the linker. (e) Map of the residues for which the Γ2 rates in the B state exceed the average + one standard deviation (green surface and ribbon representation; PDB accession code 1NE6). The locations of the PRE spin-label (Ala109Cys) is indicated in red. The CBD-A residues experiencing the most significant PREs are those on the side of the CBD-A proximal to the linker in the cAMP-bound state. (f) Representative $^{1}H^{15}N$ HSQC expansions. The spectra recorded with nitroxide in the oxidized (black) and reduced states (red) are shown for both the cAMP- and Rp-cAMPS-bound forms.

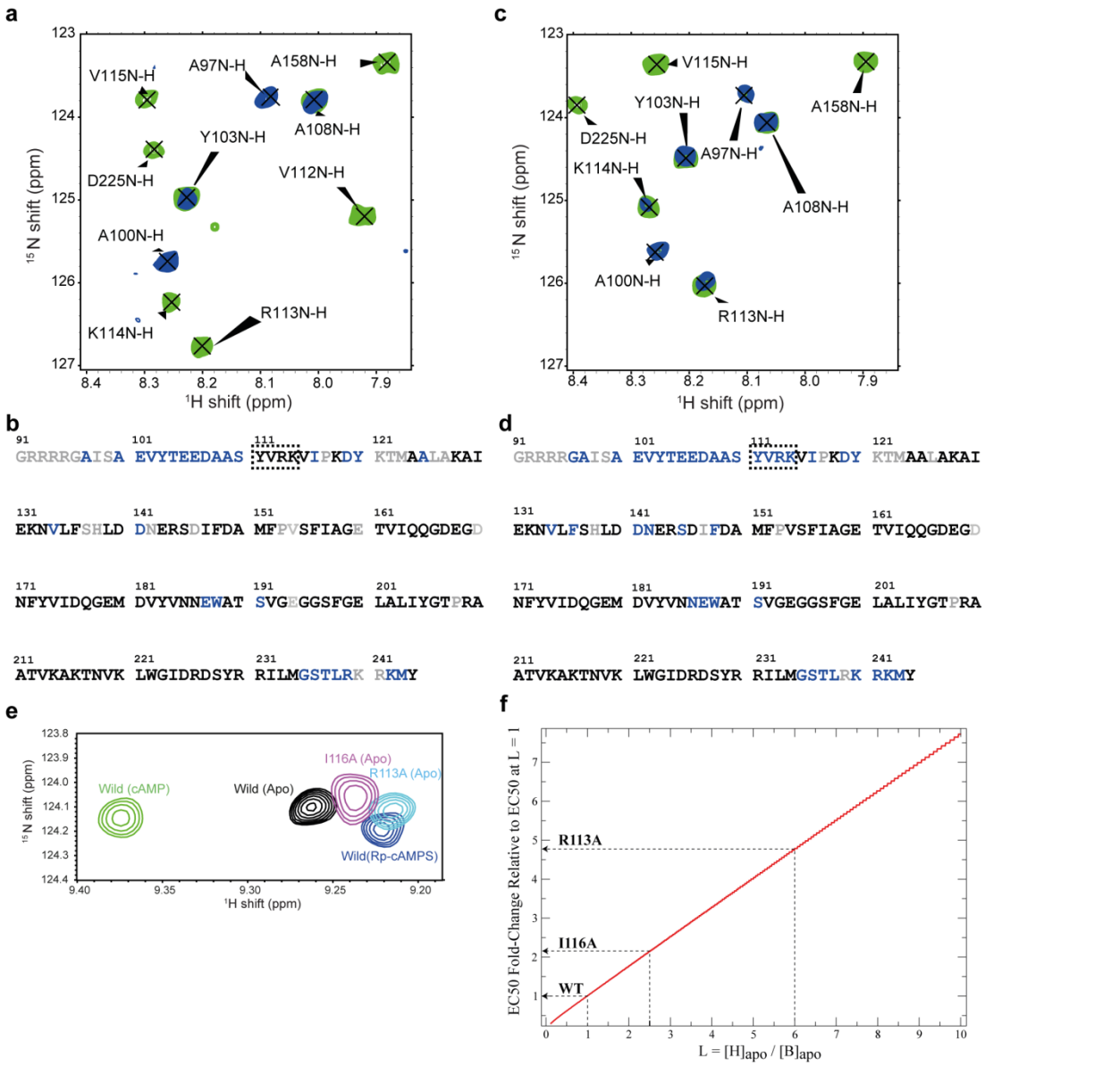

Figure S5: H/H exchange data for RIα (91-244) bound to either cAMP (a, b) or Rp-cAMPS (c, d) The H/H exchange spectra were acquired for both the cAMP- and the Rp-cAMPS-bound forms of RA, because these ligands stabilize the B and H states of CBD-A, respectively. (a, c) Representative HSQC (green) and CLEANEX (blue) cross-peaks. (b, d) RIα (91-244) sequence with residues for which CLEANEX cross-peaks were observed marked in blue. Assigned residues for which CLEANEX cross-peaks were not observed are marked in black. Not assigned and/or overlapped residues are shown in grey. The comparative cAMP vs. Rp-cAMPS H/H analysis reveals that residues 111-114 (dotted box) are more exposed in the Rp-cAMPS-bound form than in the presence of cAMP, confirming that R113 and the adjacent residues define a key site for the B-selective interaction of the linker with CBD-A. (e) Effect of the R113A and I116A mutations on the H vs. B equilibrium of apo RIα (91-244) as sensed by the HSQC peak of D140. The R113A and I116A mutations shift the H vs. B equilibrium of apo RIα (91-244) away from the B state, represented by the cAMP-bound WT RIα (91-244) peak. (f) EC50 dependence on L, the H vs. B equilibrium constant for apo RA, predicted by the thermodynamic model of Fig. 4a. Only the L parameter was varied, with the other four equilibrium constants kept fixed at the values reported in Table S1.

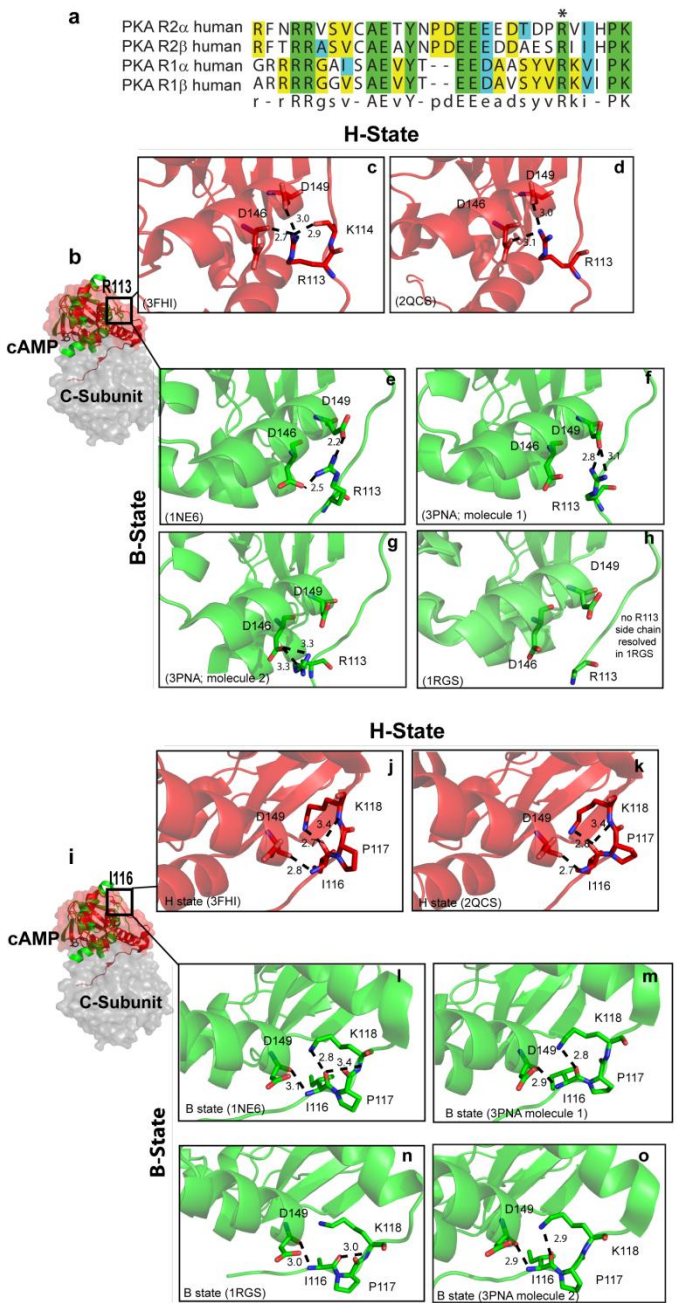

Figure S6: (a) Sequence alignment with CLUSTALW, among the four isoforms of the human R-subunit for the region corresponding to the (91-118) linker of RIα. The position of R113 in RIα is marked by an asterisk. (b) Location of R113 relative to the cAMP and C-binding interfaces. (c, d) Hydrogen-bonds (dashed lines) formed by the R113 guanidinium in the H-state crystal structures, i.e. C-bound RIα subunit. Note that all residue numbers refer to the R-subunit. (e-h) As (c, d) but for the B-state, i.e. cAMP- or Sp-cAMPS-bound RIα subunit. Distances are reported in Å. The PDB codes are indicated in parenthesis in the figure. The R113 side chain is missing in the 1RGS structure. (i) Location of I116 relative to the cAMP and C-binding interfaces. (j, k) Hydrogen-bonds (dashed lines) formed by I116 in the H-state crystal structures, i.e. C-bound RIα subunit. All residue numbers refer to the R-subunit. (l-o) As (j, k) but for the B-state, i.e. cAMP- or Sp-cAMPS-bound RIα subunit. Distances are reported in Å. The PDB codes are indicated in parenthesis in the figure.

2.13 Supplementary Tables

Table S1 : Summary of Urea-Induced Unfolding Thermodynamics Data for the (91-244) and (119-244) RIα constructs

RIα Construct	Bound to	C_m / M	$\Delta_{UF}G^{o}_{H2O}$ / (kcal/mol) [a]	$\Delta_{\Lambda}\Delta_{UF}G^{o}_{H2O}$ / (kcal/mol) [b]	m / (kcal/mol M)
(91-244)	cAMP	5.9 ± 0.2	11.4 ± 0.2		-1.9 ± 0.1
(119-244)	cAMP	5.1 ± 0.1	9.9 ± 0.2	1.5 ± 0.3	-1.9 ± 0.1
(91-244)	-- *Apo*	3.7 ± 0.2	3.6 ± 0.1		-1.0 ± 0.1
(119-244)	-- *Apo*	3.1 ± 0.2	3.0 ± 0.1	0.6 ± 0.2	-1.0 ± 0.1
(91-244)	Rp-cAMPS	4.0 ± 0.2	5.3 ± 0.2		-1.4 ± 0.1
(119-244)	Rp-cAMPS	4.0 ± 0.1	5.2 ± 0.2	0.1 ± 0.3	-1.3 ± 0.1

[a]Free energy of unfolding extrapolated to 0 M urea concentration. [b]Difference between the $\Delta_{UF}G^{o}_{H2O}$ free energies measured with and without the (91-118) linker. $\Delta_{\Lambda}\Delta_{UF}G^{o}_{H2O}$ quantifies the overall strength of the interactions between the (91-118) linker and the cAMP-binding domain A (CBD-A) of RIα.

Table S2: Principal Component Breakdown of Total Variance

Principal Component (PC)	Percentage of Total Variance
PC1	80.1 % (80.1 %)*
PC2	11.4 % (91.5 %)*
PC3	7.1 % (98.6 %)*
PC4	1.4 % (100 %)*

*The percentage reported in parenthesis reflects the cumulative contributions of the PCs in a given row and above.

Table S3: Thermodynamic Constants Used for the Modeling of PKA Activation [a]

	$K_{a,R(H):C}$ / M^{-1}	$K_{a,R(B):C}$ / M^{-1}	$K_{a,R(H):cAMP}$ / M^{-1}	$K_{a,R(B):cAMP}$ / M^{-1}	L
Wt	$2.5x10^{10}$ [b]	$3.1x10^{7}$ [c]	$\leq 10^{4}$ [d]	$0.5x10^{9}$ [e]	1.0 [f]
I116A	$2.5x10^{10}$ [b, g]	$3.1x10^{7}$ [c, g]	$\leq 10^{4}$ [d, g]	$0.5x10^{9}$ [e, g]	2.5 [e]
R113A	$2.5x10^{10}$ [b, g]	$3.1x10^{7}$ [c, g]	$\leq 10^{4}$ [d, g]	$0.5x10^{9}$ [e, g]	6.0 [e]

[a] These constants are defined as follows: $K_{a,R(H):C}$ and $K_{a,R(B):C}$ are the association constants between C and RIα (91-244) in the H and B conformations, respectively, while $K_{a,R(H):cAMP}$ and $K_{a,R(B):cAMP}$ are the association constants between cAMP and RIα (91-244) in the H and B conformations, respectively. L is the H *vs.* B equilibrium constant of RIα (91-244) in the absence of cAMP (*i.e. apo* form), as defined in equation (S1).

[b] $K_{a,R(H):C}$ is approximated as the association constant between C and the reverse agonist Rp-cAMPS-bound RIα (91-244) previously measured by stopped flow kinetic measurements (1). From SI reference (1)

[c] $K_{a,R(B):C}$ is approximated as the association constant between C and cAMP-bound RIα (91-244) previously measured by stopped flow kinetic measurements (6).From SI reference (6).

[d] This estimate is based on reference (7) indicating that cAMP binds the R:C complex with a $K_d > 1$ μM and on the fitting of the activation data for the R113A and I116A mutants. From SI reference (7)

[e] Obtained by fitting to the measured activation profile of Fig. 4.

[f] L was independently measured using the NMR chemical shifts of Fig. 2.

[g] These association constants were assumed to be unaffected by the mutation as the mutated residue is well outside both interfaces with C and cAMP (Fig. S6b, i)

Chapter 3

Inter-CBD Linker Control by the PKA RIα CBD-B

3.1 Author's Preface

The work presented in this chapter was submitted to Plos Biology. I conducted most of the experiments necessary for the manuscript. Eric Tyler McNicholl performed the assignment of 119-379 PKA R subunit constructs. Avinash Ramkissoon and Kody Moleschi supported the purification of the catalytic subunit of PKA. S.S.Taylor provided the plasmids. I co-wrote the manuscript with Dr. Giuseppe Melacini.

3.2 Introduction

cAMP is an ancient second messenger and in higher eukaryotes Protein Kinase A (PKA) is the major receptor for cAMP. The cAMP-dependent activation of PKA controls the intra-cellular responses to a wide variety of extracellular stimuli [1-4]. In the resting state, PKA exists as an inhibited tetramer formed by a dimeric regulatory subunit (R_2), with each R-protomer binding and inhibiting one equivalent of catalytic subunit (C). Upon binding of four equivalents of cAMP to R_2, the R_2C_2 tetramer dissociates releasing active C-subunit to phosphorylate downstream substrates [5,6]. The R-subunit of PKA is a multi-domain protein (Figure 1a), starting from a dimerization-docking domain followed by a linker, which includes an inhibitory site for C and is in turn followed by two tandem cAMP-binding domains (CBD-A and B) that provide additional contact sites for binding the C-subunit [7,8]. The RIα (91-379) construct spans the inhibitory site and both CBDs (Figure 1a) and recapitulates both C-inhibition and cAMP-dependent activation of PKA [9-11]. The structures of this construct have been solved in both the $cAMP_2$-bound (i.e. active) [10] and C-bound forms (i.e. inactive) [9], revealing major conformational changes that underlie the cAMP-dependent activation of PKA (Figure 1c). Furthermore, the dynamics of apo CBD-A has been recently shown to be another central determinant of the allosteric control of PKA activation by cAMP [12]. However, less is known about the CBD-B dynamics and how it relates to the physiological function of this domain.

The CBD-B serves a pivotal function in both PKA inhibition and activation. The structure of C-bound RIα (91-379) has revealed that CBD-B contributes to the effective inhibition of the C-subunit because the N-terminal helix of CBD-B provides a key site for binding C [9]. The structure of $cAMP_2$-bound RIα (91-379) has shown that CBD-B also facilitates the

cAMP-dependent release of C from R by functioning as a "gate-keeper" domain that controls the availability of a Trp indole (i.e. W260) that stacks against the adenine of cAMP bound to CBD-A and acts as a lid for CBD-A [10,11,13]. However, as in the case of CBD-A [12], the cAMP- and C-bound structures of CBD-B are not sufficient for a full thermodynamic dissection of the central function of CBD-B, which requires also the investigation of apo CBD-B.

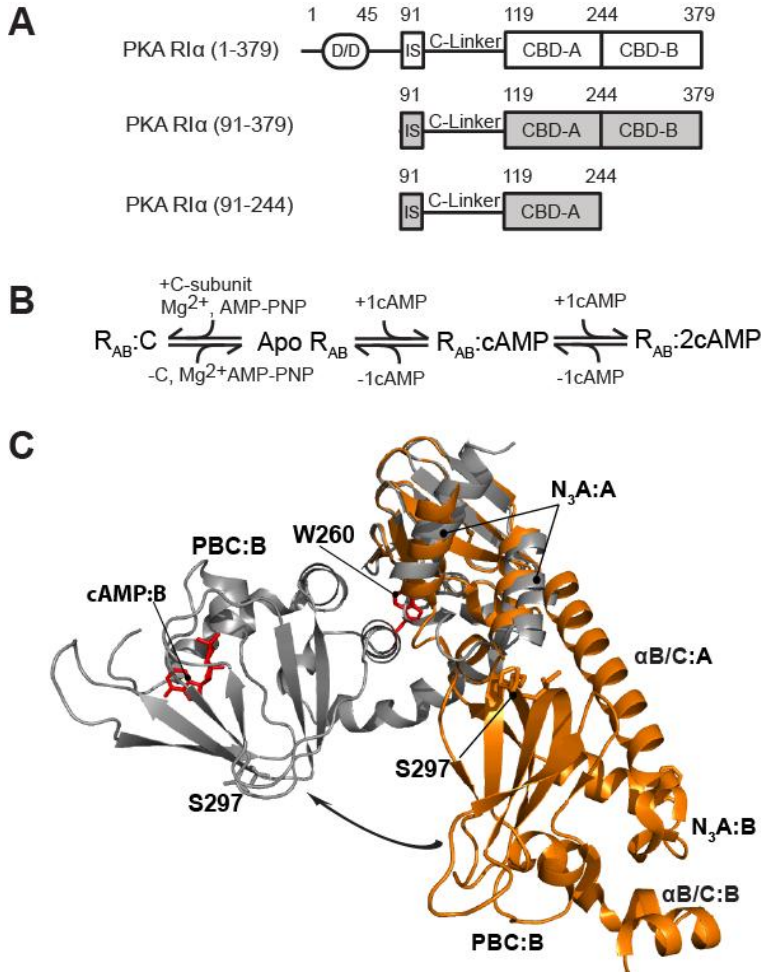

Figure 1: Construct design and architecture of PKA RIα. (A) Domain organization of the RIα subunit of PKA and its minimal functional constructs to ensure cAMP-dependent inhibition of the catalytic subunit (C). (B) Binding equilibria of PKA RIα. Even when apo RIα is a transient low-population intermediate, it is still a critical thermodynamic determinant of cAMP-dependent regulation of PKA. (C) Structures of PKA RIα (91-379) bound to either cAMP (grey, PDB code 1RGS) or the C-subunit (orange, PDB code 2QCS). The two structures are superimposed through the β-barrel of cAMP-binding domain (CBD) A. Selected regions and residues are labeled. The arrow shows the change of the position of CBD-B relative to CBD-A occurring upon cAMP-binding.

The currently available evidence suggests that apo CBD-B is highly dynamic. The structure of RIα (91-379) with cGMP bound to site A and no nucleotide bound to site B revealed overall elevated B-factors for CBD-B relative to CBD-A [14] and a SAXS investigation of the R:C complex indicated that the orientation of CBD-B relative to CBD-A and the C-subunit is dynamic [15, 16]. In addition, MD simulations confirmed that the helix connecting CBD-A and B is flexible in the absence of cAMP [17]. Overall, these initial results suggest that dynamics of nucleotide-free CBD-B is functionally critical, although currently the relationship between apo CBD-B dynamics and its function is not fully understood. Here we hypothesize that, similarly to CBD-A [12], apo CBD-B pre-samples both active and inactive conformations with cAMP or C selecting the former or the latter, respectively.

In order to test this hypothesis about conformational selection in CBD-B and to understand how the intra-CBD dynamics affects inter-CBD interactions, here we comparatively analyze by NMR the two domain construct RIα (91-379) in its apo, $cAMP_2$ and C-bound forms. The latter is the most technically challenging form of RIα (91-379) both in terms of sample preparation and NMR data acquisition, given the high MW (i.e. ~73 kDa), and was lacking in previous NMR investigations [18, 19]. However, C-bound RIα (91-379) is included here because it plays a critical role in our comparative NMR analysis scheme as an essential reference term for the inactive state of R. In addition, the present comparative analysis includes mutations designed to specifically probe inter-domain interactions and provides an opportunity to re-assess previous data on CBD-A [20, 12] in the context of a more complete construct with both tandem CBD-A and B.

Our comparative NMR analysis supports a model of double conformational selection in which each apo CBD populates a nearly degenerate free energy landscape independently of the adjacent CBD. Such degeneracy is unusual for allosteric systems, which typically sample highly skewed conformational equilibria in their apo form [21-23], but it explains why even weak interactions with the C-subunit are sufficient for conformational selection as well as why both RIα CBDs bind cAMP with higher affinity than other eukaryotic CBDs. Binding of two equivalents of cAMP eliminates this degeneracy by selecting the active conformation within each CBD and stabilizing the inter-CBD contacts. We also show that the CBD-A/B interface requires both cAMP and the indole of W260 to form, and, although it is not required for the intra-domain conformational selection, it contributes to the activation of PKA by occluding C-subunit recognition sites within CBD-A. Hence, the proposed model explains how CBD-B contributes to PKA inhibition and activation. In addition, our investigation revealed that cAMP-binding does not fully quench the dynamics of the apo CBDs, with major loci of residual dynamics found both at the inter-CBD interface and within each tandem CBD. Surprisingly, the residual dynamics profiles of the structurally homologous CBD-A and B are different. This unexpected finding supports the notion that conservation of structure does not necessarily imply conservation of dynamics and opens new opportunities in the selective targeting of CBDs for therapeutic purposes.

3.3 Material and Methods

Protein Expression and Purification: All PKA RIα constructs as well as the PKA C-subunit were expressed and purified according to previously published protocols [12, 18]. The W260A mutants were prepared by site-directed mutagenesis.

General NMR Spectroscopy: All NMR spectra were recorded at 306K, unless otherwise specified, using a Bruker AV 700 spectrometer equipped with a TCI cryo-probe and processed with NMRpipe [24] employing linear prediction, unless otherwise specified, and a resolution enhancing 60° shifted sine squared bell window function. All spectra were analyzed with Sparky [25] using Gaussian line-fitting. Assignments were obtained either through triple-resonance 3D experiments (i.e. HNCO, HNCA, HN(CO)CA, CBCA(CO)NH and HNCACB in TROSY-version for higher MW constructs) [26,27] and/or through spectral comparisons, if no ambiguities were present. The secondary structure probabilities were determined using the secondary chemical shifts via the PECAN software [28]. Other NMR experiments are discussed below.

Chemical Shift Analysis: Uniformly ^{2}H ^{15}N-labeled PKA RIα (91-379) and (91-244) were concentrated to 100 µM into the NMR buffer (50 mM MOPS (pH 7), 100 mM NaCl, 10 mM $MgCl_2$, 5 mM DTT, with or without 1 mM cAMP, 0.02 % sodium azide and 5 % $2H_2O$). The C subunit-bound RIα (91-379) and (91-244) were prepared with 1mM AMP-PNP in the NMR buffer as previously described [12]. Transverse-relaxation optimized spectroscopy (TROSY) 2D experiments with 80 (t1) and 1024 (t2) complex points and spectral widths of 31.82 ppm and 15.94 ppm for the ^{15}N and ^{1}H dimensions, respectively, were recorded with 12 scans and a recycle delay of 1.70 s. Sensitivity enhanced ^{15}N-^{1}H hetero-nuclear single quantum coherence (HSQC) spectra with 128 (t1) and 1024 (t2) complex points and spectral widths of 31.82 ppm

and 15.94 ppm for the ^{15}N and ^{1}H dimensions, respectively, were recorded with 8 scans and a recycle delay of 1.0 s. The ^{1}H and ^{15}N carrier frequencies were set at the water resonance and at the centre of the amide region, respectively. The C subunit and cAMP-bound RIα(91-379) forms served as the reference states in the CHEmical Shift Projection Analysis (CHESPA) to evaluate the position of the inhibitory equilibria in the apo RIα(91-379). The fractional activation and cos(θ) values were calculated as previously described [21].

Relaxation Measurements: Uniformly ^{15}N-labeled PKA RIα (119-379) wild type and W260A mutant were concentrated to 100 µM in 50 mM MES (pH 6.5), 100 mM NaCl, 5 mM DTT, 2 mM EDTA, 2 mM EGTA, 0.02 % sodium azide and 5 % $2H_2O$. The R1 relaxation rates were measured with water flipback and sensitivity enhanced pulse sequences using relaxation delays of 100 (×2), 200, 300, 400(×2), 500, 600, 800, and 1000 ms [22]. The R2 measurements were acquired using CPMG relaxation delays of 8.48, 16.96, 25.44, 33.92, 42.4, 50.88, 59.36, 76.32, and 93.28 ms with an offset and duty cycle compensated ^{15}N R2 CPMG pulse sequence with an inter-180^{o} pulse delay of 0.9 ms [22]. Both R1 and R2 experiments were acquired with recycle delays of 1.5 sec. The entire series of R1 and R2 relaxation rates were collected in triplicate and the NOE spectra were collected as a set of ten replicas. The acquired spectra were then co-added in the time domain prior to Fourier transformation. The R1 and R2 relaxation rates were determined by using cross peak fit heights in Sparky. The errors on the R1 and R2 rates were estimated from the Gaussian distributed random noise. The errors on the NOE values were gauged based on the standard deviation between fit heights in the replicate spectra. The ^{15}N relaxation data were mapped into reduced spectral densities as previously described [29]. The reduced spectral density values in the absence of internal motions were computed through

hydrodynamic simulation using the Hydro NMR software [30,31] and the $cAMP_2$- and C-bound structures (PDB Codes: 1RGS and 2QCS, respectively, but without C-subunit for comparison with the values from 1RGS). An atomic element radius of 2.8 Å was used in all hydrodynamic simulations.

H/D Exchange: Amide proton H/D exchange spectra were acquired as previously described [18] using the RIα (119-379) construct for the wild type and the mutant. The protein was concentrated to 100 μM in 50 mM MES (pH 6.5), 100 mM NaCl, 5 mM DTT, 2 mM EDTA, 2 mM EGTA, 0.02 % sodium azide and 5 % ^2H_2O. The cAMP bound sample was prepared by adding excess 100 μM cAMP in the buffer.

3.4 Results

3.4.1 Intra-Domain Conformational Selection in PKA RIα CBDs.

As a first step towards mapping the functional conformational equilibria of apo PKA RIα (91-379), we compared it to two reference states, i.e. C-bound RIα (91-379), which is assumed to trap the inhibitory ("inactive") conformation of RIα (91-379), and $cAMP_2$-bound RIα (91-379), which is expected to represent the uninhibited ("active") form of PKA-R. The comparative spectral analysis of apo *vs*. C- *vs*. $cAMP_2$-bound RIα (91-379) is illustrated in Figure 2. Panels 2a,b focus on two representative residues of CBD-A and B, i.e. G223 and S297, respectively, which are sufficiently removed from the cAMP and C-subunit binding interfaces to report primarily on the conformational equilibria of RIα (91-379). For both residues the cross-peaks arising from the apo, C and $cAMP_2$-bound forms define a clear linear pattern, which

is indicative of apo RIα (91-379) sampling two states (i.e. the active and inactive conformations) through an exchange that is fast in the chemical shift NMR time scale at the field of data acquisition (i.e. 700 MHz).

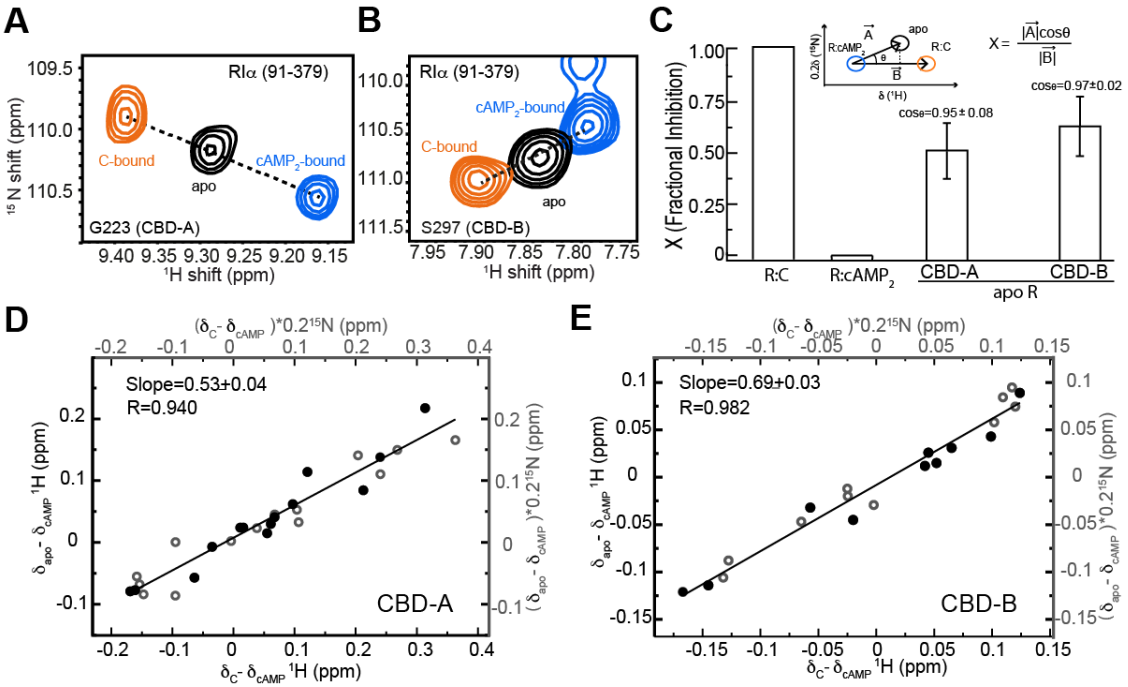

Figure 2: Conformational selection in CBD-A and B of RIα (91-379). (A, B) Overlay of apo, cAMP2-bound and C-bound RIα (91-379) for cross-peaks of representative residues sensing the active vs. inactive equilibria in CBD-A (A) and CBD-B (B). (C) Fractional inhibition of apo RIα (91-379) (X) relative to cAMP2- and C-bound RIα (91-379), assuming they represent the active and inactive forms of PKA, respectively. The inset illustrates how X was measured, using the CHEmical Shift Projection Analysis (CHESPA) method. The bar graphs shows the average X values observed for residues in CBD-A and B exhibiting a linear pattern ($|\cos\theta| > 0.95$). (D) Alternative evaluation of the fractional inhibition of apo RIα (91-379) (X) through the slope of the ($\delta_{apo} - \delta_{cAMP}$) vs. ($\delta_{apo} - \delta_{C}$) plot, where δ_{apo}, δ_{cAMP} and δ_{C} are the chemical shifts of apo, cAMP2- and C-bound RIα (91-379). Closed and open circles indicate ^{1}H and ^{15}N chemical shifts, respectively. This plot was restricted to CBD-A residues that are sufficiently removed from the cAMP-dependent interfaces (e.g. R:C, R:cAMP and CBD-A:CBD-B) to report primarily on the active vs. inactive equilibrium of CBD-A. (E) Similar to panel (D) but for CBD-B.

Given the fast regime for the active *vs*. inactive exchange, the apo cross-peak position is simply a population-weighed linear average of the chemical shifts for the active and inactive conformations. Hence, the chemical shifts encode directly the relative populations of the active

vs. inactive equilibrium. For example, the intermediate position of the apo peaks of G223 and S297 relative to those of the C and $cAMP_2$-bound forms (Figure 2a,b) suggests that in each apo CBD the populations of active and inactive states are comparable. In order to verify that this result does not depend on the specific choice of reporter residues (e.g. G223 and S297), the apo CBD active *vs*. inactive populations were also assessed through the CHEmical Shift Projection Analysis (CHESPA) (Figure 2c) [21] and through complementary chemical shift correlations (Figure 2d,e). Both approaches rely on a wider collection of conformational equilibria-sensing residues as opposed to only one residue per CBD, as shown in Figure 2a,b.

The CHESPA analysis (Figure 2c) shows that, if C- and $cAMP_2$-bound RIα (91-379) represent the inactive and active states of PKA, the average fractional activation observed for CBD-A is ~50%, with slightly higher values measured for CBD-B. The differences in average fractional activations between CBD-A and B are not major as they are within one standard deviation of both distributions (Figure 2c). Similar conclusions are obtained through chemical shift correlation analyses (Figure 2d,e). Panels 2d,e report the ($\delta_{Apo} - \delta_{cAMP}$) *vs*. ($\delta_C - \delta_{cAMP}$) chemical shift correlations for apo CBD-A and B, respectively. The linearity of the correlations in Figure 2d,e confirms that each CBD samples a dynamic two-state equilibrium of active and inactive conformations. In addition, the slopes of the correlations provide the molar fraction of inactive state, i.e. ~50% and ~70% for CBD-A and B, respectively, corroborating that both apo CBD-A and B access significant populations of active conformations, although the latter appears slightly lower for CBD-B than CBD-A. However, the somewhat higher population of inactive state in apo CBD-B *vs*. apo CBD-A may also reflect the fact in the R:C complex the CBD-B does not interact with the C-subunit as tightly as CBD-A. The transient nature of the CBD-B

interactions with the C-subunit may shift the R:C cross-peaks of CBD-B towards the apo cross-peaks, resulting in an increase in the apparent fractional inactivation measured for apo CBD-B. In this respect, the actual population of inactive state in apo CBD-B is possibly lower than the measured 70%, confirming that the CBD-B samples significant (i.e. > 30%) populations of active state even prior to cAMP binding.

It should be noted that even if we knew the exact value for fractional inactivation of CBD-B, the data in Figure 2 alone would not be sufficient to gauge the degree of correlation between the active – inactive conformational transitions in the two tandem domains. For example, if the actual fractional inactivation of each CBD is 50%, two markedly different distributions of state populations are still possible, i.e. one with 50% of active-active state, 50% of inactive-inactive state and no mixed (inactive-active and active-inactive) sates, while the other with 25% of each possible state. In the two scenarios the degree of correlation between the active-inactive transitions in the two domains is clearly different, but in both cases the fractional inactivation for each CBD is 50%. Hence, it is clear that understanding how the inactive *vs*. active intra-CBD equilibria are coupled to each other requires an assessment of CBD-A/B interactions in the context of a combinatorial analysis of CBD states (i.e. active-active, inactive-active, active-inactive and inactive-inactive CBD-CBD states). For this purpose, we dissected the state-specificity of inter-domain interactions by probing the effect of CBD-B deletion on CBD-A, i.e. by comparing the RIα (91-379) *vs*. RIα (91-244) constructs (Figure 3).

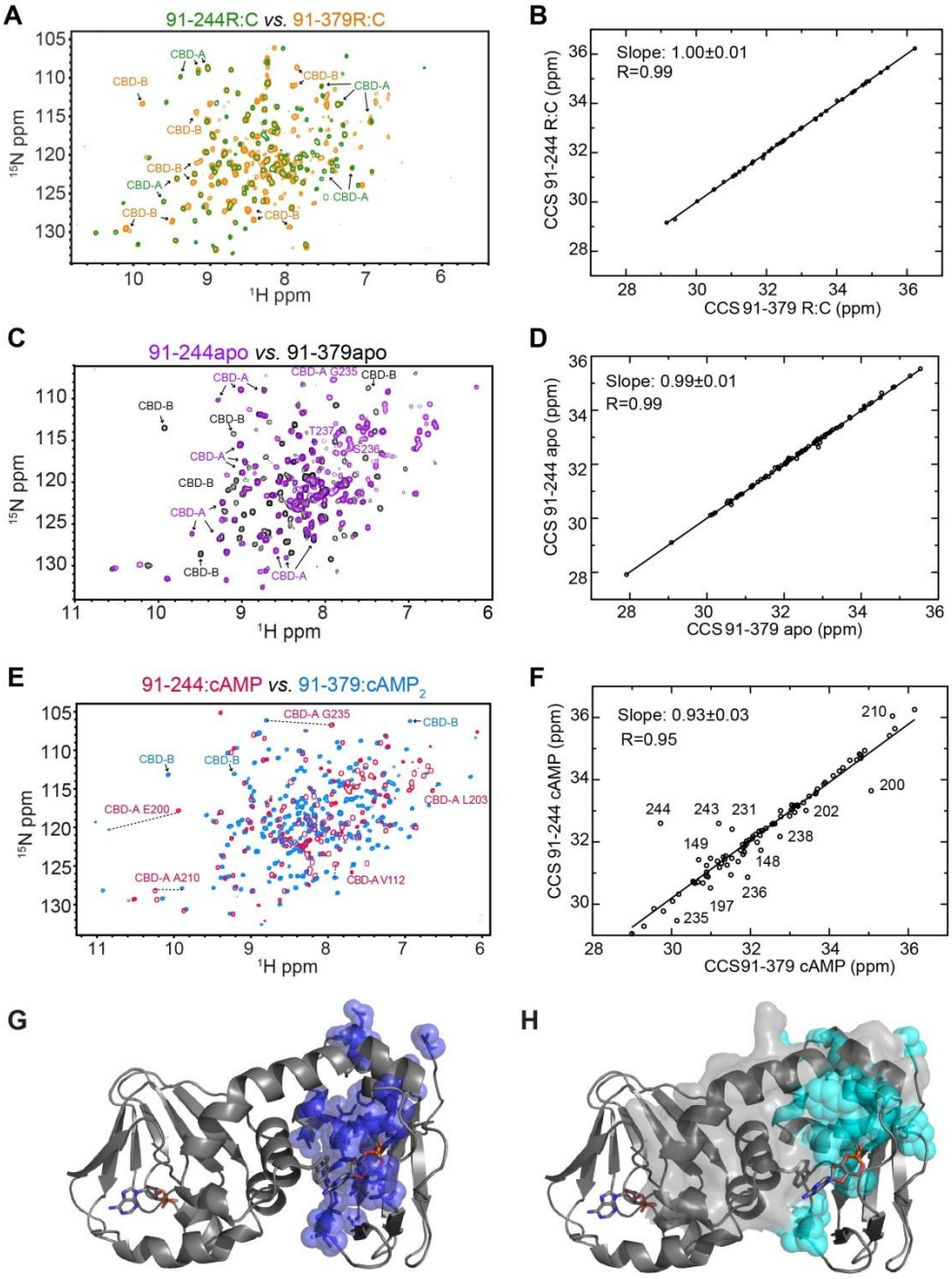

Figure 3: Probing CBD-A/B interactions in apo, C-bound and cAMP2-bound RIα (91-379) through CBD-B deletion. (A) Overlay of the HN-TROSY spectra of C-bound RIα (91-379) and RIα (91-244), in which CBD-B is deleted. (B) Correlation between the combined chemical shifts (CCS) of C-bound RIα (91-379) and RIα (91-244). (C, D) As panels (A, B) but for the apo form of RIα (91-379) and RIα (91-244). (E, F) As panels (A, B) but for the cAMP2-bound form of RIα (91-379) and the cAMP-bound form RIα (91-244). Color codes for panels A, C and E are indicated in the figure and representative CBD-A and B cross-peaks are labeled. (G) Map of above-average RIα (91-379):cAMP2 vs. RIα (91-244):cAMP CCS differences for residues < 226 (blue spheres) onto the structure of RIα (91-379):cAMP2 (PDB Code: 1RGS). (H) Cyan spheres represent CBD-A residues experiencing solvent accessible surface area (SASA) changes upon deletion of residues 226-379, which are highlighted with a grey surface. This SASA map was built using the same structure as in panel (H).

3.4.2 State-Specific Inter-Domain Interactions as Mapped by CBD-B Deletion.

Figure 3 reports on the comparative NMR analysis of the RIα (91-379) *vs*. RIα (91-244) constructs in their apo *vs*. C- *vs*. $cAMP_2$-bound forms. Figure 3a shows that the cross-peak positions of the RIα (91-244):C complex don't change significantly relative to RIα (91-379):C, which includes the CBD-B as well, suggesting that inter-CBD interactions are negligible in the C-bound state. This conclusion is also supported by the chemical shift similarity between the RIα (91-244):C and RIα (91-379):C complexes (Figure 3b). Considering that the C-subunit of PKA is selective for the inactive-state of both CBDs, panels 3a,b point to negligible inter-CBD interactions when both CBDs adopt the inactive conformation ("inactive-inactive" state).

Figure 3c,d re-examines the RIα (91-379) *vs*. RIα (91-244) comparison shown in panels 3a,b, but in the absence of both C-subunit and cAMP, i.e. for the apo forms of both constructs. Again the majority of the residues of CBD-A do not experience significant chemical shift changes upon deletion of CBD-B (Figure 3c,d), suggesting negligible inter-CBD interactions in apo RIα (91-379). Considering that each CBD in apo RIα (91-379) samples comparable populations of the respective active and inactive states, the absence of detectable inter-CBD contacts in apo RIα (91-379) suggests that in the absence of cAMP inter-CBD interactions are negligible not only in the "inactive-inactive" state, but also in the remaining three combinations, i.e. the "active-inactive", the "inactive-inactive" and the "active-active" states. Overall, our data indicate that CBD-A and B are largely independent of each other when cAMP is absent.

Unlike the cases of apo or C-bound RIα (91-379) (Figure 3a-d), in the presence of excess cAMP the deletion of CBD-B:cAMP causes extensive chemical shift changes in

CBD-A:cAMP (Figure 3e,f), pointing to the presence of significant inter-domain interactions. Interestingly, the residues in CBD-A:cAMP experiencing chemical shift variations upon deletion of CBD-B:cAMP (Figure 3g) are similar to those subject to solvent accessible surface area (SASA) variations upon deletion of RIα (226-379), which includes CBD-B (Figure 3h). The similarity of the residue maps in panels 3g and 3h suggests that the ppm differences observed in Figure 3e,f reflect primarily the disruption of inter-domain contacts upon CBD-B:cAMP deletion as opposed to possible changes in the intra-CBD active *vs*. inactive equilibria. Based on this result, we hypothesized that the contribution of domain-domain interactions to the conformational selection of the active state in both CBDs is negligible compared to the contribution of cAMP. In order to test this hypothesis, we further probed the inter-domain interactions within RIα (91-379):$cAMP_2$ through the W260A point mutation. W260 belongs to CBD-B but contacts through aromatic stacking cAMP bound to CBD-A (Figure 1c). Hence, W260 is expected to play a pivotal role in the cAMP-dependent CBD-A/B interactions [9].

3.4.3 The W260A Point Mutation is Sufficient to Disrupt the CBD-A/B Interface.

The W260A mutation causes major chemical shift changes in the presence of excess cAMP (Figure 4a, green bars) and these changes mimic those caused by the deletion of the whole CBD-B (Figure 4b). These chemical shift patterns suggest the single point W260A mutation is sufficient to disrupt the CBD-A/B interface. The disruption of the CBD-A/B interface caused by the W260A mutation was also independently confirmed through ^{15}N-relaxation measurements, which were analyzed in terms of reduced spectral densities (Figure 5). The W260A mutation causes a decrease in the average J(0) value and a concurrent increase in the average J(ωN) value (Figure 5, red vertical arrows; Table 1), which are indicative of a reduction

of the effective correlation time for overall tumbling, as expected upon de-correlation of the motions of the two adjacent CBDs, i.e. the W260A mutant conforms better than WT to a model of two domains joined by a flexible linker. This result is independently confirmed by the observation that W260A enhances the flexibility of the helical region connecting the two tandem CBDs, as supported by the fact that several residues in this region experience a reduction of J(0) values (Figure 5a, red dashed oval) and an enhanced solvent exposure for (Figure 5a, green arrows) due to the W260A mutation. Hence, the changes in dynamics caused by W260A corroborate the chemical shift perturbation results (Figure 4ab) indicating that the W260A mutation is sufficient to disrupt the CBD-A/B interface.

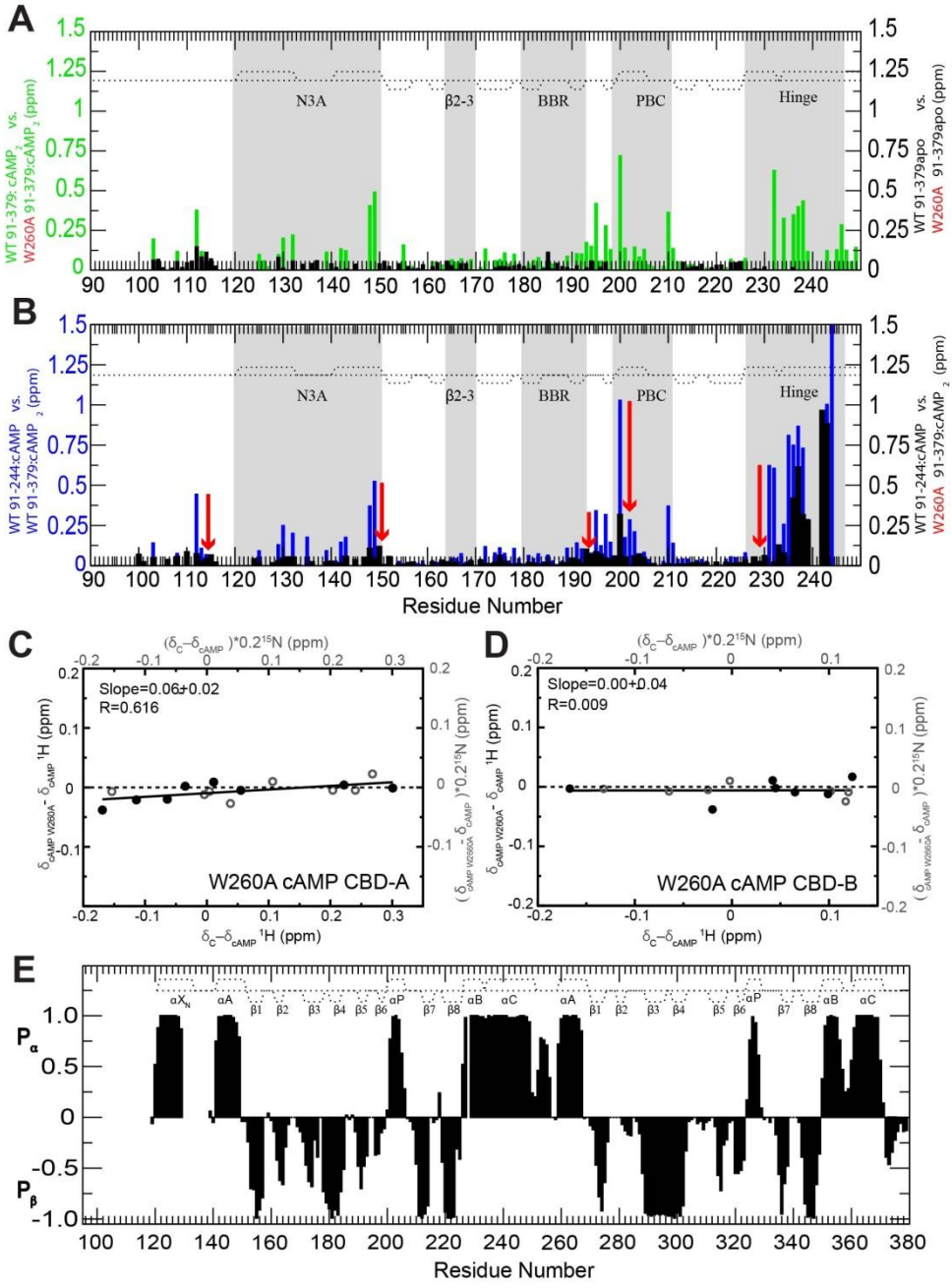

Figure 4: Probing CBD-A/B interactions in RIα (91-379) through the W260A mutation. Evaluation of the effect of the W260A mutation on the CBD-A/B interface through CCS differences in the apo (A) and cAMP-bound states (B). In panel (B), the WT cAMP-bound RIα (91-244) vs. W260A $cAMP_2$-bound RIα (91-379) CCS differences are shown in black. The WT cAMP-bound RIα (91-244) vs. WT $cAMP_2$-bound RIα (91-379) CCS differences are shown in blue. The red arrows illustrate the effect of the W260A mutation. The comparison of the black and blue CCS difference profiles shows that the W260A mutation mimics the deletion of CBD-B. (C) Effect of the W260A mutation on the active vs. inactive equilibrium of CBD-A, as assessed by chemical shift correlation, similarly to Fig. 2D but with apo WT RIα (91-379) replaced by $cAMP_2$-bound W260A RIα (91-379). (D) As panel (C), but for CBD-B. (E) 2^o structure probability map based on the secondary chemical shifts of the W260A mutant RIα (119-379):$cAMP_2$ (black bars). The 2^o structure profile of the WT:$cAMP_2$ is reported as dashed lines.

3.4.4 Dynamics at the CBD-A/B Junction.

The observation that a single point mutation (i.e. W260A) compromises the integrity of a whole inter-CBD surface is suggestive of weak inter-CBD interactions, even in the presence of cAMP. In order to further investigate this hypothesis, we inspected the dynamics of the B-C hinge helices, which join CBD-A to CBD-B. As shown in Figure 5a, these helices exhibit J(0) values that are higher than other regions of the two-domain construct, suggesting the presence of residual ms-μs dynamics or diffusional anisotropy in the inter-domain hinge region even in the presence of excess cAMP. Diffusional anisotropy contributions arise in principle from either the main conformation, represented by the structure of $cAMP_2$-bound RIα [10] with the two CBDs in close contact (Figure 1c), or possibly from minor populations of less compact and highly anisotropic conformers in which the CBD contacts are lost, as in the case of the dumbbell-shaped structure of C-bound RIα [9].

The diffusional anisotropy of both types of conformations was assessed through hydrodynamic simulations (Figure 5a, orange and blue traces) and in both cases a negligible contribution of diffusional anisotropy was determined for the elevated J(0) values observed in the B-C hinge helices connecting CBD-A to CBD-B. The observed J(0) values in the CBD-A hinge region are higher than the J(0) values predicted by hydrodynamic modeling based on the structure of the $cAMP_2$-bound two-domain construct in the absence of internal motions (Figure 5a, orange trace; Table 1). Hence, the anisotropy of this compact conformer cannot account for the J(0) values observed in the hinge:A region (Figure 5a). Furthermore, although the diffusional anisotropy is amplified in the dumbbell-shaped structure observed for the C-bound R-subunit (Figure 5a, blue trace), contributions from this type of conformations to the elevated J(0) values

observed for the hinge region of CBD-A are unlikely, as other regions (e.g. β8 of CBD-B) should then display elevated J(0) values, which is not the case (Figure 5a). These considerations confirm that the elevated J(0) values observed for the B-C hinge helices connecting CBD-A to CBD-B reflect primarily ms-μs residual dynamics, which remains even after cAMP-binding to both domains (Figure 5a). The dynamic nature of the B-C helices joining CBD-A and B calls for an assessment of the role of inter-domain interactions on the intra-CBD conformational equilibria.

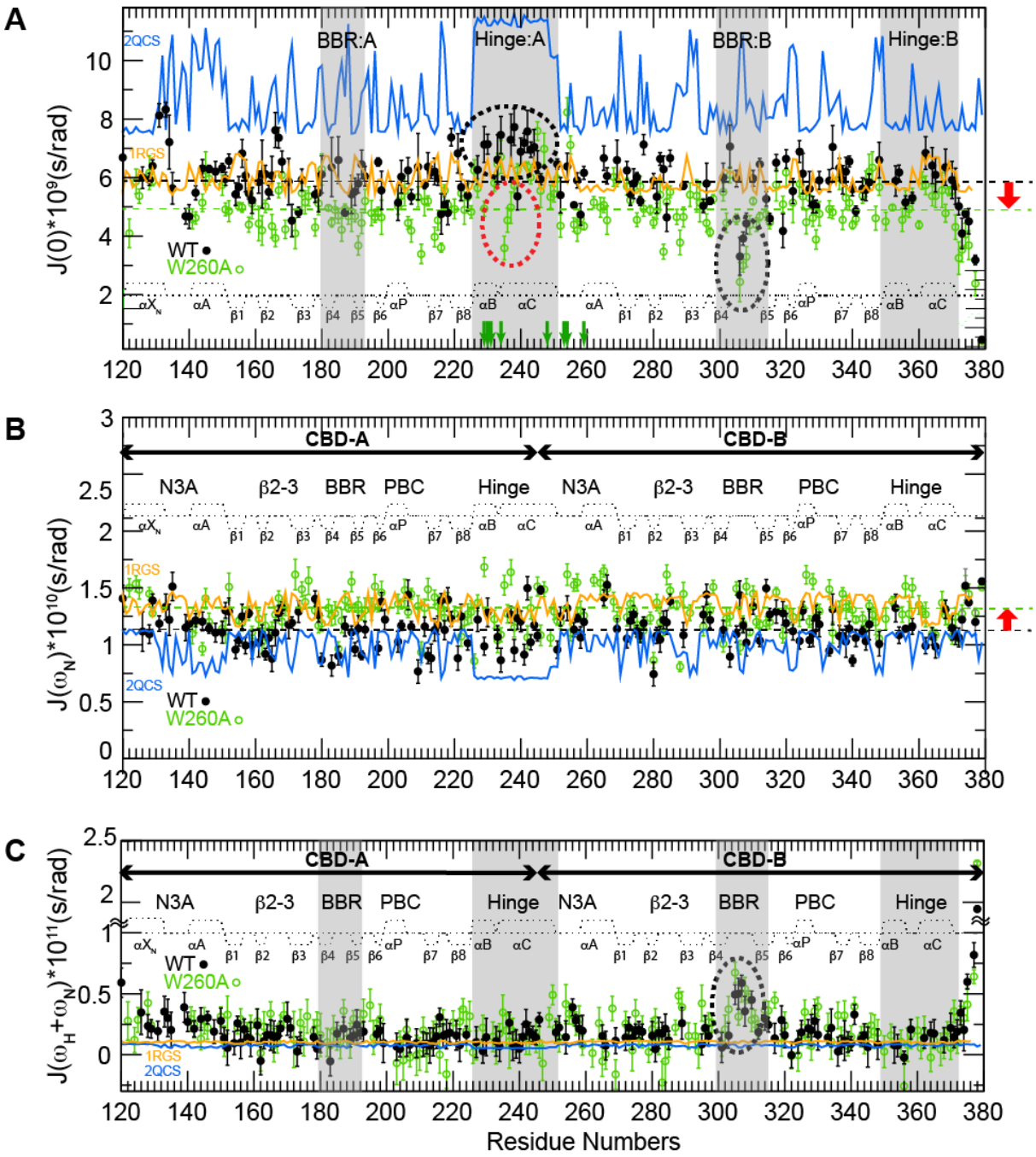

Figure 5: Intra- and Inter-Domain RIα Dynamics. Dynamics of WT (black closed circles) and W260A (green open circles) RIα (119-379):cAMP$_2$ mapped through residue-specific reduced spectra densities at 0 Hz, ωN and ωN + ωH frequencies in panels (A-C), respectively. Green vertical arrows in panel (A) mark residues of the helical region between the two β-barrels that are subject to fast H/D exchange (within the dead time) in W260A but not in the WT sample. The reduced spectra densities predicted based on the cAMP$_2$- and C-bound RIα structures in the absence of internal motions are shown in orange and blue, respectively. The PDB codes of the structures used for the reduced spectra densities prediction are reported in the figure. Key regions subject to significant CBD-A vs. B differences in dynamics profiles are highlighted in grey and with dashed ovals. The dashed horizontal lines in panels (A, B) indicate the average reduced spectra density values at 0 Hz and at ωN for the WT (black) and W260A (green) constructs.

3.4.5 The Contribution of CBD-A/B Interactions to the Intra-CBD Conformational Selection is Marginal

The role of inter-domain interactions on the conformational equilibria of each CBD was probed using the W260A mutation to selectively disrupt the CBD-A/B interface without significantly affecting the structures of the two CBDs, which are largely unperturbed by the mutation (Figure 4e). Specifically, we measured the degree of correlation between the W260A:$cAMP_2$ *vs*. WT:$cAMP_2$ and the WT:C *vs*. WT:$cAMP_2$ chemical shift differences. Similarly to the correlations shown in Fig. 2de, this plot was restricted to residues that are sufficiently removed from the cAMP-dependent interfaces (e.g. R:C, R:cAMP and CBD-A:CBD-B) to report primarily on the active *vs*. inactive equilibrium of each CBD. However, unlike Fig. 2d,e, no significant correlation was observed in either CBD-A or B (Figure 3c,d), confirming the hypothesis that the contribution of inter-CBD interactions to the intra-CBD conformational selection is marginal compared to the contribution of cAMP (Figure 2). This hypothesis is also independently confirmed by previous results based on the RIα (91-244) CBD-A construct, showing linear cross-peak patterns with the apo form found in a central position, as in Figure 2a for CBD-A in the two domain construct [12]. Overall, both the W260A mutation and the CBD-B deletion consistently indicate that cAMP-binding alone is sufficient to almost quantitatively stabilize the active-state of each CBD, even in the absence of CBD-CBD contacts. However, cAMP-binding does not result in a full quenching of dynamics and the profile of residual dynamics after cAMP binding defines distinct differences between the two structurally homologous CBDs.

3.4.6 A *vs*. B Differential CBD:cAMP Dynamics.

The ms-μs residual dynamics detected for the B-C helices is a unique feature of CBD-A, as no noticeable internal dynamics was observed for the B-C helices of CBD-B (Figure 5a). In fact, both J(0) and J(ωH+ωN) spectra densities measured for residues in the B-C helices of CBD-B appear in overall good agreement with the values predicted based on hydrodynamic simulations starting from the $cAMP_2$-bound structure of the R-subunit in the absence of internal motions (Figure 5a,c). Hence, the hinge helix dynamic profile appears to be highly domain-specific. Another region subject to a domain-specific dynamic profile is the base-binding region (BBR). The BBR of CBD-B exhibits elevated J(ωH+ωN) values relative to other regions of CBD-B, with the exception of the C-terminal tail (Figure 5c; Table 1), indicating that the BBR:B is flexible in the ps-ns time-scale. Unlike BBR:B, for BBR:A no internal dynamics was detected, as both J(0) and J(ωH+ωN) spectral densities for BBR:A residues appear in agreement with the values expected based on rigid-body hydrodynamic modeling (Figure 5a,c; Table 1). Overall, distinct dynamic profiles emerge for CBD-A and B, in spite of their structural homology. The B-C helices exhibit ms-μs flexibility in CBD-A but not in CBD-B, while the BBR region is subject to ps-ns dynamics in CBD-B but not in CBD-A (Figure 5; Table 1).

Table 1: Spectral Density Mapping Statistics[a, b]

		CBD-A					
		N3A	**β2-3**	**BBR**	**PBC**	**Hinge**	**Total**
WT	$J(0)\times10^{9}$ (s/rad)	6.13±0.20	6.29±0.38	5.90±0.53	5.81±0.52	**6.80±0.53**	**6.06±0.43**
	$J(\omega_N)\times10^{10}$(s/rad)	1.19±0.07	1.12±0.08	1.00±0.07	1.12±0.08	1.14±0.08	**1.13±0.08**
	$J(\omega_H+\omega_N)\times10^{11}$(s/rad)	0.26±0.08	0.14±0.09	0.15±0.09	0.09±0.10	0.15±0.10	0.16±0.10
W260A	$J(0)\times10^{9}$ (s/rad)	5.58±0.30	4.86±0.31	4.80±0.34	4.92±0.34	5.87±0.36	**5.07±0.33**
	$J(\omega_N)\times10^{10}$ (s/rad)	1.21±0.06	1.25±0.08	1.29±0.07	1.35±0.07	1.27±0.08	**1.30±0.08**
	$J(\omega_H+\omega_N)\times10^{11}$ (s/rad)	0.26±0.08	0.22±0.10	0.21±0.11	0.07±0.11	0.14±0.12	0.19±0.11
2QCS[b]	$J(0)\times10^{9}$ (s/rad)	8.88±1.29	8.75±1.01	8.66±1.13	8.27±0.68	11.19±0.41	8.95±1.42
	$J(\omega_N)\times10^{10}$ (s/rad)	0.96±0.15	0.96±0.12	0.97±0.13	1.01±0.09	0.72±0.03	0.95±0.16
	$J(\omega_H+\omega_N)\times10^{11}$(s/rad)	0.07±0.01	0.07±0.01	0.08±0.01	0.08±0.01	0.06±0.00	0.07±0.01
1RGS[b]	$J(0)\times10^{9}$ (s/rad)	5.91±0.32	5.88±0.33	6.19±0.45	5.83±0.30	6.13±0.32	6.01±0.39
	$J(\omega_N)\times10^{10}$ (s/rad)	1.35±0.07	1.35±0.08	1.29±0.10	1.37±0.07	1.30±0.07	1.33±0.09
	$J(\omega_H+\omega_N)\times10^{11}$ (s/rad)	0.11±0.01	0.11±0.01	0.10±0.01	0.11±0.01	0.10±0.01	0.10±0.01

		CBD-B					
		N3A	**β2-3**	**BBR**	**PBC**	**Hinge**	**Total**
WT	$J(0)\times10^{9}$ (s/rad)	5.88±0.30	5.88±0.35	**5.30±0.36**	5.95±0.45	6.01±0.49	**5.63±0.37**
	$J(\omega_N)\times10^{10}$ (s/rad)	1.26±0.08	1.17±0.09	1.19±0.08	1.14±0.09	1.12±0.08	**1.17±0.08**
	$J(\omega_H+\omega_N)\times10^{11}$ (s/rad)	0.21±0.09	0.16±0.11	**0.33±0.09**	0.19±0.11	0.15±0.09	0.23±0.10
W260A	$J(0)\times10^{9}$ (s/rad)	5.12±0.35	4.85±0.35	4.40±0.27	4.88±0.35	5.32±0.33	**4.87±0.34**
	$J(\omega_N)\times10^{10}$ (s/rad)	1.39±0.07	1.38±0.08	1.24±0.06	1.35±0.07	1.26±0.08	**1.28±0.07**
	$J(\omega_H+\omega_N)\times10^{11}$ (s/rad)	0.18±0.11	0.10±0.13	0.37±0.08	0.20±0.11	0.05±0.12	0.23±0.10
2QCS[b]	$J(0)\times10^{9}$ (s/rad)	8.98±1.45	8.16±0.73	8.33±0.87	8.30±0.96	8.04±0.60	8.49±1.11
	$J(\omega_N)\times10^{10}$ (s/rad)	0.95±0.16	1.04±0.10	1.01±0.10	1.02±0.12	1.05±0.08	1.00±0.13
	$J(\omega_H+\omega_N)\times10^{11}$ (s/rad)	0.07±0.01	0.08±0.01	0.08±0.01	0.08±0.01	0.08±0.01	0.08±0.01
1RGS[b]	$J(0)\times10^{9}$ (s/rad)	5.88±0.37	5.78±0.21	5.89±0.35	5.79±0.36	6.11±0.46	5.87±0.38
	$J(\omega_N)\times10^{10}$ (s/rad)	1.36±0.08	1.38±0.05	1.36±0.08	1.38±0.08	1.31±0.10	1.36±0.09
	$J(\omega_H+\omega_N)\times10^{11}$ (s/rad)	0.11±0.01	0.11±0.00	0.11±0.01	0.11±0.01	0.10±0.01	0.11±0.01

[a] *CBD-A includes residues 119-268, while CBD-B spans residues 244-379. Spectral desnity averages were computed for major allosteric or binding hot spots, which include the N3A motif (residues 119-150), the β2-3 loop (residues 163-171), the BBR (residues 180-193), the PBC (residues 199-211), the hinge (residues 226-251) in CBD-A. For CBD-B, the residue boundaries are: N3A motif (residues 244-268, which includes the W260 lid for CBD-A), β2-3 (residues 281-289), BBR (residues 298-316), PBC (residues 323-335) and hinge (residues 350-370). Average values which are more critical for the discussion (see Text) are highlighted in bold.*

[b] Spectral density values for the RIa (119-379) either bound to the C-subunit (PDB Code: 2QCS) or two equivalents of cAMP (PDB Code: 1RGS) were computed using HydroNMR, which models only the overall tumbling as opposed to internal motions.

3.5 Discussion

A "Double Conformational Selection" Model for the cAMP-Dependent Control of the Inhibitory Interactions Mediated by the CBDs of PKA-RIα. The comparative NMR analysis of the dynamic conformational equilibria of CBD-A and B presented here supports a "double conformational selection" model for the cAMP-dependent activation of PKA RIα (Figure 6a). In the absence of cAMP the PKA-RIα region spanning the two tandem cAMP-binding domains (CBD-A and B), denoted as R_{AB}, samples four states populating a nearly degenerate free-energy landscape, in which each CBD accesses both C-binding competent ("inactive") and C-binding incompetent ("active") conformations with comparable populations, as shown in Figure 2, and independently of the adjacent CBD, due to the absence of significant inter-domain interactions, as shown in Figure 3ab. Out of these four nearly degenerate states, the "inactive-inactive" state exhibits the highest affinity for the C-subunit as both domains are primed for binding C and the inter-domain helical region is also available for interacting with C. The CBD-B affinity for the C-subunit is known to be lower than that of CBD-A, but weak interactions between CBD-B and the C-subunit are still sufficient to drive the conformational equilibria towards the inactive state due to the apo R_{AB} near degeneracy.

The free energy near-degeneracy of apo R_{AB} is eliminated upon binding of two equivalents of cAMP, which select the active state in each CBDs ("active-active" state) and promote CBD-CBD interactions through the lid capping exerted by W260, which is essential to preserve the integrity of the whole CBD-A/B interface, as show in Figure 4ab. The CBD-A/B interface stabilized by cAMP contributes to the dissociation of the R:C complex, because selected CBD-A/B contacts overlap with the R:C interface as revealed by the SASA difference

analysis of Figure 6b,c (dashed rectangles). In addition, the inter-domain interactions stabilized by cAMP result in bending of the C-helix, thus further reducing the affinity of R_{AB} for the PKA catalytic subunit (C), which prefers an elongated unbent C-helix [9]. Overall, the emerging evidence suggests that cAMP contributes to the R:C dissociation through three distinct but concurrent mechanisms: (a) selection of active conformation of CBD-A, which exhibits low affinity for C; (b) selection of active conformation of CBD-B, which further reduces the affinity for C; (c) stabilization of inter-domain interactions that are incompatible with the R:C interface.

Mechanism (a), i.e. intra-CBD-A conformational-selection, significantly contributes to the activation of PKA by cAMP, given the high affinity for C of CBD-A in the inactive state [32]. However, the contributions of (b) and (c) are essential to explain why CBD-B significantly lowers the Ka for the cAMP-dependent activation of PKA [20]. Although the deletion of CBD-B does not appreciably perturb the affinity of R for C [32], mechanism (b), i.e. intra-CBD-B conformational-selection to stabilize the active state of CBD-B, is still pivotal to promote the inter-CBD interactions, which contribute to the release of C through mechanism (c). Interestingly, even in the presence of cAMP the free energy decrease contributed by inter-domain interaction is marginal compared to the free energy of cAMP binding, as CBD-B deletion does not significantly reduce the free energy of unfolding of CBD-A [20, 33] and of cAMP-binding to CBD-A [12, 13, 34, 35]. Hence, the “closed” inter-domain topology of R_{AB}:$cAMP_2$, in which W260 from CBD-B caps cAMP in CBD-A, exists in a dynamic equilibrium with minor populations of an “open” active-active state, in which inter-domain coupling is negligible (Figure 6a). Since intra-domain conformational selection in R_{AB} relies primarily on cAMP binding with only negligible contributions from domain-domain interactions (Figure 4c,d),

in such an "open" topology of R_{AB}:$cAMP_2$, which is mimicked by the W260A mutant, the active state selection within each CBD is not compromised, i.e. mechanisms (a) and (b) are still effective, but mechanism (c) is not activated.

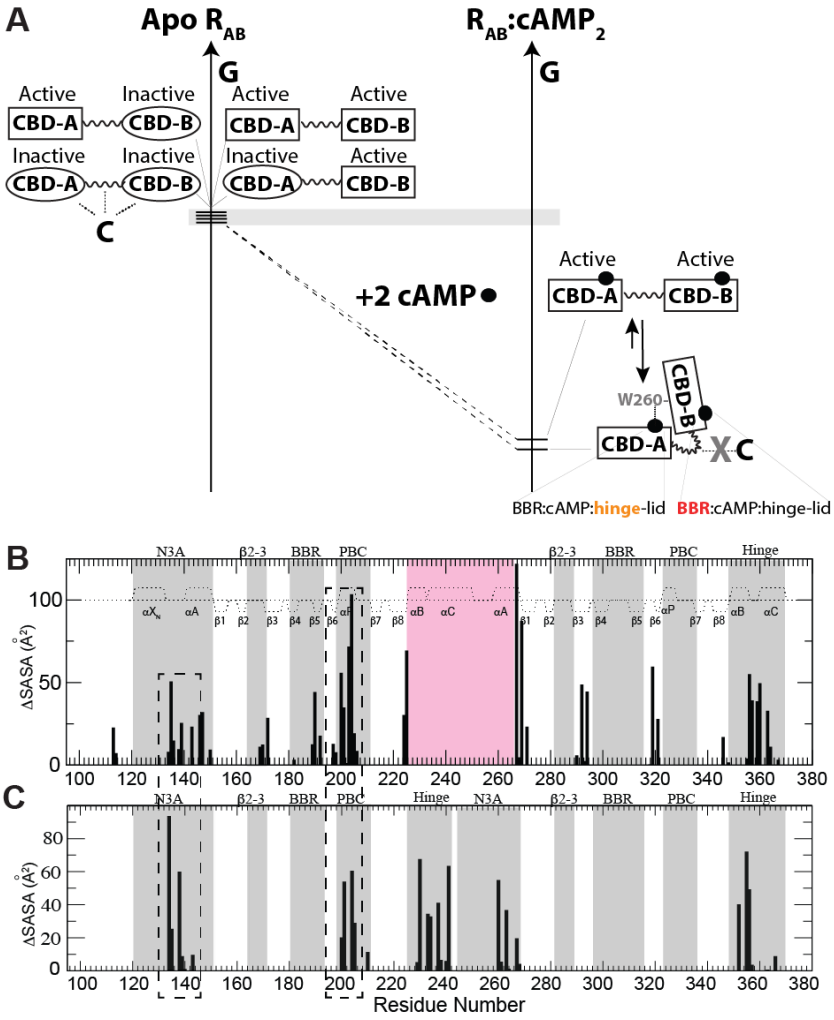

Figure 6: "Double Conformational Selection" Model proposed for PKA-RIα. **(A)** The CBD-specific active and inactive states are represented through ovals and rectangles, respectively. The grey horizontal bar indicates that free energy differences are of the order of ~RT. Dotted lines denote interactions with the C-subunit of PKA. cAMP is shown as solid black circles. R_{AB} refers to the PKA-RIα region spanning the two tandem cAMP-binding domains (CBD-A and B). The cAMP recognition motifs for both CBDs are reported as BBR:cAMP:hinge-lid, where BBR stands for base-binding region and orange (red) denotes enhanced ms-μs (ps-ns) dynamics. See text in the Discussion text for a full explanation. **(B)** Inter-domain contact profile based on SASA changes upon deletion of the helical inter-domain region (red area) from the structure of $cAMP_2$-bound RIα (91-379) (PDB Code: 1RGS). **(C)** Profile of RIα (91-379):C contact as mapped by SASA variations upon deletion of the C-subunit from the sructure of the RIα (91-379):C complex (PDB Code: 2QCS). Regions experiencing SASA changes in both panels (B) and (C) (i.e. residues involved in both CBD-A/B contacts as well as interactions with the C-subunit) are highlighted by dashed boxes.

A critical feature of the double conformational selection model proposed here to explain the functional role of CBD-B (Figure 6a) is the near free energy degeneracy of the states sampled by apo R_{AB}. This degeneracy is quite unique of PKA RIα, as it was not observed for other structurally homologous CBDs, such as those of the hyperpolarization and cyclic nucleotide activated (HCN) ion channels for which conformational selection relies on apo equilibria that are skewed towards the inactive (auto-inhibited) state with typically low affinity for cAMP [23]. This observation provides a possible explanation as to why both CBDs of PKA RIα bind cAMP with higher affinity than HCN, in spite of the structural homology among eukaryotic CBDs. Furthermore, our investigation revealed marked differences in dynamics also among homologous CBDs in their cAMP-bound forms. For example, in both CBD-A and B of PKA RIα the adenine base of cAMP is sandwiched by β-strands 4 and 5 (Base Binding Region or BBR) on one side and on the other side by an aromatic side chain lid (i.e. W260 in CBD-A and Y371 in CBD-B), which is part of hinge helices that are C-terminal to the β-subdomains of the respective CBDs. Despite this structural pattern of cAMP recognition through the BBR and hinge helix-lid motifs is conserved in both CBDs, the BBR:B is significantly more dynamic in the ps-ns timescale than the BBR:A, while the hinge:A is significantly more dynamic in the ms-μs timescale than the hinge:B (Figure 6a). The hinge:A dynamics explains why CBD-A in RIα tolerates without major affinity losses cAMP analogues with bulky substituents at the adenine C8 better than anticipated based on the narrow pocket observed in the static structure [36]. In general, these observations corroborate the notion that structurally homologous domains may still exhibit marked differences in dynamic profiles that affect affinities and recognition, opening new opportunities for the design of selective ligands that target specific eukaryotic CBDs.

3.6 Acknowledgements

We thank B. VanSchouwen, J. Byun, S. Boulton, N. Jafari, and M. Gloyd for helpful discussion. This work was supported by the Canadian Institutes of Health Research (CIHR).

3.7 References

1. Taylor, S.S., and Kornev, A.P. (2011) Protein kinases: evolution of dynamic regulatory proteins. *Trends Biochem.Sci.* **36,** 65-77

2. Serezani, C.H., Ballinger, M.N., Aronoff, D.M., and Peters-Golden, M. (2008) Cyclic AMP: master regulator of innate immune cell function. *Am.J.Respir.Cell Mol.Biol.* **39,** 127-132

3. Stork, P.J., and Schmitt, J.M. (2002) Crosstalk between cAMP and MAP kinase signaling in the regulation of cell proliferation. *Trends Cell Biol.* **12,** 258-266

4. Shabb, J.B. (2001) Physiological substrates of cAMP-dependent protein kinase. *Chem.Rev.* **101,** 2381-2411

5. Hanks, S.K., and Hunter, T. (1995) Protein kinases 6. The eukaryotic protein kinase superfamily: kinase (catalytic) domain structure and classification. *FASEB J.* **9,** 576-596

6. Beebe, S. J.; Corbin, J. D. (1986) The Enzymes: Control by Phosphorylation; Academic Press, Inc.:New York, 43-111

7. Johnson, D.A., Akamine, P., Radzio-Andzelm, E., Madhusudan, M., and Taylor, S.S. (2001) Dynamics of cAMP-dependent protein kinase. *Chem.Rev.* **101,** 2243-2270

8. Taylor, S.S., Kim, C., Vigil, D., Haste, N.M., Yang, J., Wu, J., and Anand, G.S. (2005) Dynamics of signaling by PKA. *Biochim.Biophys.Acta.* **1754,** 25-37

9. Kim, C., Cheng, C.Y., Saldanha, S.A., and Taylor, S.S. (2007) PKA-I holoenzyme structure reveals a mechanism for cAMP-dependent activation. *Cell.* **130,** 1032-1043 D

10. Su, Y., Dostmann, W.R., Herberg, F.W., Durick, K., Xuong, N.H., Ten Eyck, L., Taylor, S.S., and Varughese, K.I. (1995) Regulatory subunit of protein kinase A: structure of deletion mutant with cAMP binding domains. *Science.* **269,** 807-813

11. Wu, J., Jones, J.M., Nguyen-Huu, X., Ten Eyck, L.F., and Taylor, S.S. (2004) Crystal structures of RIalpha subunit of cyclic adenosine 5'-monophosphate (cAMP)-dependent protein kinase complexed with (Rp)-adenosine 3',5'-cyclic monophosphothioate and (Sp)-adenosine 3',5'-cyclic monophosphothioate, the phosphothioate analogues of cAMP. *Biochemistry.* **43,** 6620-6629

12. Akimoto, M., Selvaratnam, R., McNicholl, E.T., Verma, G., Taylor, S.S., and Melacini, G. (2013) Signaling through dynamic linkers as revealed by PKA. *Proc.Natl.Acad.Sci.U.S.A.* **110,** 14231-14236

13. Herberg, F.W., Taylor, S.S., and Dostmann, W.R. (1996) Active site mutations define the pathway for the cooperative activation of cAMP-dependent protein kinase. *Biochemistry.* **35,** 2934-2942

14. Wu, J., Brown, S., Xuong, N.H., and Taylor, S.S. (2004) RIalpha subunit of PKA cAMP-free structure reveals a hydrophobic capping mechanism for docking cAMP into site B. *Structure.* **12,** 1057-1065

15. Cheng, C.Y., Yang, J., Taylor, S.S., and Blumenthal, D.K. (2009) Sensing domain dynamics in protein kinase A-I{alpha} complexes by solution X-ray scattering. *J.Biol.Chem.* **284,** 35916-35925

16. Vigil, D., Blumenthal, D.K., Taylor, S.S., and Trewhella, J. (2005) The conformationally dynamic C helix of the RIalpha subunit of protein kinase A mediates isoform-specific domain reorganization upon C subunit binding. *J.Biol.Chem.* **280,** 35521-35527

17. Gullingsrud, J., Kim, C., Taylor, S.S., and McCammon, J.A. (2006) Dynamic binding of PKA regulatory subunit RI alpha. *Structure.* **14,** 141-149

18. McNicholl, E.T., Das, R., SilDas, S., Taylor, S.S., and Melacini, G. (2010) Communication between tandem cAMP binding domains in the regulatory subunit of protein kinase A-Ialpha as revealed by domain-silencing mutations. *J.Biol.Chem.* **285,** 15523-15537

19. Byeon, I.J., Dao, K.K., Jung, J., Keen, J., Leiros, I., Doskeland, S.O., Martinez, A., and Gronenborn, A.M. (2010) Allosteric communication between cAMP binding sites in the RI subunit of protein kinase A revealed by NMR. *J.Biol.Chem.* **285,** 14062-14070

20. Das, R., Esposito, V., Abu-Abed, M., Anand, G.S., Taylor, S.S., and Melacini, G. (2007) cAMP activation of PKA defines an ancient signaling mechanism. *Proc.Natl.Acad.Sci.U.S.A.* **104,** 93-98

21. Selvaratnam, R., Vanschouwen, B., Fogolari, F., Mazhab-Jafari, M.T., Das, R., and Melacini, G. (2012) The Projection Analysis of NMR Chemical Shifts Reveals Extended EPAC Autoinhibition Determinants. *Biophys.J.* **102,** 630-639

22. Das, R., Mazhab-Jafari, M.T., Chowdhury, S., SilDas, S., Selvaratnam, R., and Melacini, G. (2008) Entropy-driven cAMP-dependent allosteric control of inhibitory interactions in exchange proteins directly activated by cAMP. *J.Biol.Chem.* **283,** 19691-19703

23. Akimoto, M., Zhang, Z., Boulton, S., Selvaratnam, R., VanSchouwen, B., Gloyd, M., Accili, E.A., Lange, O.F., and Melacini, G. (2014) A mechanism for the auto-inhibition of hyperpolarization-activated cyclic nucleotide-gated (HCN) channel opening and its relief by cAMP. *J.Biol.Chem.* **289,** 22205-22220

24. Delaglio, F., Grzesiek, S., Vuister, G.W., Zhu, G., Pfeifer, J., and Bax, A. (1995) Nmrpipe - a Multidimensional Spectral Processing System Based on Unix Pipes. *J.Biomol.NMR.* **6,** 277-293

25. T. D. Goddard and D. G. Kneller University of California, San Francisco SPARKY**3,**

26. Sattler, M., Schleucher, J., and Griesinger, C. (1999) Heteronuclear multidimensional NMR experiments for the structure determination of proteins in solution employing pulsed field gradients. *Prog Nucl Magn Reson Spectrosc.* **34,** 93-158

27. Salzmann, M., Pervushin, K., Wider, G., Senn, H., and Wuthrich, K. (1998) TROSY in triple-resonance experiments: new perspectives for sequential NMR assignment of large proteins. *Proc.Natl.Acad.Sci.U.S.A.* **95,** 13585-13590

28. Eghbalnia, H., Bahrami, A., Wang, L., Assadi, A., and Markley, J. (2005) Probabilistic identification of spin systems and their assignments including coil-helix inference as output (PISTACHIO). *J.Biomol.NMR.* **32,** 219-233

29. Das, R., and Melacini, G. (2007) A model for agonism and antagonism in an ancient and ubiquitous cAMP-binding domain. *J.Biol.Chem.* **282,** 581-593

30. Bernado, P., Garcia de la Torre, J., and Pons, M. (2002) Interpretation of 15N NMR relaxation data of globular proteins using hydrodynamic calculations with HYDRONMR. *J.Biomol.NMR.* **23,** 139-150

31. Garcia de la Torre, J. (2001) Building hydrodynamic bead-shell models for rigid bioparticles of arbitrary shape. *Biophys.Chem.* **94,** 265-274

32. Sjoberg, T.J., Kornev, A.P., and Taylor, S.S. (2010) Dissecting the cAMP-inducible allosteric switch in protein kinase A RIalpha. *Protein Sci.* **19,** 1213-1221

33. Canaves, J.M., Leon, D.A., and Taylor, S.S. (2000) Consequences of cAMP-binding site mutations on the structural stability of the type I regulatory subunit of cAMP-dependent protein kinase. *Biochemistry.* **39,** 15022-15031

34. Akimoto, M., Moleschi, K., Boulton, S., VanSchouwen, B., Selvaratnam, R., Taylor, S.S., and Melacini, G. (2014) Allosteric linkers in cAMP signalling. *Biochem.Soc.Trans.* **42,** 139-144

35. Boulton, S., Akimoto, M., Vanschouwen, B., Moleschi, K., Selvaratnam, R., Giri, R., and Melacini, G. (2014) Tapping the translation potential of cAMP signalling: molecular basis for selectivity in cAMP agonism and antagonism as revealed by NMR. *Biochem.Soc.Trans.* **42,** 302-307

36. Schwede, F., Christensen, A., Liauw, S., Hippe, T., Kopperud, R., Jastorff, B., and Doskeland, S.O. (2000) 8-Substituted cAMP analogues reveal marked differences in adaptability, hydrogen bonding, and charge accommodation between homologous binding sites (AI/AII and BI/BII) in cAMP kinase I and II. *Biochemistry.* **39,** 8803-8812

Chapter 4

Intracellular Linker Control by the HCN4 CBD

4.1 Author's Preface

This research was originally published in The Journal of Biological Chemistry. © the American Society for Biochemistry and Molecular Biology. Full citation is as follows:

Akimoto, M., Z. Zhang, S. Boulton, R. Selvaratnam, B. VanSchouwen, M. Gloyd, E.A. Accili, O.F. Lange, and G. Melacini. 2014. A mechanism for the auto-inhibition of hyperpolarization-activated cyclic nucleotide-gated (HCN) channel opening and its relief by cAMP. J. Biol. Chem. 289: 22205–22220.

I conducted most of the experiments necessary for the manuscript. Dr. O.F. Lange and Z. Zhang performed structure modeling with CS-Rosetta. Stephen Boulton performed STD and CHEPA analysis. Rajeevan Selvaratnam performed the assignment of mutant HCN4 (563-724). Bryan VanSchouwen performed and analyzed all MD simulations. M. Gloyd worked on protein purification. Dr. E.A. Accili provided HCN plasmids. I co-wrote the manuscript with Dr. Giuseppe Melacini.

4.2 Introduction

The hyperpolarization-activated cyclic nucleotide-gated (HCN) ion channels contribute to electrical activity in neurons and cardiomyocytes [1-22]. Four homologous mammalian HCN variants are known to date (HCN1-4) that share a similar multi-domain organization with an N-terminal trans-membrane region (TR) and a C terminal intracellular region (IR) [1]. As for closely-related voltage-gated potassium channels, the HCN TR is thought to form a tetrameric ion channel, with each subunit of the tetramer composed of six helices. The IR includes a linker with six additional helices (A'-F' or "C-linker") that connect the TR to a C-terminal cAMP-binding domain (CBD) (Figure 1a,b) [1]. Although HCN channels are primarily activated by hyperpolarization of the membrane potential, their opening is variably facilitated by cAMP binding to the CBD, with HCN2 and HCN4 responding strongly to cAMP, HCN1 responding to a lesser extent and HCN3 being unaffected by cAMP [1-4]. The cAMP-dependent modulation of HCN4 activity is a key determinant for the increased heart rate induced by β-adrenergic agonists [3, 4]. This is because in the absence of cAMP the CBD causes a tonic inhibition of the HCN channel [21, 23] and binding of cAMP to the CBD relaxes the inhibition of the inner gate, such that opening by hyperpolarization occurs more easily [21-23].

The crystal structures of the cAMP-bound (holo) IR have been solved for HCN1, 2 and 4 (Figure 1c) [1, 21, 22]. No significant differences have been observed among the secondary, tertiary and quaternary structures of the holo IR for these HCN isoforms, which assemble to form a highly conserved homo-tetramer with a four-fold rotational symmetry [1, 21, 22]. Although linker tetramerization is cAMP-dependent, the inter-subunit contacts in the tetramer are mediated by the linker helices A'-D', which are located more than 20 Å away from the cAMP

binding site in the CBD. The HCN CBD is composed of a contiguous β-subdomain and a non-contiguous α-subdomain (Figure 1a). The β-subdomain forms a β-barrel that contains the phosphate binding cassette (PBC; Figure 1c), whereas the all helical α-subdomain includes an N-terminal A-helix, directly connected to the C-linker, and two C-terminal helices critical for HCN activation (B and C; Figure 1a,c) [1]. In the cAMP-bound structure of HCN the B-C helices, which are in close proximity to the PBC and cAMP, separate the PBC from the N-terminal helices E'-F'-A, which are collectively referred to as the N3A motif (Figure 1c) [24]. This α-subdomain tertiary structure is denoted as the "N3A out/B-C in" topology, where in and out refer to the orientation relative to the PBC and the β-subdomain.

Although the holo IR structure provides an invaluable picture of the IR in its active state, it is still unclear how the apo IR causes tonic inhibition of the HCN channel, and how cAMP releases this inhibition. As a first step towards addressing this question, the crystal structure of the tetrameric apo HCN2 IR was solved, but was found to be virtually identical to that of the holo HCN2 IR (rmsd = 0.5 Å) with the exception of partial uncoiling of the F'-helix and of the C-terminal half of the C-helix, which was unresolved [25]. However, it has been suggested that the similarity between the apo and holo HCN2 IR tetramer structures might at least in part be due to crystal packing, and a co-crystallized bromide ion mimicking the cAMP phosphate [25], as also observed for other apo CBDs [26, 27]. Furthermore, size exclusion chromatography and analytical ultracentrifugation indicate that in solution the IR of HCN2 and HCN4 is primarily monomeric in the apo form, with no tetrameric IR detected [11, 21]. However, only sparse structural information is currently available on the apo IR monomer.

Solution FRET data on the monomeric HCN2 IR point to large scale movements in the CBD C-terminus upon cAMP-binding, resulting in a cAMP-induced disorder to order transition for the distal half of the C-helix coupled to a possible rearrangement of the F' helix [25]. The above studies begin to identify potential alterations in the C-linker and CBD that occur upon cAMP binding to facilitate HCN opening, but it remains still unclear how these alterations actually promote oligomerization of the C-linker and if other conformational or dynamic changes are also required for the cAMP-dependent control of the gating ring that disinhibits channel opening. To address these questions, more information is needed on the changes caused by cAMP-binding to the apo IR HCN monomer.

Herein, we probe by NMR the cAMP-dependent changes in the apo HCN4 IR monomer in solution. For this purpose, we utilize an HCN4 construct, i.e. human HCN4 (563-724), that is stabilized in the monomeric state through the deletion of the A'-B' helices required for tetramerization [11, 13, 21]. This HCN4 segment spans the linker helices C'-F' as well as the CBD and is referred to here as the 'extended CBD' or 'eCBD' (Figure 1b). The eCBD was analyzed by NMR in the apo form and bound to either cAMP or the cCMP partial agonist. Surprisingly, our comparative NMR analyses reveal that cAMP-binding to the HCN4 eCBD monomer does not significantly affect the C' and D' helices of the C-linker, which remain predominantly unstructured when monomeric. However, cAMP drives a drastic change in the remaining eCBD from tetramerization- incompetent to tetramerization-competent structures. The apo eCBD exists in a pre-equilibrium between these states, in which tetramerization-incompetent conformations prevail. Tetramerization-incompetency arises from the orientation of the β-subdomain relative to the E', F' and A-C helices observed in the absence of cAMP, which is

sterically incompatible with the tight CBD packing required for tetramerization, explaining why the apo IR is primarily monomeric. Overall, our experiments support a mechanism proposed to rationalize not only why the apo CBD contributes to the tonic inhibition of the inner gate, but also how cAMP releases this inhibition and facilitates channel opening.

4.3 Materials and Methods

Protein Expression and Purification: HCN4 (563-724) and HCN4 (579-707) were subcloned into a pET302NT-His vector (Invitrogen) as a rare codon optimized fusion construct with SUMO connected to the N-terminus of HCN4 by a TEV cleavable linker. Both HCN4 constructs were then expressed in the Escherichia coli strain BL-21(DE3). Cells were grown in M9 minimal media and induced with 0.5 mM Isopropyl β-D-1-thiogalactopyranoside at an optical density of 0.6-0.9 (λ=600 nm), and further incubated at 18-20°C for 16 hrs. After harvesting, the cells were re-suspended in the lysis buffer (10 mM HEPES, pH 7.4 with 250 mM KCl and 10% glycerol) and lysed by French Press. The cell lysate was centrifuged and the supernatant was further purified by Ni-NTA affinity chromatography with wash buffer (10 mM HEPES, pH 7.4 with 250 mM KCl, 10 mM 2-mercaptoethanol and 20 mM imidazole) and elution buffer (10 mM HEPES, pH 7.4 with 250 mM KCl, 10 mM 2-mercaptoethanol and 250 mM imidazole). The His_6-SUMO was cleaved by His_6-tagged TEV protease prior to a second Ni^{2+} column purification to remove both the cleaved His_6-SUMO and TEV. The cleaved protein was further purified by gel filtration on a Superdex 75 column.

General NMR Spectroscopy: All NMR spectra were recorded at a temperature of 27°C, unless otherwise specified, using a Bruker AV 700 spectrometer equipped with a TCI cryo-probe or Bruker AV III 850 MHz AscendTM spectrometer equipped with a PATXI probe and processed

with NMRpipe [28] employing linear prediction, unless otherwise specified, and a resolution enhancing 60° shifted sine squared bell window function. All spectra were analyzed with Sparky [29] using Gaussian line-fitting. Assignments were obtained either through triple-resonance 3D experiments (i.e. HNCO, HNCA, HN(CO)CA, CC(CO)NH, H(CCCO)NH, HCCH-TOCSY, CBCA(CO)NH and HNCACB) [30] and/or through spectral comparisons, if no ambiguities were present. For the triple resonance data acquisition, uniformly ^{15}N and ^{13}C labeled HCN4 (579-707) was concentrated to 500 µM in 20 mM MES (pH 6.5), 100 mM KCl, 1 mM DTT, 2 mM EDTA, 2 mM EGTA, 0.02 % sodium azide and 5 % $^{2}H_2O$. The secondary structure probabilities were determined using the secondary chemical shifts via the PECAN software [31]. Other specific NMR experiments are discussed below.

Affinity Measurement: Titration of 10 µM HCN4 (563-724) with cAMP was performed at 25°C in 20 mM potassium phosphate buffer, pH 6.5, 50 mM KCl, >99% D_2O. Saturation transfer difference (STD) 1D spectra were acquired using a 50 ms spin-lock to minimize interference from protein signals [32]. The spectral width was 8389.26 Hz centered at 4.72 ppm. Spectra were digitized with 16 K complex points. The on-resonance saturation frequency was 0.57 ppm while the off-resonance reference frequency was 30 ppm. The STD amplification factor (STD_{af}) was calculated as the product of the STD/STR ratio for the cAMP ribose H1' singlet peak at 6.2 ppm, with the ratio of total cAMP and HCN concentrations. STD_{af} values were then normalized with the equation:

$$\langle v \rangle = (STD_{af,[cAMP]} - STD_{af,[cAMP]=0}) / (STD_{af,[cAMP]plateau} - STD_{af,[cAMP]=0}) \quad [1]$$

with <v> = $[PL]/[P]_{Tot}$. Error bars were determined starting from the spectral noise. Binding isotherms where then fitted using the quadratic equation derived from the dissociation constant equilibrium equation Kd = [P][L]/[PL]. The Kd was determined by minimizing the experimental *vs*. calculated <v> rmsd.

Chemical Shift Analysis: Uniformly ^{15}N-labeled HCN4 (563-724) was concentrated to 100 µM in 20 mM MES (pH 6.5), 100 mM KCl, 1 mM DTT, 2 mM EDTA, 2 mM EGTA, 0.02 % sodium azide and 5 % $^{2}H_2O$. Stock solutions of cCMP (Biolog) and cAMP (Sigma) were prepared using the same buffer as for the protein solution. Starting from the apo samples, stock solutions of the cyclic nucleotide ligands (25 mM) were titrated into the protein solution to full saturation (the final concentrations of ligands were 2.5 mM for cAMP and 5 mM for cCMP). Sensitivity enhanced ^{15}N-^{1}H hetero-nuclear single quantum coherence (HSQC) spectra with 190 (t1) and 1024 (t2) complex points and spectral widths of 31.82 ppm and 14.056 ppm for the ^{15}N and ^{1}H dimensions, respectively, were recorded with 16 scans and a recycle delay of 1.0 s. The ^{1}H and ^{15}N carrier frequencies were set at the water resonance and in the middle of the amide region, respectively. The combined ^{15}N and ^{1}H chemical shifts ($\delta^{1}H+0.2\ \delta^{15}N$) from the HSQC spectra of apo and cAMP, cCMP-bound HCN4 (563-724) were analyzed using the chemical shift projection analysis (CHESPA), according to previously published protocols [33, 34].

HN-NOE Measurements: HN-NOE data were acquired as previously reported [35, 36] and processed without linear prediction. A 10 s recycle delay was used to include a 5 s proton saturation period. Data were collected in 10 sets of saturated and unsaturated spectra using uniformly ^{15}N-labeled HCN4 (563-724) and HCN4 (579-707) samples concentrated to 100 µM in 20 mM MES (pH 6.5), 100 mM KCl, 1 mM DTT, 2 mM EDTA, 2 mM EGTA, 0.02 % sodium azide

and 5 % $^{2}H_2O$. All spectra were co-added before processing using NMRpipe, resulting in a total 40 scans per serial file for each HN-NOE experiment (with and without ^{1}H saturation). The steady state HN-NOE values were computed as the ratio of the intensities in saturated to unsaturated spectra. The error on the HN-NOE values were gauged based on the standard deviation between fit heights in replicate spectra.

H/H Exchange. Amide proton H/H exchange spectra were acquired as previously described [32, 35] using the HCN4 (563-724) construct. The protein was concentrated to 100 µM in 20 mM MES (pH 6.5), 100 mM KCl, 1 mM DTT, 2 mM EDTA, 2 mM EGTA, 0.02 % sodium azide and 5 % $^{2}H_2O$. The cAMP bound sample was prepared by adding 1 mM cAMP in the buffer.

Residual Dipolar Coupling (RDC) Measurements. The residual dipolar coupling were measured in the presence and absence of pf1 (Alsa Biotech) using sensitivity-enhanced IPAP-type $^{1}H,^{15}N$ HSQC experiment [37, 38]. The spectra were acquired with 128 (t1) and 1024 (t2) complex points and spectral widths of 31.82 ppm and 14.056 ppm for the ^{15}N and ^{1}H dimensions, respectively, with 8 scans and a recycle delay of 1.0 s. HCN4 (579-707) was concentrated to 200 µM in 20 mM MES (pH 6.5), 100 mM KCl, 1 mM EDTA, 1 mM DTT, 0.02 % sodium azide and 5 % $^{2}H_2O$. The anisotropic sample of HCN4 (579-707) was prepared with a 6 mg/ml final concentration of pf1 phage.

NOE Measurements: Methyl-Methyl NOEs were measured using a ^{1}H-^{13}C HSQC-NOESY-^{1}H-^{13}C HSQC experiment [39] for ILV methyl selectively ^{13}C-labeled $^{2}H^{15}N$ HCN4 (579-707). The protein was expressed in deuterated M9 media and one hour prior to induction, 100 mg of methyl ^{13}C α-ketoisovalreic acid and 100 mg of methyl ^{13}C α-ketobutyric acid were

added to the media. The protein was concentrated to 250 µM in 25 mM phosphate buffer (pH 6.5) 100 mM KCl, 99 % $^{2}H_2O$. The mixing times were 200 and 300 ms. The NOESY-^{15}N HSQC and ^{15}N-HSQC-NOESY-^{15}N HSQC experiments [30] were acquired using uniformly $^{13}C^{15}N$-labeled HCN4 (579-707). The mixing time were 130 ms. The protein was concentrated to 250 µM in 20 mM MES (pH 6.5), 100 mM KCl, 1 mM EDTA, 1 mM DTT, 0.02 % sodium azide and 5 % $^{2}H_2O$.

Spin Labeling and Paramagnetic Relaxation Enhancement (PRE) Analysis: The spin label 1-oxyl-2,2,5,5-tetra- methyl-pyrroline-3-methyl-methanethio-sulfonate (MTSL) was covalently attached to the free cysteine residue in the HCN4 (579-707). The reducing reagent was exchanged using a PD10 column before the addition of MTSL [35]. The reduced HCN4 (579-707) was incubated with a threefold molar excess of MTSL for 3 h at room temperature. The PREs were quantified through oxidized *vs*. reduced rates cross-peak intensities [40] in sensitivity-enhanced $^{1}H^{15}N$ hetero-nuclear single quantum coherence (HSQC) spectra with 256 (t1) and 1024 (t2) complex points and spectral widths of 31.82 and 14.06 ppm for the ^{15}N and ^{1}H dimensions, respectively. Ninety-six scans were recorded with a recycle delay of 1.50 s. After recording the data for the paramagnetic state, 5 mM DTT was added to obtain the diamagnetic control. The diamagnetic sample was incubated at room temperature for 1 h, after which we repeated the same experiments carried out for the paramagnetic sample [35]. HSQC intensity ratios were then calculated as I_{ox}/I_{red}, where I_{ox} is the intensity of signal with MTSL and I_{red} is the intensity in reduced sample with DTT.

Structure Calculations by CS-Rosetta [41-52]. The RASREC algorithm from the CS-Rosetta [43, 45] methodology was employed to calculate the structures of HCN4. In addition to chemical shift and residual dipolar couplings, distance restraints were generated from remote

homologous structures using the CS-HM protocol [41, 51]. Homologous protein structures and their alignment to the target sequence were determined with HHSEARCH (Ver. 2.0.16). The generated alignments spanned residues 588-705, which are nearly the entire modeled region of HCN4. Fragments were picked through the Rosetta3 fragment picker [42, 43] using backbone chemical shifts. From the RASREC pool, which was set to a size of 500, we selected the ten lowest energy structures as final models. A second calculation was carried out with additional distance restraints derived from methyl-methyl and methyl-HN NOEs in an ILV labeled sample. Atomic coordinates of apo HCN4 (579-707) have been deposited in the Protein Data Bank with entry code 2MNG.

4.4 Results

cAMP-Binding to the Monomeric HCN4 eCBD Causes Pervasive Structural Changes in the E'-C Helices. As a first step in the validation of the HCN4 construct used in our initial NMR studies, i.e. the human HCN4 (563-724) (eCBD; Figure 1), we monitored cAMP-binding through saturation transfer difference (STD) experiments (Figure 2a). Figure 2a shows the cAMP-binding isotherm for the HCN4 eCBD, which exhibits a clear dose-response pattern with a well-defined plateau, indicative of specific cAMP:eCBD interactions. In addition, non-linear fitting to a 1:1 binding model resulted in a Kd value in the 1-9 μM range, which is consistent with affinities previously reported for monomeric HCN4 and longer HCN4 constructs at similar concentrations [11, 21]. We then acquired HN HSQC spectra of the HCN4 eCBD in the absence of cAMP and in the presence of saturating amounts of cAMP (Figure 2b) to probe at residue resolution the effect of cAMP-binding.

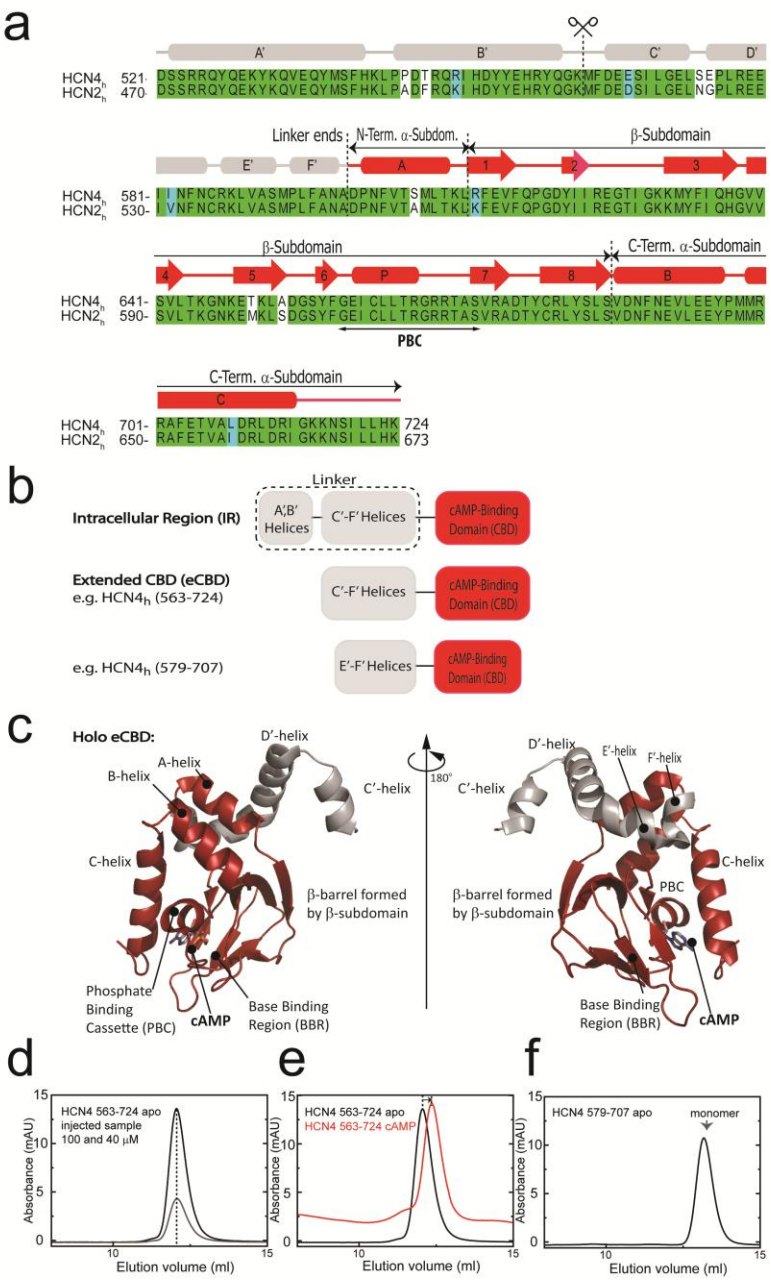

Figure 1: Construct design and architecture of cAMP-bound HCN. The linker and cAMP-Binding Domain (CBD) regions are displayed in grey and red, respectively. (a) Sequence alignment of the CBDs of human HCN2 and human HCN4. The location of α-helices and β-strands is shown using red rectangles and arrows, respectively, and was inferred from the crystal structure of cAMP-bound HCN4 (PDB Code: 3OTF) (22). (b) Domain organization of the intracellular region of HCN4. The human HCN4 (563-724) construct was investigated by NMR here. (c) Structure of HCN4 (563-724) bound to cAMP (PDB code: 3OTF) (22). (d-f) Analytical Size Exclusion Chromatography (SEC) data of human HCN4. (d) Effect of dilution on apo HCN4 (563-724). Two different concentrations (100 μM and 40 μM) were injected in the column. (e) Apo vs. cAMP SEC profiles of HCN4 (563-724) injected as a 100 μM solution. (f) SEC profile of apo HCN4 (579-707) injected as a 100 μM solution. Analytical SEC was preformed with a Superdex 75 10/30 column (GE Healthcare) at 4°C. Buffer contained 20 mM MES (pH 6.5), 100 mM KCl, 1 mM DTT with or without 1 mM cAMP.

The apo *vs*. holo HSQC comparison reveals dramatic changes in chemical shifts for the large majority of the eCBD residues (Figure 2b). A plot of the ppm variations *vs*. residue number indicates that cAMP binding has a pervasive effect on the eCBD region from the E' to the C-helix (Figure 2c). It is notable that cAMP results in major ppm changes (> average) not only in the cAMP-contact regions, which are nested within the β-subdomain (i.e. phosphate binding cassette, PBC, and the base binding region, BBR), but also in the α-subdomain, including helices that are both N- and C-terminal to the β-subdomain (Figure 2c,d). These observations point to the presence of cAMP-dependent structural changes that are not confined only to the B, C-helices, but extend to the E'-A segment as well, i.e. the N3A motif (Figure 2c,d). Unlike the N3A, the C'-D' region, which is part of the HCN IR tetramerization domain (i.e. helices A'-D'), displays only relatively minor, below average, chemical shift variations (Figure 2c). This finding is in agreement with the absence of major changes in self-association upon cAMP binding to the HCN4 eCBD, as expected due to the deletion of the A'-B' segment required for tetramerization [11, 21, 22]. In addition, analytical size exclusion chromatography (aSEC) confirms that the HCN4 eCBD remains predominantly monomeric even after cAMP binding (Figure 1d, e), as also shown by Chow et al. [11]. A minor shift towards larger elution volumes is observed upon cAMP-binding to the eCBD (Figure 1e), in agreement with a more compact structure for the cAMP-bound than the apo eCBD. In order to further probe the functional relevance of this cAMP-dependent structural change, we have extended our apo *vs*. holo comparative NMR analyses to a partial agonist, i.e. the cCMP cyclic nucleotide, which results in lower activation efficacies than cAMP [5, 53]. Therefore, cCMP is an excellent tool to establish

correlations between NMR observables of HCN4 fragments and functionally relevant electrophysiological measurements for full-length integral HCN4 channels.

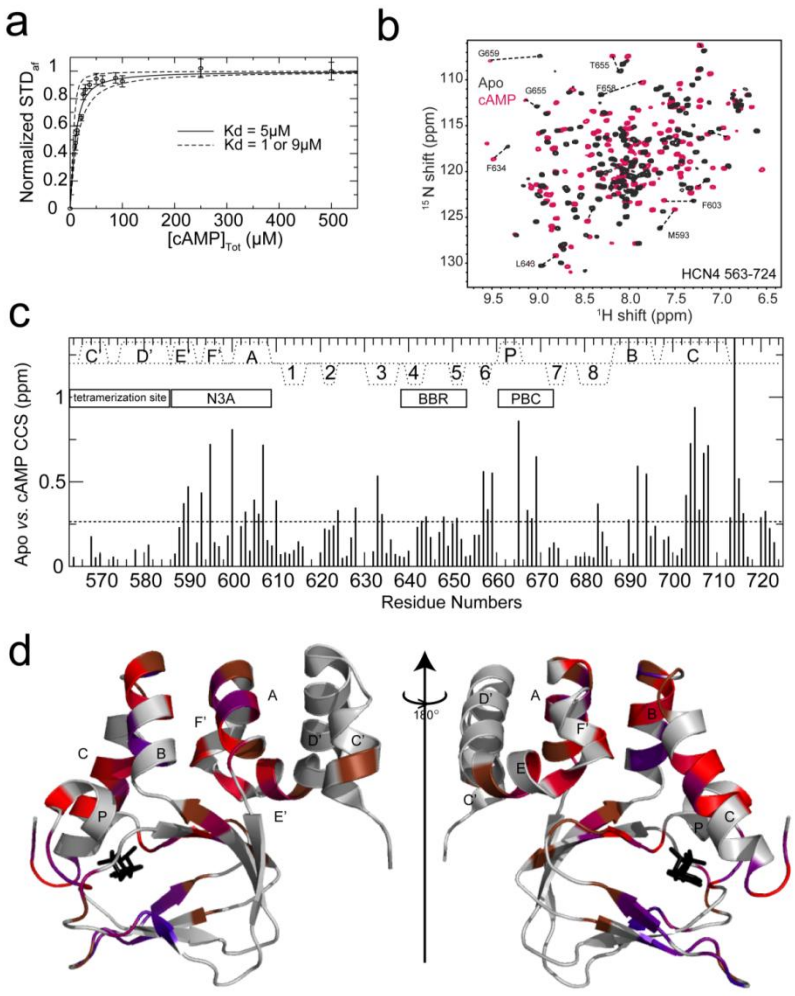

Figure 2: Binding of cAMP to human HCN4 (563-724) mapped by Saturation Transfer Difference (STD) NMR and Chemical Shift Perturbations. (a) Binding isotherm for the titration of cAMP into a 10 μM HCN4 (563-724) solution monitored through the STD amplification factor (STDaf) normalized to the plateau value and plotted versus the total cAMP concentration. The solid line represents the binding isotherm corresponding to a Kd value of 5 μM, while the dashed lines correspond to Kd values of 1 and 9 μM. (b) ^{1}H-^{15}N HSQC spectra of 0.1 mM HCN4 (563-724) acquired in the absence (black) and presence (red) of 2.5 mM excess cAMP. Representative peaks are labeled. (c) Compounded ^{1}H,^{15}N chemical shift (CCS) differences between apo and cAMP-bound HCN4 (563-724) plotted against the residue number. The secondary structure of cAMP-bound HCN4 is reported as dotted lines at the top of this panel. (d) Map of apo vs. holo CCS differences onto the structure of cAMP-bound HCN4 (563-724) (22). cAMP is shown as black sticks. Residue color code: 0.10 ppm ≤ CCS < 0.25 ppm is shown in brown, 0.25 ppm ≤ CCS < 0.50 ppm in purple and 0.50 ppm ≤ CCS in red.

The HCN4 eCBD Exists in a Dynamic Equilibrium of Functionally-Relevant Channel Inhibition-Competent and Incompetent States. The overlay of the HN-HSQC spectra of hHCN4 (563-724) in the absence and presence of saturating concentrations of cAMP or cCMP indicate that several residues far from the ligand contact sites (PBC, BBR, C-helix) exhibit a linear pattern (Figure 3a, b). The linearity of this pattern is consistent with the eCBD of HCN4 sampling a dynamic equilibrium between two-states that exchange fast in the NMR chemical shift time scale. This means that the observed chemical shifts are linearly weighted averages of the chemical shifts of the two exchanging states and as such they reflect the position of the equilibrium. In this respect, it is notable that the relative order of the peak positions (Apo < cCMP < cAMP) appears in agreement with the ranking of the respective V1/2 voltages measured through patch clamp electrophysiology for full-length HCN4 channels [53].

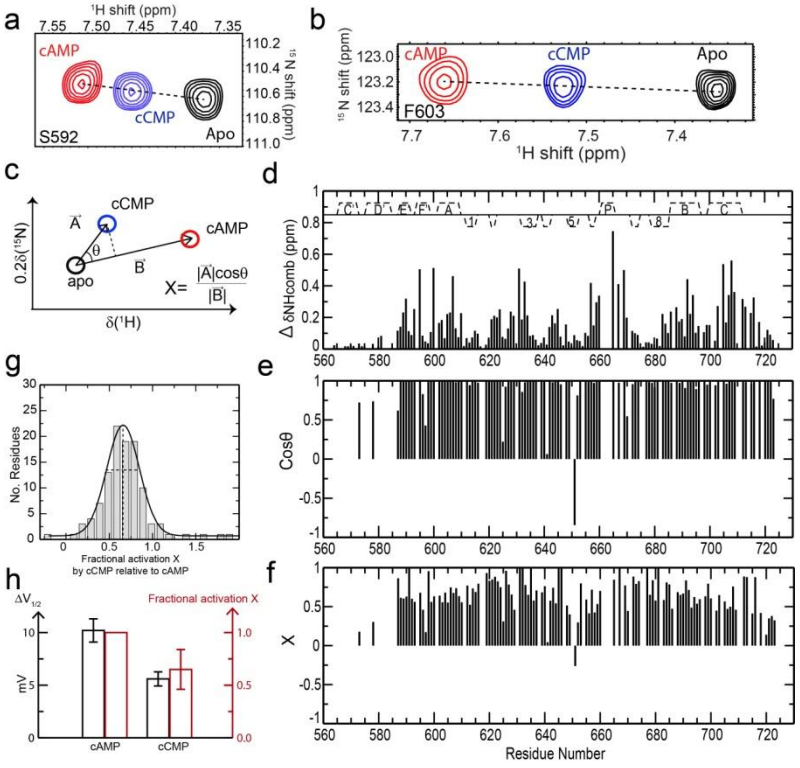

Figure 3: Fractional activation by cCMP partial agonist quantified through the comparative chemical shift analysis of apo vs. cCMP vs. cAMP HCN4 (563-724). **(a),(b)** Representative HSQC cross-peak for HCN4 (563-724) in the apo form and bound to excess cAMP or cCMP (2.5-5.0 mM). **(c)** Schematic illustration of the vectors utilized for the projection analysis of NMR chemical shifts. **(d)** Compounded chemical shift profile of cCMP relative to apo. **(e)** cos(θ) residue profile. The angle θ is defined in panel (c). **(f)** Residue-specific fractional shifts (X) toward activation caused by cCMP-binding. X is defined in panel (c). X was computed only for residues with an apo vs. cAMP compounded chemical shift greater than a 0.05 ppm.

(g) The distribution of fractional shifts toward activation from (f), computed using the CHEmical Shift Projection Analysis (CHESPA) (33). The experimental distribution was fitted to a Gaussian function. **(h)** Comparison between the NMR-based average relative % of active state in the cCMP-saturated HCN4 (563-724) sample and the $\Delta V_{1/2}$ voltage changes caused by cCMP binding to full length HCN4 channels measured through electrophysiology (53).

To further explore the relationship between the NMR peak positions and the HCN channel efficacies, we computed the distribution of relative fractional activations for cCMP relative to cAMP based on the NMR chemical shifts (X in Figure 3c,d and g) and we compared the average NMR-based activations to the ligand-induced change in V1/2 voltages (ΔV1/2 in Figure 3h). The X-distribution appears Gaussian and defines an average NMR-based fractional activation for cCMP, which is about half that observed for cAMP (Figure 3g). This cCMP *vs*. cAMP reduction is within error in agreement with the 50 % reduction in the ΔV1/2 for cCMP relative to cAMP, measured by electrophysiology of the full length HCN4 channel (Figure 3h). These observations suggest that the two states involved in the eCBD dynamic equilibrium sensed by NMR are inhibition-competent and incompetent, respectively, and that the cyclic nucleotide-dependent modulation of the position of the eCBD equilibrium is a key determinant of HCN channel gating. Hence, we have investigated further the structural changes caused by binding of cAMP to the eCBD.

cAMP-Binding to the Monomeric HCN4 eCBD Stabilizes the PBC helix and Distal Half of the C-Helix. To gain further insight into the structural changes caused by cAMP-binding to the HCN4 eCBD, we evaluated the secondary structure probabilities based on the secondary chemical shifts in both apo and holo forms (Figure 4a,b). The secondary structure profile of the cAMP-bound monomeric HCN4 eCBD matches well with that observed for the E'-C region of the

crystal structure solved for holo tetrameric HCN4 IR [21, 22] (Figure 4a). However, the C'-D' segment of the IR tetramerization domain does not adopt a clear secondary structure in the monomeric HCN4 (Figure 4a), whereas it is helical in the tetrameric form [21, 22]. The flexibility in the N-terminal region of the HCN eCBD monomer is confirmed by the presence of fast exchanging amides and by a pattern of decreasing HN NOE values detected when moving from the D' helix towards the N-terminus (Figure 4c). Furthermore, order parameter computations support a disordering of the A'-D' helices upon tetramer dissociation into monomers (Figure 4d).

The apo HCN4 eCBD exhibits a secondary structure profile that is remarkably similar to that of the holo form but for two notable exceptions, the PBC and the distal half of the C-helix (Figure 4b). In the absence of cAMP, the PBC helix between β6 and β7 is not observed (Figure 4b). Although some PBC residues could not be assigned due to line-broadening indicative of ms-μs dynamics, the lack of significant helical probabilities in the apo PBC is consistent with a destabilization of the PBC helix, which is clearly observed in the holo eCBD (Figure 4a). The destabilization of the apo PBC is also supported by the observation of fast exchanging amides (Figure 4a). The other major change in secondary structure caused by cAMP is in the C-helix region spanning residues 705-715, which is unstructured in the absence of cAMP (Figure 4b), but becomes structured in the presence of cAMP (Figure 4a). The cAMP-induced structuring of this segment is independently supported by a consistent increase in the HN NOE values upon cAMP-binding and by the cAMP-induced protection of several C-helix amides that are fast exchanging in the apo form (Figure 4c). Interestingly, no major changes in secondary structure are observed for the rest of the α-subdomain (Figure 4a,b), suggesting that the marked

cAMP-dependent HN chemical shift variations observed for helices E'-B (Figure 2c,d) arise primarily from changes in tertiary structure. This type of helical re-orientations is best probed through residual dipolar couplings (RDCs), which are highly sensitive to both hinge and on-axis rotations of helices [54, 55]. In order to facilitate the measurement of RDCs, we reduced the overlap in the helical spectral regions, which are typically less dispersed than β-sheets, by deleting the N- and C-terminal disordered residues (i.e. 563-578 and 708-724). These segments are unstructured in the apo eCBD as shown by both the secondary chemical shifts and the decreased HN NOE values (Figure 4b,c). Hence, removal of these regions is not expected to significantly perturb the rest of the apo HCN4 eCBD. This prediction is supported by the overall minimal chemical shift differences observed between the apo 563-724 and the apo 579-707 HCN4 constructs (Figure 4e). Furthermore, the analytical SEC elution profile confirms that apo HCN4 579-707 remains monomeric (Figure 1f). Thus, this construct is ideal for further NMR studies on the structure adopted by the apo eCBD monomer.

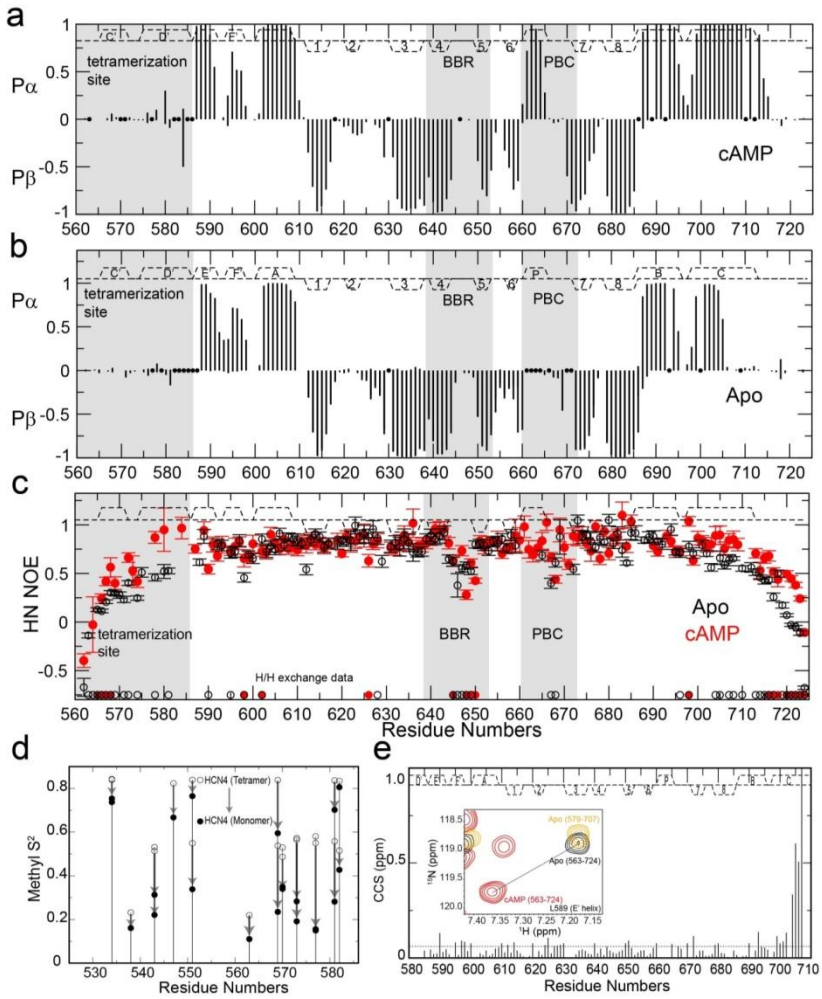

Figure 4: Secondary structure and ps-ns dynamic profile of apo and cAMP-bound human HCN4 (563-724). NMR chemical shift based secondary structure of HCN4 (563-724) in the presence of excess cAMP **(a)** and in the apo form **(b)**. Helical and strand probabilities are reported as positive and negative values, respectively. In panels (a) and (b), residues for which HN assignments are not available are flagged with a dot. **(c)** HN-NOE vs. residue plot for HCN4 (563-724) in the presence of excess cAMP (red) and in the apo form (black). The circles at the bottom of panel (c) denote the presence of fast H/H exchange as indicated by the observation of CLEANEX cross peaks in the apo form (empty circles) and in the presence of excess cAMP (red filled circles). **(d)** Changes in methyl order parameters (S^2) for the region spanning helices A'-D' as computed based on the HCN4 structure (chain A of PDB file 3OTF) either as an isolated monomer (filled circles) or assembled as a tetramer (open circles). Computations were executed through the "S2" software [81]. These computations don't consider the possible unfolding of the A'-D' helices upon tetramer dissociation and therefore it is possible that the experimental order parameters for the monomer are lower than those computed here. **(e)** Compounded chemical shift (CCS) differences between apo human HCN4 (579-707) and apo human HCN4 (563-724). Dashed lines outline the secondary structure as per the PDB entry 3OTF (22).

cAMP-Binding Causes a Shift in the α-Subdomain Tertiary Structure from an "N3A in/B-C out" to an "N3A out/B-C in" topology. A ten-structure model of apo HCN4 (579-707) was built (Figure 5a and Table 1) by CS-Rosetta using chemical shifts, homology restraints and RDCs (Figure 6a) [41-52]. Overall, the model is well converged, as supported by local RMSD values below 0.2 Å for most residues (Figure 6b). Selected regions exhibit RMSD > 0.2 Å, including the N- and

C-termini, the F' helix, the β2-3 and β4-5 loops as well as the PBC (Figure 6b). These local RMSD maxima match well with local minima in the HN NOE profile of apo HCN4 (579-707) (orange plot in Figure 6b; dotted ovals), suggesting that the increased RMSD values observed in these segments reflect genuinely enhanced ps-ns local dynamics rather than simply lack of experimental restraints.

To further validate the structural model of apo HCN4 (579-707) built by CS-Rosetta based on chemical shifts, evolutionary restraints and RDCs, we measured methyl-methyl NOEs in an ILV-methyl protonated but otherwise deuterated sample of apo HCN4 (579-707) (Figure 6c). Because of the extensive degree of deuteration, both spin-diffusion and transverse relaxation are reduced relative to fully protonated samples. This allows the measurement of NOEs for long-range distances (≤ 8 Å), which are sensitive to tertiary structure changes, such as those occurring in the HCN4 eCBD upon cAMP-binding. As shown in Figure 6c, the CS-Rosetta structures are in agreement with the experimental methyl-methyl NOEs, although the latter were not used as restraints in the structural refinement. Further CS-Rosetta iterations, with Me-Me and NH-involving NOEs explicitly included as restraints did not result in increased convergence nor in different models. In addition, the CS-Rosetta structures are supported by paramagnetic relaxation enhancement (PRE) measurements for an apo HCN4 (579-707) sample in which a spin-label was covalently linked to the endogenous Cys 586 (Figure 6d). PREs values quantified as oxidized *vs*. reduced intensity ratios (I_{ox}/I_{red}) are expected to vary linearly with distances when less than ~0.8 [40] and should exhibit a trend similar to that of the amide distances from Cys 586 predicted from the CS-Rosetta model. The PRE *vs*. distance linearity is apparent in Figure 6d, except for regions experiencing enhanced dynamics and greater

flexibility, such as the F' helix, the PBC and the C-terminus (Figure 6b,d). The local flexibility in these regions contributes to the localized deviations from the linear I_{ox}/I_{red} *vs*. distance trend. We conclude that the CS-Rosetta structures of the apo HCN4 (579-707) are supported not only by the measured chemical shifts and RDC values, but also by independent NOE and PRE measurements.

The structures of the apo HCN4 eCBD reveal several critical differences relative to its holo form (Figure 5b). In apo HCN4 the axis of the B-helix is tilted away from the PBC through a hinge rotation that moves the C-helix outward relative to the cAMP-binding site in the β-subdomain (i.e. 'B-C out' arrangement, Figure 5b). The movement of the C-helix away from the β-subdomain allows the E' and F'-helices to move closer to the PBC (i.e. 'N3A in' arrangement, Figure 5b) primarily through a rotation of the A-helix around its axis. Hence, the α-subdomain tertiary structure topologies in apo and holo HCN4 are reversed. The eCBD α-subdomain topology is "N3A in/B-C out" before cAMP binding, but switches to "N3A out/B-C in" after. This switch in α-subdomain topology does not significantly alter the relative orientation of the N3A helices E'-F'-A (Figure 5c), but changes the orientation of the β-subdomain relative to the N3A motif (Figure 5b,d).

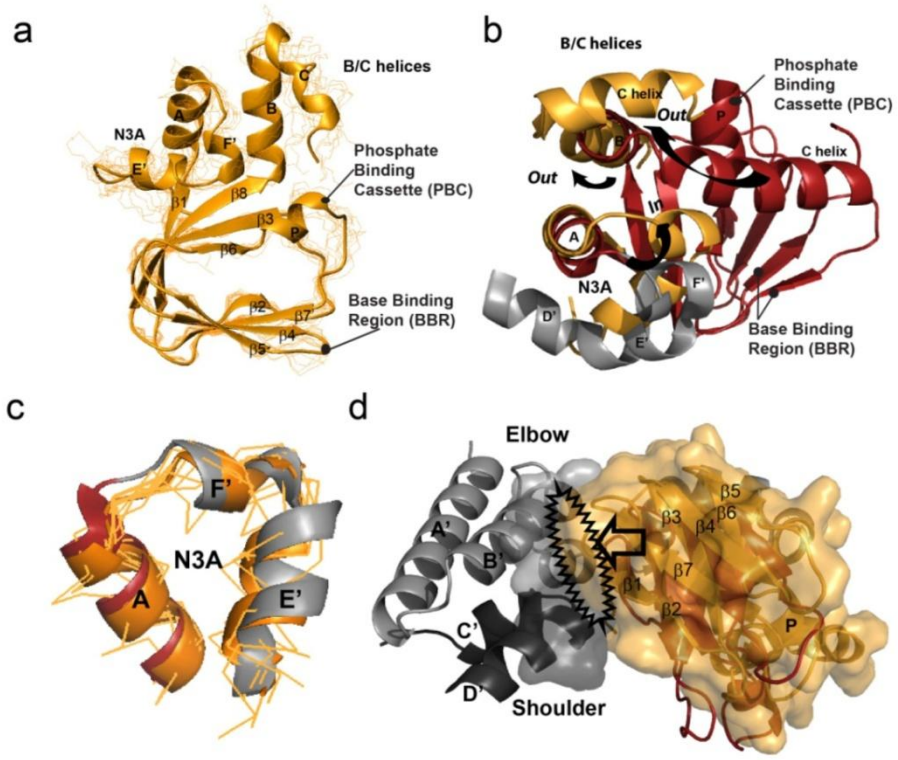

Figure 5: Proposed structural model for apo human HCN4 (579-707). (a) Overlay of ten representative structures of apo HCN4 (579-707) as refined through CS-Rosetta. The cartoon represents the average structure of the ensemble. (b) Apo (average, orange) vs. cAMP-bound (grey and red) CBD comparison. The holo HCN4 structure was obtained from the PDB entry 3OTF (22). Upon cAMP removal, the A helix rotates around its axis and slightly tilts moving the N3A motif closer to the PBC and the β-barrel ('N3A in' orientation). Unlike the N3A region, the B/C helices move away from the PBC upon removal of cAMP ('B/C out' orientation). (c) Apo (orange) vs. holo N3A overlay, revealing that the cAMP-dependent N3A movement occurs in first approximation as a rigid-body, i.e. the average relative orientation of the helices within the N3A motif does not change significantly upon cAMP-binding. The cartoon represents the average structure of the ensemble, similarly to panel (a). (d) "Hybrid" HCN4 hypothetical model arising from the overlay of the N3A motives from the active-state IR region (i.e. A'-β segment from the 'A' protomer of the PDB structure 3OTF; linker in light grey and CBD component in red) and from the inactive-state average structure (E'- β segment of apo HCN4 (579-707); orange). Helices C'-D' from an adjacent protomer are shown in dark grey to illustrate the 'elbow-shoulder' inter-molecular contacts that stabilize the tetramer. Surfaces are shown for the IR tetramerization domain residues that in the holo tetramer are in contact with the β-subdomain, and for the apo HCN4 structure. The arrow and black jagged oval highlight the site of steric clashes between the apo β-barrel and the IR tetramerization domain, as quantified in Table 2.

To explore how the cAMP-dependent β-subdomain / N3A reorientation affects the packing of the CBD within the tetramer, and in turn the propensity of the HCN4 IR to tetramerize, we superimposed the N3A motif of the apo HCN4 structure solved here to the N3A

region of the holo HCN4 tetramer (PDB code: 3OTF) [22] and analyzed how the packing of the β-subdomain is affected by the absence of cAMP (Figure 5d). In the presence of cAMP the β1-2 turn of the β-subdomain is in close contact with a surface defined by two contiguous helices, helix B' from the same protomer as the β-subdomain and helix D' from an adjacent protomer in the tetramer (Figure 5d). The B' and D' helices are respective parts of the 'elbow' and 'shoulder' contacts that stabilize the tetramer. In the absence of cAMP the β-subdomain moves towards the IR tetramerization domain, resulting in steric clashes between the β-barrel and the B'/D' elbow/shoulder surface (Figure 5d). The steric hindrance with the B'/D' helices leads to a marked surge in Van der Waals interaction energies, as summarized in Table 2, and hence to a destabilization of the tetramer. Overall, the apo HCN4 eCBD structure is not compatible with the tight packing imposed by tetramerization of the HCN IR. Upon cAMP-binding, the β-subdomain reorients removing the steric clashes with the IR tetramerization domain, thereby stabilizing the tetramer and explaining why cAMP causes a transition from tetramerization-incompetent to tetramerization-competent states.

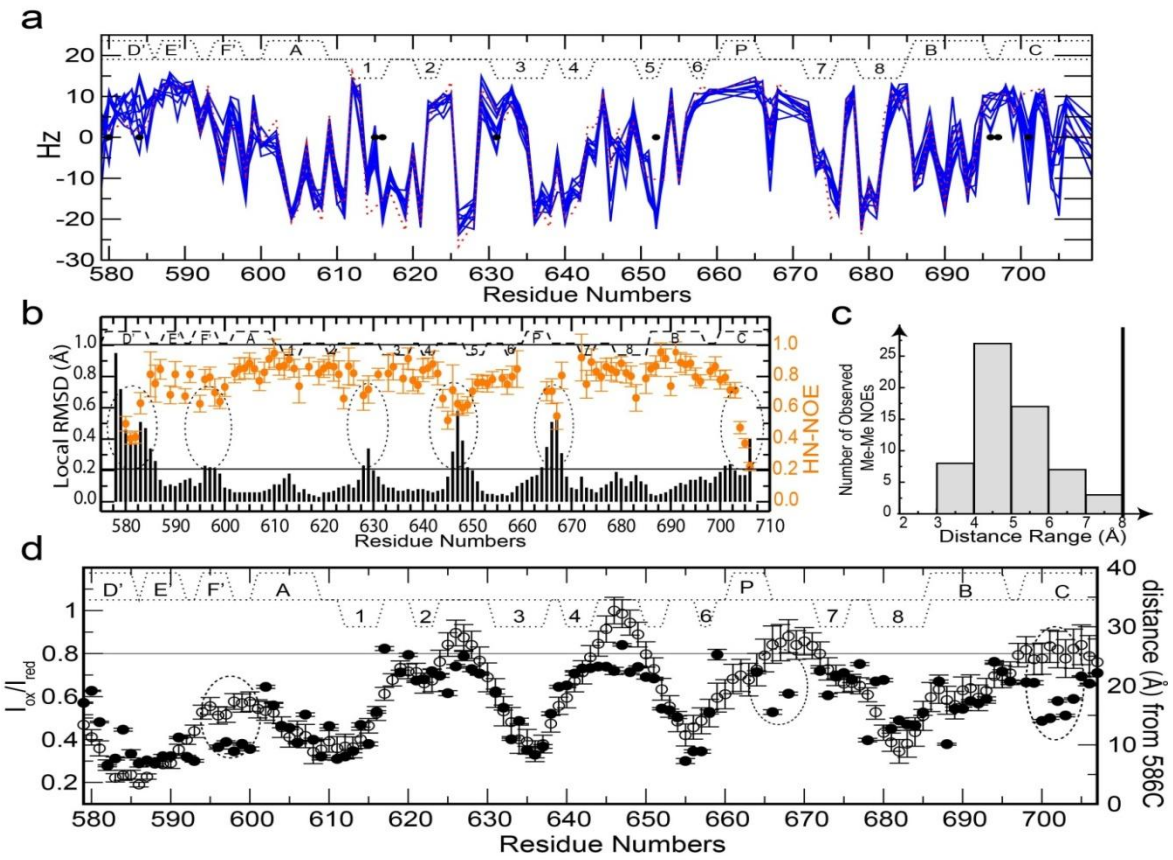

Figure 6: Validation of the structural model for apo human HCN4 (579-707). **(a)** Experimental vs. back-calculated RDC comparison for apo human HCN4 (579-707). The experimental backbone amide RDCs (red dashed line) show overall good agreement with the back-calculated RDCs (blue lines). Black dots represent residues for which cross-peaks were overlapping in the HSQC spectra. **(b)** Comparative analysis of the residue-specific local RMSD and HN-NOE profiles of apo human HCN4 (579-707). The dashed ovals highlight regions corresponding to local maxima and local minima in the RMSD and HN-NOE values, respectively. The secondary structure is reported as dashed lines. The local RMSD was computed using the structure bundle shown in Figure 5a. **(c)** Distance distribution for the Me-Me NOEs measured for apo HCN4 (579-707). Histogram showing the number of observed NOEs in apo HCN4 (579-707) for different distance ranges. Methyl-methyl distances have been calculated between methyl carbon atoms. All the observed NOEs correspond to distances less than 8 Å. **(d)** Paramagnetic Relaxation Enhancement (PRE) profile for apo human HCN4 (579-707) spin-labeled at Cys 586. The PREs were quantified in terms of relative HSQC intensity attenuations (I_{ox}/I_{red}; filled circles) and were compared to the average amide distances from the sulfur atom of Cys 586 computed based on the apo human HCN4 (579-707) structures (open circles). The I_{ox}/I_{red} ratios < 0.8 are expected to correlate linearly with distances, unless internal dynamics is present. Significant contributions from spin-labels at other Cys sites (i.e. Cys 662 and Cys 679) were ruled out as follows. Cys 679 is well structured (HN-NOE > 0.8, (a) and its side chain is inaccessible (solvent-accessible surface area, or SASA, in the apo structure is 0 $Å^2$). For Cys 662 the corresponding side chain SASA is 1 $Å^2$ and, although the HN NOE value for this residue is not available, the profile of amide distances from Cys 662 does not match the experimental intensity data. The dotted ovals indicate local deviations between the PRE ratios and the distances calculated based on the structures, possibly arising from the presence of structural dynamics.

Table 1: Structural Statistics of Apo HCN4 (579-707)	
Residues	131 [a]
Restraints	
Evolutionary restraints	4502
Total HN RDCs	115
Residues with good[b] TALOS+ prediction	94
Average RMSD to mean structure (Å)	
Backbone atoms (CING)	0.90 ± 0.19
Heavy atoms (CING)	1.43 ± 0.16
Ramachandran statistics (CING)	
Residues in most favored regions	89.6 %
Residues in allowed regions	10.4 %
Residues in generously allowed regions	0.0 %
Residue in disallowed regions	0.0 %

[a] 129 residues for HCN4 (579-707) and two additional residues from the restriction site (Asn and Ser). [b] "Good" TALOS+ predictions are defined as in reference [82].

Table 2: Potential Energies of Steric Contact Among Structural Elements of the Active-State and "Hybrid" Tetramer Structures of HCN4[a]

Structure	**αA'-αB'/β-core Intra-Monomer Contact Energy**[a] (kcal/mol)		**αC'-αD'/β-core Inter-Monomer Contact Energy**[a] (kcal/mol)		**Total IR Tetramerization Domain/β-core**[a] **Contact Energy** (kcal/mol)	
	αA Overlay [b]	N3A Overlay [b]	αA Overlay [b]	N3A Overlay [b]	αA Overlay [b]	N3A Overlay [b]
NMR #1	~ 10^1	~ 10^3	~ 10^2	-6.12	~ 10^2	~ 10^3
NMR #2	~ 10^9	> 10^9	~ 10^6	~ 10^3	~ 10^9	> 10^9
NMR #3	~ 10^6	~ 10^9	> 10^9	~ 10^5	> 10^9	~ 10^9
NMR #4	~ 10^8	~ 10^7	~ 10^4	~ 10^3	~ 10^8	~ 10^7
NMR #5	~ 10^8	> 10^9	~ 10^9	~ 10^2	~ 10^9	> 10^9
NMR #6	-7.49	-1.93	~ 10^7	-2.13 (~ 10^7) [c]	~ 10^7	-4.06 (~ 10^7) [c]
NMR #7	> 10^9	> 10^9	> 10^9	~ 10^8	> 10^9	> 10^9
NMR #8	> 10^9	~ 10^9	-7.01	~ 10^3	> 10^9	~ 10^9
NMR #9	~ 10^3	~ 10^9	~ 10^9	-12.05	~ 10^9	~ 10^9
NMR #10	~ 10^4	> 10^9	~ 10^4	~ 10^4	~ 10^4	> 10^9
NMR Median Average	~ 10^8	~ 10^9	~ 10^7	~ 10^3	~ 10^9	~ 10^9
Active-State Tetramer [d]	-16.83		-11.84		-28.67	

[a] The energies of steric contact between structural elements "X" and "Y" were computed from the Van der Waals (VDW) energies using NAMD as follows: Contact E (X *vs*. Y) = VDW (X and Y together) – VDW (X alone) – VDW (Y alone). The CHARMM 27 force field was used to calculate the VDW energies. [b] For each NMR-derived "hybrid" tetramer, energy values for two structures are listed in each row: a structure consisting of the αA'-αF' segment of the active-state structure (3OTF), and the αA-αC segment of the respective NMR structure, grafted together *via* αA helix backbone overlay (first value); and a structure consisting of the αA'-αD' segment of the active-state structure (3OTF), and the αE'-αC segment of the respective NMR structure, grafted together *via* αE'-αA region (N3A) backbone overlay (second value). [c] The number in parenthesis is the contact energy arising from the inter-molecular αB/C *vs.* b-core clash. [d] Tetramer derived from structure "3OTF" obtained from the RCSB Protein Data Bank.

4.5 Discussion

Our data support a model for the intracellular region (IR) of HCN4 in which the C-linker region spanning the IR tetramerization domain, i.e. helices A'-D', remains intrinsically unstructured or only partially structured when the IR is monomeric (Figure 7a-d), whereas the rest of the IR, including the CBD, exists in a dynamic equilibrium between auto-inhibited and active states (Figure 7a,b). In both states the internal structures of the N3A and β-barrel remain largely conserved, but they are oriented differently in relation to each other. In the auto-inhibited state the N3A motif is in close proximity to the β-barrel ('N3A in', Figure 7a) because of an outward movement of the C-terminal B-C helices ('B/C out', Figure 7a), which would otherwise clash with the N3A in arrangement. In the active state, the CBD switches to a swapped topology, where the N3A adopts an 'out' orientation distal from the β-subdomain because the B/C helices are tilted in an 'in' arrangement (Figure 7b). In the absence of cAMP, the auto-inhibited *vs*. active equilibrium is shifted toward the former state, whereas the latter has greater affinity for cAMP and is therefore favored when the cyclic nucleotide is available to bind.

A key determinant of the selectivity of cAMP for the active state is its ability to stabilize the C-terminal half of the C-helix, which serves as a lid for capping the adenine base (Figure 7c) [1, 3, 56]. The active *vs*. inactive selectivity of cAMP results in the coupling between the cAMP-binding and the conformational equilibria of the eCBD, which is described by the allosteric thermodynamic cycle depicted in Figure 7a-d. In all four states of the cycle for the monomeric IR, the C-linker region spanning the IR tetramerization domain remains largely

unstructured, regardless of cAMP availability or the position of the auto-inhibitory equilibrium (Figure 7a-d).

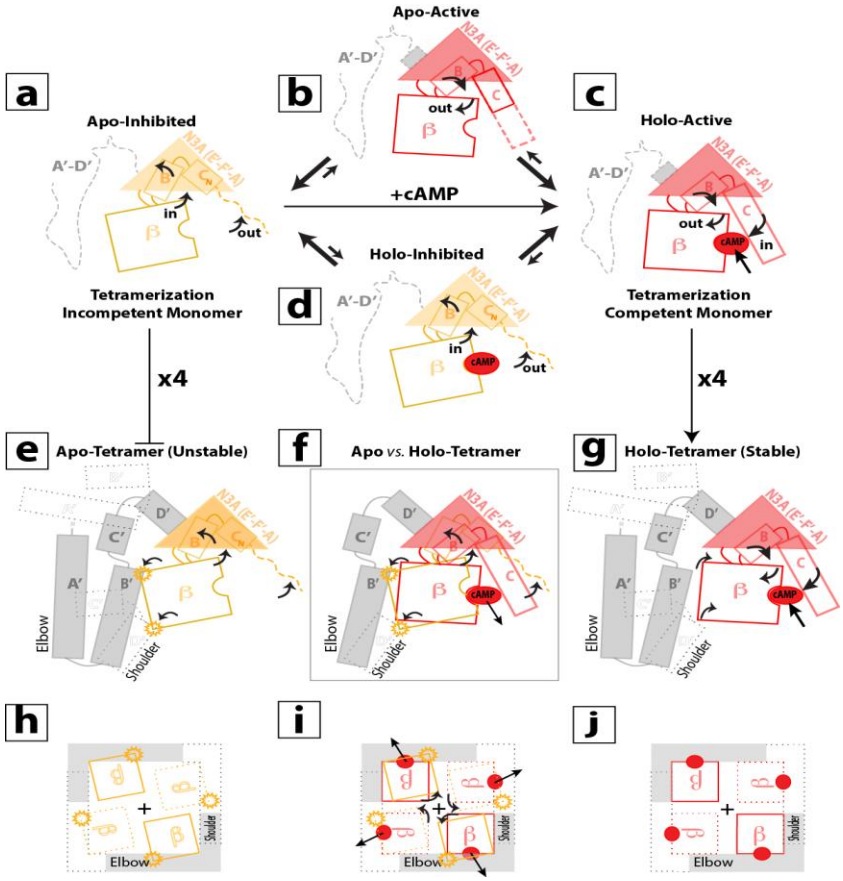

Figure 7: Proposed model for auto-inhibition of HCN4 by the intracellular region (IR), spanning the IR tetramerization domain (i.e. helices A'-D'), shown in grey, the N3A and the remaining part of the CBD, both shown in either orange (apo) or red (holo). The N3A motif (triangle) is composed of helices E'-F'-A, which are N-terminal to the β-subdomain of the CBD. The CBD includes also helices B-C, which are C-terminal to the β-subdomain and function as a lid for cAMP. The N3A orientation is kept constant in all the panels. Dashed lines denote unfolded or partially unfolded segments. (a-d) Four-state thermodynamic cycle for the cAMP-dependent allostery of the monomeric HCN4 IR, resulting from the coupling of the cAMP-binding equilibrium (i.e. apo vs. holo) and the conformational change equilibrium (i.e. inhibited vs. active). (e-f) Models for the tetrameric HCN4 IR. Dotted lines indicate helices from distinct but adjacent protomers within the tetramer. Tetramerization promotes folding of helices A'-D'. However, the apo-tetramer is unstable due to steric clashes between the β-subdomain and the IR tetramerization domain, which are highlighted as yellow stars. The allosteric conformational transition driven by cAMP-binding changes the relative orientation of the N3A and β-subdomain, eliminating the steric clashes that destabilize the apo-tetramer, as shown in panel (g). Panel (f) illustrates the apo-tetramer vs. holo-tetramer comparison. (h-j) Schemes of the apo (h), holo (j) and apo vs. holo (i) HCN4 intracellular region tetramer viewed parallel to the four-fold axis, denoted by the "+" sign in the center of each tetramer. Similarly to panels e-g, yellow stars indicate steric clashes and red filled ovals represent cAMP molecules.

The four helices of the C-linker composing the IR tetramerization domain, i.e. A'-D', are stabilized upon tetramer formation by 'elbow-shoulder' swapped contacts between the A'-B' motif of one protomer and the C'-D' helices of the adjacent subunit (Figure 7e-g) [1, 21, 22]. The stabilized D' helix in the tetramer recruits and orients the contiguous N3A motif with respect to the IR tetramerization domain [1, 21, 22, 25]. However, in the absence of cAMP the 'N3A in/B-C out' tertiary structure of the apo eCBD leads to a steric clash between the β-subdomain and the 'elbow-shoulder' surface defined by helix B' of the same protomer and helix D' of the adjacent protomer (Figure 7e,h), making an apo-tetramer unstable. By switching the 'N3A in/B-C out' to the 'N3A out/B-C in' conformation, cAMP binding effectively removes the steric hindrance that destabilizes the apo-tetramer (Figure 7f,i), resulting in a stable holo-tetramer (Figure 7g,j). This simple model (Figure 7) explains why apo monomeric IR is tetramerization-incompetent (Figure 7a,e,h) and why tetramerization-competence is restored by cAMP (Figure 7c,g,j). Because tetramerization of the HCN2 and HCN4 IR in solution appears to reflect a process promoted by cAMP in the full-length channel [1, 11, 21, 57], we propose that the scheme in Figure 7 represents a possible molecular mechanism for auto-inhibition of opening by the IR and its relaxation by cAMP in the full-length HCN channel.

The proposed mechanism (Figure 7) explains several other previously reported observations on the activation of HCN truncation mutants [23]. For example, the scheme of Figure 7 rationalizes why deletion of the C-terminal C-helix results in an HCN2 channel that remains auto-inhibited both in the absence and presence of cAMP [23]. The C-helix truncation does not affect significantly the apo form, where the C-helix is already partially unstructured and in an 'out' orientation (Figure 7a). However, the C-helix deletion removes the lid for cAMP

and, thus, the 'N3A in/B-C out' to 'N3A out/B-C in' conformational switch does not take place when cAMP binds. Furthermore, the mechanism of Figure 7 explains why the deletion of the whole CBD activates the HCN channels, mimicking the action of cAMP binding to the wt HCN [23]. In the absence of the CBD, the steric clashes that destabilize the apo-tetramer (Figure 7e,h) are effectively eliminated, allowing tetramerization, and presumably facilitation of opening in the full-length channel, to occur even in the absence of cAMP.

The model of Figure 7 is also supported by other independent observations. For instance, the structure of the HCN2 IR solved in the absence of cAMP reveals a tetramer in which both the N3A and the β-barrel preserve the same orientation relative to the IR tetramerization domain (TD) as observed in the cAMP-bound tetramer [25]. This observation has two key implications. The first is that, as posited in the proposed model (Figure 7e-j), the positioning of the N3A motif relative to the TD is dictated primarily by the tetramerization, rather than by cAMP availability. The second is that, once the N3A is positioned relative to the TD, the 'in' orientation of the β-barrel is incompatible with the tetramer and, if the tetramer is imposed through the use of high concentrations, as in the case of crystallization, the β-barrel is forced to shift to the 'out' orientation to relieve the steric clashes with the TD and fit in the tightly packed tetramer, as observed [1, 25].

The tetramerization-induced shift of the eCBD from the 'N3A in/B-C out' to the 'N3A out/B-C in' state, which exhibits higher affinity for cAMP, is also independently confirmed by experiments showing that the tetrameric forms of the HCN2 and HCN4 IR bind cAMP with affinities significantly higher than those measured for the monomeric IR [11]. Therefore, cAMP-binding and tetramerization appear mutually coupled and an enhancement in one

promotes the other. This mutual coupling may explain the differences in cAMP-sensitivities observed for different HCN isoforms [21]. Overall, the currently available data support the mutual exclusivity between the apo eCBD 'N3A in/B-C out' topology and the formation of a tightly packed HCN tetramer. Nevertheless, it should be noted that the apo eCBD 'N3A in/B-C out' structure might be compatible with oligomeric forms of the IR other than tetramers.

The model of Figure 7 is consistent with the presence of dimers (Figure 8). This is because not only apo-monomers, but also apo-dimers may release the steric hindrance identified in the apo-tetramer (Figure 7e,h) due to the intrinsic flexibility of the A'-D' region (Figure 7a). In the scheme of Figure 7e,h, the presence of steric clashes between the β-subdomain and the B'/D' elbow/shoulder surface of the TD requires the simultaneous structuring through self-association of both the A'B' and the C'D' helical pairs belonging to the same protomer as the β-barrel causing the hindrance. If either one of these A'B' or C'D' pairs is not fully structured, the orientation of the N3A motif relative to the TD is not fully defined, given the intrinsic dynamics observed for the TD region in the absence of self-association (Figure 8a). The steric clashes generated by the β-subdomain can then be effectively reduced by a rigid-body movement of the N3A and β-subdomain away from the TD, without the need of a 'N3A in/B-C out' to 'N3A out/B-C in' shift of the eCBD. This is the case for HCN dimers (Figure 8), in which the C'D' of one protomer is not stabilized by the A'B' of an adjacent protomer or vice versa. Hence, in the dimer, unlike in the tetramer, the A'B' and C'D' pairs cannot both be simultaneously stabilized though self-association and thus steric hindrance is released even without cAMP (Figure 8). We conclude that the model of Figure 7 is fully consistent with the

apo HCN IR existing not only as a monomer, but also as a dimer of dimers (Figure 8), as previously proposed based on electrophysiological measurements [57, 58].

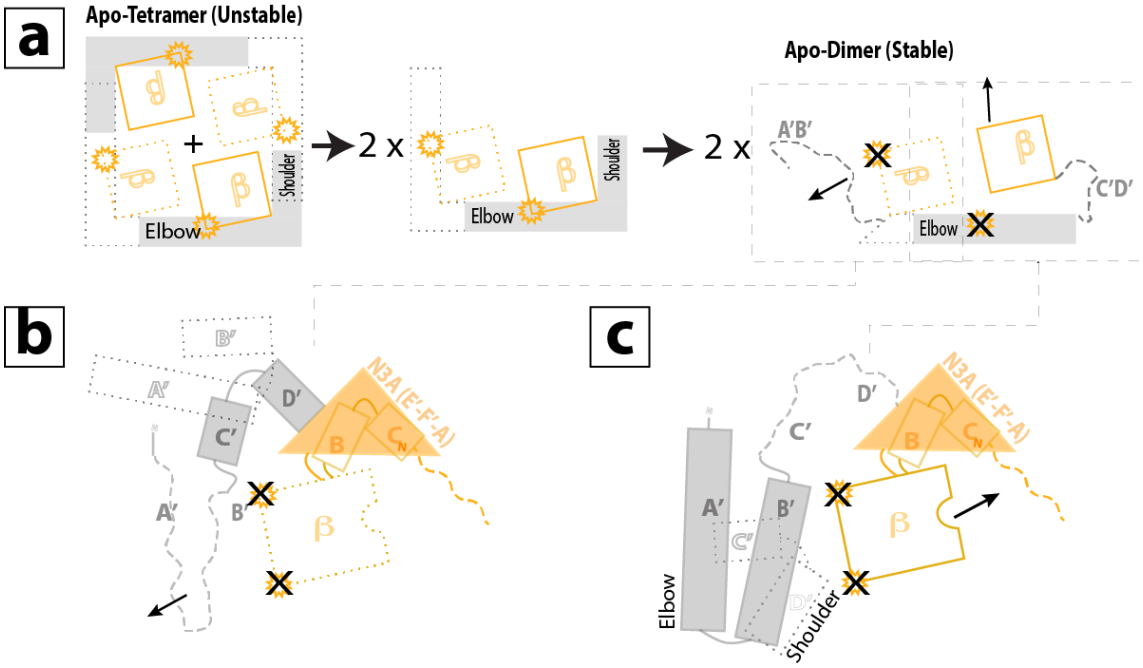

Figure 8: Proposed Models for Apo HCN Dimer of Dimers. Scheme illustrating why in the apo HCN dimer the eCBD does not necessarily lead to steric clashes, unlike in the apo tetramer (Figure 7e,h). The color codes are as in Figure 7. As in Figure 7, dashed lines denote regions that are only partially structured or unstructured, while dotted rectangles indicate helices belonging to an adjacent protomer. (a) Step-wise dissociation of the unstable apo-tetramer into dimers, in which the structuring effect of self-association is preserved for only a single elbow-shoulder interface per dimer. The increased linker flexibility in the dimer relative to the tetramer allows the β-subdomain of the CBD to move and relax the steric clashes (stars with "X"), as shown in panels, (b) and (c), which correspond to the two different protomers within the dimer.

Our data also suggest a possible mechanism for the action of cCMP, which has been shown to act as a partial agonist using electrophysiological methods [1, 53]. Partial agonism could arise either from a different conformational change occurring in response to the partial agonist or from a structural change that is similar to the alteration produced by the endogenous allosteric effector, but corresponds to a reduced shift in the position of the auto-inhibitory equilibrium [59]. Our results support the second hypothesis, whereby cCMP exhibits a lower tetramerization-competent *vs*. tetramerization-incompetent state selectivity than cAMP.

Consequently, the tetramerization- competent state is more stable when bound to cAMP than cCMP, resulting in a reduced equilibrium shift upon cCMP binding to the CBD.

Last but not least, the model of Figure 7 reveals that the HCN eCBD exhibits similarities with the allosteric conformational switch previously observed for PKA [60-69], and distinct differences from EPAC, which is another pivotal eukaryotic cAMP receptor with a structurally homologous α/β-CBD [70-75]. In the EPAC CBD, the cAMP-dependent structural changes are mainly confined to the helix C-terminal to the β-subdomain [34]. Upon cAMP-binding, this helix tilts toward the PBC and during the hinge rotation the helix partially unfolds, unlike what observed in HCN. In addition, unlike HCN, in EPAC no major cAMP-dependent re-arrangements are observed for the N3A motif, whereas a clear 'N3A in/B-C out' to 'N3A out/B-C in' shift was reported for both CBDs of the regulatory subunit of PKA [24, 60-75], similarly to bacterial CNG channels [76]. In this respect, the HCN CBD resembles more closely that of PKA rather than that of EPAC. However, it is likely that differences may still exist between the CBDs of PKA and HCN. For instance, for one of the PKA CBDs the apo pre-equilibrium does not appear to be as highly skewed toward the inactive state as in the CBD of the apo HCN IR [35], explaining why the regulatory subunit of PKA, unlike HCN [11], binds cAMP with a low ~nM affinity. The differences in binding and allosteric properties among different eukaryotic CBDs will facilitate the selective targeting of CBDs as required for therapeutic purposes [77-80].

4.6 Acknowledgements

We thank Professors Anna Moroni (University of Milan) and Susan S. Taylor (UCSD), as well as K. Moleschi and Dr. R. Giri for helpful discussions. This project was funded by a grant to G.M. from the Canadian Institutes of Health Research (CIHR).

4.7 References

1. Zagotta, W.N., Olivier, N.B., Black, K.D., Young, E.C., Olson, R., and Gouaux, E. (2003) Structural basis for modulation and agonist specificity of HCN pacemaker channels. Nature. 425, 200-205
2. Robinson, R.B., and Siegelbaum, S.A. (2003) Hyperpolarization-activated cation currents: from molecules to physiological function. Annu.Rev.Physiol. 65, 453-480
3. Trudeau, M.C., and Zagotta, W.N. (2003) Calcium/calmodulin modulation of olfactory and rod cyclic nucleotide-gated ion channels. J.Biol.Chem. 278, 18705-18708
4. Kaupp, U.B., and Seifert, R. (2002) Cyclic nucleotide-gated ion channels. Physiol.Rev. 82, 769-824
5. DiFrancesco, D., and Tortora, P. (1991) Direct activation of cardiac pacemaker channels by intracellular cyclic AMP. Nature. 351, 145-147
6. Kusch, J., Thon, S., Schulz, E., Biskup, C., Nache, V., Zimmer, T., Seifert, R., Schwede, F., and Benndorf, K. (2011) How subunits cooperate in cAMP-induced activation of homotetrameric HCN2 channels. Nat.Chem.Biol. 8, 162-169
7. Zagotta, W.N., and Siegelbaum, S.A. (1996) Structure and function of cyclic nucleotide-gated channels. Annu.Rev.Neurosci. 19, 235-263
8. Craven, K.B., and Zagotta, W.N. (2006) CNG and HCN channels: two peas, one pod. Annu.Rev.Physiol. 68, 375-401
9. Flynn, G.E., Johnson, J.P.,Jr, and Zagotta, W.N. (2001) Cyclic nucleotide-gated channels: shedding light on the opening of a channel pore. Nat.Rev.Neurosci. 2, 643-651
10. Johnson, J.P.,Jr, and Zagotta, W.N. (2005) The carboxyl-terminal region of cyclic nucleotide-modulated channels is a gating ring, not a permeation path. Proc.Natl.Acad.Sci.U.S.A. 102, 2742-2747
11. Chow, S.S., Van Petegem, F., and Accili, E.A. (2012) Energetics of cyclic AMP binding to HCN channel C terminus reveal negative cooperativity. J.Biol.Chem. 287, 600-606

12. Hegle, A.P., Nazzari, H., Roth, A., Angoli, D., and Accili, E.A. (2010) Evolutionary emergence of N-glycosylation as a variable promoter of HCN channel surface expression. Am.J.Physiol.Cell.Physiol. 298, C1066-76

13. Jackson, H.A., Hegle, A., Nazzari, H., Jegla, T., and Accili, E.A. (2012) Asymmetric divergence in structure and function of HCN channel duplicates in Ciona intestinalis. PLoS One. 7, e47590

14. Jackson, H.A., Marshall, C.R., and Accili, E.A. (2007) Evolution and structural diversification of hyperpolarization-activated cyclic nucleotide-gated channel genes. Physiol.Genomics. 29, 231-245

15. Macri, V., and Accili, E.A. (2004) Structural elements of instantaneous and slow gating in hyperpolarization-activated cyclic nucleotide-gated channels. J.Biol.Chem. 279, 16832-16846

16. Macri, V., Angoli, D., and Accili, E.A. (2012) Architecture of the HCN selectivity filter and control of cation permeation. Sci.Rep. 2, 894

17. Macri, V., Nazzari, H., McDonald, E., and Accili, E.A. (2009) Alanine scanning of the S6 segment reveals a unique and cAMP-sensitive association between the pore and voltage-dependent opening in HCN channels. J.Biol.Chem. 284, 15659-15667

18. Peters, C.J., Chow, S.S., Angoli, D., Nazzari, H., Cayabyab, F.S., Morshedian, A., and Accili, E.A. (2009) In situ co-distribution and functional interactions of SAP97 with sinoatrial isoforms of HCN channels. J.Mol.Cell.Cardiol. 46, 636-643

19. Qu, Y., Whitaker, G.M., Hove-Madsen, L., Tibbits, G.F., and Accili, E.A. (2008) Hyperpolarization-activated cyclic nucleotide-modulated 'HCN' channels confer regular and faster rhythmicity to beating mouse embryonic stem cells. J.Physiol. 586, 701-716

20. Whitaker, G.M., Angoli, D., Nazzari, H., Shigemoto, R., and Accili, E.A. (2007) HCN2 and HCN4 isoforms self-assemble and co-assemble with equal preference to form functional pacemaker channels. J.Biol.Chem. 282, 22900-22909

21. Lolicato, M., Nardini, M., Gazzarrini, S., Moller, S., Bertinetti, D., Herberg, F.W., Bolognesi, M., Martin, H., Fasolini, M., Bertrand, J.A., Arrigoni, C., Thiel, G., and Moroni, A. (2011) Tetramerization dynamics of C-terminal domain underlies isoform-specific cAMP gating in hyperpolarization-activated cyclic nucleotide-gated channels. J.Biol.Chem. 286, 44811-44820

22. Xu, X., Vysotskaya, Z.V., Liu, Q., and Zhou, L. (2010) Structural basis for the cAMP-dependent gating in the human HCN4 channel. J.Biol.Chem. 285, 37082-37091

23. Wainger, B.J., DeGennaro, M., Santoro, B., Siegelbaum, S.A., and Tibbs, G.R. (2001) Molecular mechanism of cAMP modulation of HCN pacemaker channels. Nature. 411, 805-810

24. Kim, C., Cheng, C.Y., Saldanha, S.A., and Taylor, S.S. (2007) PKA-I holoenzyme structure reveals a mechanism for cAMP-dependent activation. Cell. 130, 1032-1043

25. Taraska, J.W., Puljung, M.C., Olivier, N.B., Flynn, G.E., and Zagotta, W.N. (2009) Mapping the structure and conformational movements of proteins with transition metal ion FRET. Nat.Methods. 6, 532-537

26. Badireddy, S., Yunfeng, G., Ritchie, M., Akamine, P., Wu, J., Kim, C.W., Taylor, S.S., Qingsong, L., Swaminathan, K., and Anand, G.S. (2011) Cyclic AMP analog blocks kinase activation by stabilizing inactive conformation: conformational selection highlights a new concept in allosteric inhibitor design. Mol.Cell.Proteomics. 10, M110.004390

27. Kim, J.J., Casteel, D.E., Huang, G., Kwon, T.H., Ren, R.K., Zwart, P., Headd, J.J., Brown, N.G., Chow, D.C., Palzkill, T., and Kim, C. (2011) Co-crystal structures of PKG Ibeta (92-227) with cGMP and cAMP reveal the molecular details of cyclic-nucleotide binding. PLoS One. 6, e18413

28. Delaglio, F., Grzesiek, S., Vuister, G.W., Zhu, G., Pfeifer, J., and Bax, A. (1995) Nmrpipe - a Multidimensional Spectral Processing System Based on Unix Pipes. J.Biomol.NMR. 6, 277-293

29. T. D. Goddard and D. G. Kneller University of California, San Francisco SPARKY3,

30. Sattler, M., Schleucher, J., and Griesinger, C. (1999) Heteronuclear multidimensional NMR experiments for the structure determination of proteins in solution employing pulsed field gradients. Prog Nucl Magn Reson Spectrosc. 34, 93-158

31. Eghbalnia, H., Bahrami, A., Wang, L., Assadi, A., and Markley, J. (2005) Probabilistic identification of spin systems and their assignments including coil-helix inference as output (PISTACHIO). J.Biomol.NMR 32, 219-233

32. Mazhab-Jafari, M.T., Das, R., Fotheringham, S.A., SilDas, S., Chowdhury, S., and Melacini, G. (2007) Understanding cAMP-dependent allostery by NMR spectroscopy: comparative analysis of the EPAC1 cAMP-binding domain in its apo and cAMP-bound states. J.Am.Chem.Soc. 129, 14482-14492

33. Selvaratnam, R., Vanschouwen, B., Fogolari, F., Mazhab-Jafari, M.T., Das, R., and Melacini, G. (2012) The Projection Analysis of NMR Chemical Shifts Reveals Extended EPAC Autoinhibition Determinants. Biophys.J. 102, 630-639

34. Selvaratnam, R., Chowdhury, S., VanSchouwen, B., and Melacini, G. (2011) Mapping allostery through the covariance analysis of NMR chemical shifts. Proc.Natl.Acad.Sci.U.S.A. 108, 6133-6138

35. Akimoto, M., Selvaratnam, R., McNicholl, E.T., Verma, G., Taylor, S.S., and Melacini, G. (2013) Signaling through dynamic linkers as revealed by PKA. Proc.Natl.Acad.Sci.U.S.A. 110, 14231-14236

36. Pawley, N.H., Koide, S., and Nicholson, L.K. (2002) Backbone dynamics and thermodynamics of Borrelia outer surface protein A. J.Mol.Biol. 324, 991-1002

37. Cordier, F., Dingley, A.J., and Grzesiek, S. (1999) A doublet-separated sensitivity-enhanced HSQC for the determination of scalar and dipolar one-bond J-couplings. J.Biomol.NMR. 13, 175-180

38. Hansen, M.R., Mueller, L., and Pardi, A. (1998) Tunable alignment of macromolecules by filamentous phage yields dipolar coupling interactions. Nat.Struct.Biol. 5, 1065-1074

39. Tugarinov, V., and Kay, L.E. (2005) Methyl groups as probes of structure and dynamics in NMR studies of high-molecular-weight proteins. Chembiochem. 6, 1567-1577

40. Battiste, J.L., and Wagner, G. (2000) Utilization of site-directed spin labeling and high-resolution heteronuclear nuclear magnetic resonance for global fold determination of large proteins with limited nuclear overhauser effect data. Biochemistry. 39, 5355-5365

41. Thompson, J., and Baker, D. (2011) Incorporation of evolutionary information into Rosetta comparative modeling. Proteins. 79, 2380–2388

42. Vernon, R., Shen, Y., Baker, D., and Lange, O.F. (2013) Improved chemical shift based fragment selection for CS-Rosetta using Rosetta3 fragment picker. J.Biomol.NMR. 57, 117-127

43. van der Schot, G., Zhang, Z., Vernon, R., Shen, Y., Vranken, W.F., Baker, D., Bonvin, A.M., and Lange, O.F. (2013) Improving 3D structure prediction from chemical shift data. J.Biomol.NMR. 57, 27-35

44. Lange, O.F., Rossi, P., Sgourakis, N.G., Song, Y., Lee, H.W., Aramini, J.M., Ertekin, A., Xiao, R., Acton, T.B., Montelione, G.T., and Baker, D. (2012) Determination of solution structures of proteins up to 40 kDa using CS-Rosetta with sparse NMR data from deuterated samples. Proc.Natl.Acad.Sci.U.S.A. 109, 10873-10878

45. Lange, O.F., and Baker, D. (2012) Resolution-adapted recombination of structural features significantly improves sampling in restraint-guided structure calculation. Proteins. 80, 884-895

46. Bouvignies, G., Vallurupalli, P., Hansen, D.F., Correia, B.E., Lange, O., Bah, A., Vernon, R.M., Dahlquist, F.W., Baker, D., and Kay, L.E. (2011) Solution structure of a minor and transiently formed state of a T4 lysozyme mutant. Nature. 477, 111-114

47. Warner, L.R., Varga, K., Lange, O.F., Baker, S.L., Baker, D., Sousa, M.C., and Pardi, A. (2011) Structure of the BamC two-domain protein obtained by Rosetta with a limited NMR data set. J.Mol.Biol. 411, 83-95

48. Sgourakis, N.G., Lange, O.F., DiMaio, F., Andre, I., Fitzkee, N.C., Rossi, P., Montelione, G.T., Bax, A., and Baker, D. (2011) Determination of the structures of symmetric protein oligomers from NMR chemical shifts and residual dipolar couplings. J.Am.Chem.Soc. 133, 6288-6298

49. Leaver-Fay, A., Tyka, M., Lewis, S.M., Lange, O.F., Thompson, J., Jacak, R., Kaufman, K., Renfrew, P.D., Smith, C.A., Sheffler, W., Davis, I.W., Cooper, S., Treuille, A., Mandell, D.J., Richter, F., Ban, Y.E., Fleishman, S.J., Corn, J.E., Kim, D.E., Lyskov, S., Berrondo, M., Mentzer, S., Popovic, Z., Havranek, J.J., Karanicolas, J., Das, R., Meiler, J., Kortemme, T., Gray, J.J., Kuhlman, B., Baker, D., and Bradley, P. (2011) ROSETTA3: an object-oriented software suite for the simulation and design of macromolecules. Methods Enzymol. 487, 545-574

50. Raman, S., Lange, O.F., Rossi, P., Tyka, M., Wang, X., Aramini, J., Liu, G., Ramelot, T.A., Eletsky, A., Szyperski, T., Kennedy, M.A., Prestegard, J., Montelione, G.T., and Baker, D. (2010) NMR structure determination for larger proteins using backbone-only data. Science. 327, 1014-1018

51. Thompson, J. M., Sgourakis, N. G., Liu, G., Rossi, P., Tang, Y., Mills, J. L., Szyperski, T., Montelione, G. T., and Baker, D. (2012) Accurate protein structure modeling using sparse NMR data and homologous structure information. Proc.Natl.Acad.Sci.U.S.A. 109, 9875–9880

52. Shen, Y., Lange, O., Delaglio, F., Rossi, P., Aramini, J.M., Liu, G., Eletsky, A., Wu, Y., Singarapu, K.K., Lemak, A., Ignatchenko, A., Arrowsmith, C.H., Szyperski, T., Montelione, G.T., Baker, D., and Bax, A. (2008) Consistent blind protein structure generation from NMR chemical shift data. Proc.Natl.Acad.Sci.U.S.A. 105, 4685-4690

53. Zong, X., Krause, S., Chen, C.C., Kruger, J., Gruner, C., Cao-Ehlker, X., Fenske, S., Wahl-Schott, C., and Biel, M. (2012) Regulation of hyperpolarization-activated cyclic nucleotide-gated (HCN) channel activity by cCMP. J.Biol.Chem. 287, 26506-26512

54. Shi, L., Traaseth, N.J., Verardi, R., Gustavsson, M., Gao, J., and Veglia, G. (2011) Paramagnetic-based NMR restraints lift residual dipolar coupling degeneracy in multidomain detergent-solubilized membrane proteins. J.Am.Chem.Soc. 133, 2232-2241

55. Tonelli, M., Masterson, L.R., Cornilescu, G., Markley, J.L., and Veglia, G. (2009) One-sample approach to determine the relative orientations of proteins in ternary and binary complexes from residual dipolar coupling measurements. J.Am.Chem.Soc. 131, 14138-14139

56. Zhou, L., and Siegelbaum, S.A. (2007) Gating of HCN channels by cyclic nucleotides: residue contacts that underlie ligand binding, selectivity, and efficacy. Structure. 15, 655-670

57. Zhou, L., Olivier, N.B., Yao, H., Young, E.C., and Siegelbaum, S.A. (2004) A conserved tripeptide in CNG and HCN channels regulates ligand gating by controlling C-terminal oligomerization. Neuron. 44, 823-834

58. Ulens, C., and Siegelbaum, S.A. (2003) Regulation of hyperpolarization-activated HCN channels by cAMP through a gating switch in binding domain symmetry. Neuron. 40, 959-970

59. Flynn, G.E., Black, K.D., Islas, L.D., Sankaran, B., Zagotta, W.N. (2007) Structure and rearrangements in the carboxy-terminal region of SpIH channels. Structure 15(6):671-82.

60. Bruystens, J.G., Wu, J., Fortezzo, A., Kornev, A.P., Blumenthal, D.K., and Taylor, S.S. (2014) PKA RIalpha homodimer structure reveals an intermolecular interface with implications for cooperative cAMP binding and Carney complex disease. Structure. 22, 59-69

61. Ilouz, R., Bubis, J., Wu, J., Yim, Y.Y., Deal, M.S., Kornev, A.P., Ma, Y., Blumenthal, D.K., and Taylor, S.S. (2012) Localization and quaternary structure of the PKA RIbeta holoenzyme. Proc.Natl.Acad.Sci.U.S.A. 109, 12443-12448

62. Masterson, L.R., Cheng, C., Yu, T., Tonelli, M., Kornev, A., Taylor, S.S., and Veglia, G. (2010) Dynamics connect substrate recognition to catalysis in protein kinase A. Nat.Chem.Biol. 6, 821-828

63. Masterson, L.R., Shi, L., Metcalfe, E., Gao, J., Taylor, S.S., and Veglia, G. (2011) Dynamically committed, uncommitted, and quenched states encoded in protein kinase A revealed by NMR spectroscopy. Proc.Natl.Acad.Sci.U.S.A. 108, 6969-6974

64. Anand, G.S., Krishnamurthy, S., Bishnoi, T., Kornev, A., Taylor, S.S., and Johnson, D.A. (2010) Cyclic AMP- and (Rp)-cAMPS-induced conformational changes in a complex of the catalytic and regulatory (RI{alpha}) subunits of cyclic AMP-dependent protein kinase. Mol.Cell.Proteomics. 9, 2225-2237

65. Kelkar, D.S., Kumar, D., Kumar, P., Balakrishnan, L., Muthusamy, B., Yadav, A.K., Shrivastava, P., Marimuthu, A., Anand, S., Sundaram, H., Kingsbury, R., Harsha, H.C., Nair, B., Prasad, T.S., Chauhan, D.S., Katoch, K., Katoch, V.M., Kumar, P., Chaerkady, R., Ramachandran, S., Dash, D., and Pandey, A. (2011) Proteogenomic analysis of Mycobacterium tuberculosis by high resolution mass spectrometry. Mol.Cell.Proteomics. 10, M111.011627

66. Huang, G.Y., Kim, J.J., Reger, A.S., Lorenz, R., Moon, E.W., Zhao, C., Casteel, D.E., Bertinetti, D., Vanschouwen, B., Selvaratnam, R., Pflugrath, J.W., Sankaran, B., Melacini, G., Herberg, F.W., and Kim, C. (2014) Structural basis for cyclic-nucleotide selectivity and cGMP-selective activation of PKG I. Structure. 22, 116-124

67. McNicholl, E.T., Das, R., SilDas, S., Taylor, S.S., and Melacini, G. (2010) Communication between tandem cAMP binding domains in the regulatory subunit of protein kinase A-Ialpha as revealed by domain-silencing mutations. J.Biol.Chem. 285, 15523-15537

68. Das, R., Chowdhury, S., Mazhab-Jafari, M.T., Sildas, S., Selvaratnam, R., and Melacini, G. (2009) Dynamically driven ligand selectivity in cyclic nucleotide binding domains. J.Biol.Chem. 284, 23682-23696

69. Abu-Abed, M., Das, R., Wang, L., and Melacini, G. (2007) Definition of an electrostatic relay switch critical for the cAMP-dependent activation of protein kinase A as revealed by the D170A mutant of RIalpha. Proteins. 69, 112-124

70. Selvaratnam, R., Mazhab-Jafari, M.T., Das, R., and Melacini, G. (2012) The auto-inhibitory role of the EPAC hinge helix as mapped by NMR. PLoS One. 7, e48707

71. Selvaratnam, R., Akimoto, M., VanSchouwen, B., and Melacini, G. (2012) cAMP-dependent allostery and dynamics in Epac: an NMR view. Biochem.Soc.Trans. 40, 219-223

72. Vanschouwen, B., Selvaratnam, R., Fogolari, F., and Melacini, G. (2011) Role of dynamics in the auto-inhibition and activation of the exchange protein directly activated by cyclic AMP (EPAC). J.Biol.Chem. 286, 42655-42669.

73. Gavina, J.M., Mazhab-Jafari, M.T., Melacini, G., and Britz-McKibbin, P. (2009) Label-free assay for thermodynamic analysis of protein-ligand interactions: a multivariate strategy for allosteric ligand screening. Biochemistry. 48, 223-225

74. Das, R., Mazhab-Jafari, M.T., Chowdhury, S., SilDas, S., Selvaratnam, R., and Melacini, G. (2008) Entropy-driven cAMP-dependent allosteric control of inhibitory interactions in exchange proteins directly activated by cAMP. J.Biol.Chem. 283, 19691-19703

75. Rehmann, H., Wittinghofer, A., and Bos, J.L. (2007) Capturing cyclic nucleotides in action: snapshots from crystallographic studies. Nat.Rev.Mol.Cell Biol. 8, 63-73

76. Schunke, S., Stoldt, M., Lecher, J., Kaupp, U.B., and Willbold, D. (2011) Structural insights into conformational changes of a cyclic nucleotide-binding domain in solution from Mesorhizobium loti K1 channel. Proc.Natl.Acad.Sci.U.S.A. 108, 6121-6126

77. Nussinov, R. (2013) The spatial structure of cell signaling systems. Phys.Biol. 10, 045004

78. Nussinov, R., Tsai, C.J., and Csermely, P. (2011) Allo-network drugs: harnessing allostery in cellular networks. Trends Pharmacol.Sci. 32, 686-693

79. Nussinov, R., Tsai, C.J., and Ma, B. (2013) The underappreciated role of allostery in the cellular network. Annu.Rev.Biophys. 42, 169-189

80. Boulton, S., Akimoto, M., Vanschouwen, B., Moleschi, K., Selvaratnam, R., Giri, R., and Melacini, G. (2014) Tapping the translation potential of cAMP signalling: molecular basis for selectivity in cAMP agonism and antagonism as revealed by NMR. Biochem.Soc.Trans. 42, 302-307

81. Ming, D. and Brüschweiler, R. (2004) Prediction of methyl-side chain dynamics in proteins. J. Biomol. NMR 29, 363-368

82. Shen, Y., Delaglio, F., Cornilescu, G., and Bax, A. (2009) TALOS+: A hybrid method for predicting protein backbone torsion angles from NMR chemical shifts. J. Biomol. NMR 44, 213-223

Chapter 5

Conclusions and Future Perspectives

5.1 Characterization of Functional PKA RIα Linkers

When allostery arises from structural as opposed to purely dynamic changes, the comparison of active and inactive structures reveals the network of residues mediating the allosteric propagation of the signal carried by the allosteric effector. Although this approach is highly informative for well-folded domains, limitations are encountered when allostery involves protein regions that are flexible and only partially structured. This is often the case for inter-domain linkers, where critical functional sites are frequently located. In PKA the key inhibitory element is composed of a N-terminal linker followed by CBD-A, which is in turn connected through another linker to a C-terminal tandem CBD (*i.e.* CBD-B) functioning as the gate keeper domain for access of cAMP to CBD-A. Chapters 2 and 3 of this thesis focused on these two different linkers of PKA RIα. In Chapter 2 we demonstrated that the N-terminal linker followed by CBD-A is flexible, but controls the CBD-A through state selective interactions. The

state selectivity of the linker-CBD interaction was confirmed through four independent methods, *i.e.* CHESCA, PREs, unfolding experiments and mutations monitored by kinase assays. Another notable conclusion of Chapter 2 is that, although weak, the interactions elicited by flexible linkers are amplified by the near degeneracy of the free energy landscape of CBD-A in apo RIα, which samples both active and inactive conformers in agreement with a conformational selection model. In Chapter 3 we showed that, unlike the linker N-terminal to CBD-A, the linker N-terminal to CBD-B does not contribute to the conformational selection in CBD-B. However, this linker plays a central role in the full activation of PKA as this linker spans mutually exclusive binding region, *i.e.* the PKA C-subunit binding region and the inter-CBD region.

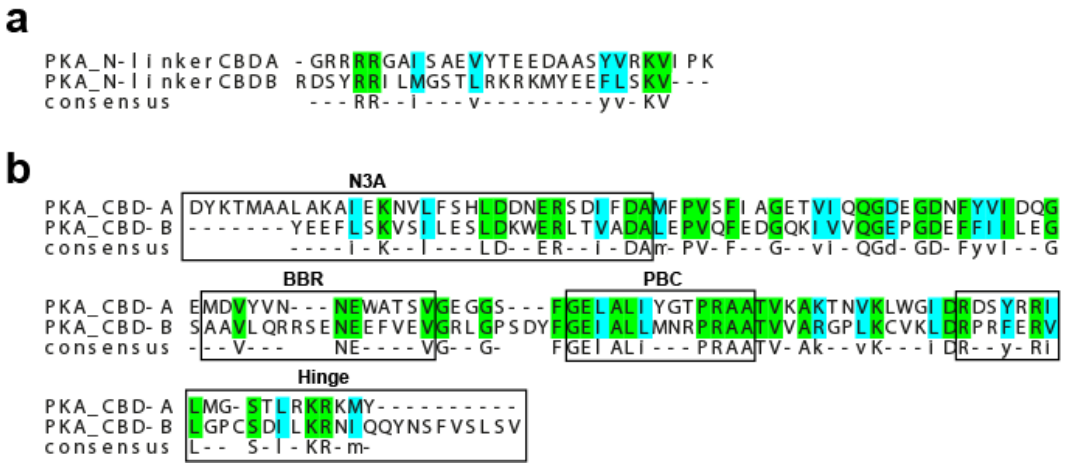

Figure 1: Sequence alignment of PKA Linkers (a) and CBD-A vs. CBD-B (b). The green color represents highly conserved residues, while cyan denotes similar residues analyzed with CLUSTALW.

The sequence analysis of the PKA RIα linkers reveals common motifs in their amino acid composition. For example, the linkers exhibit similar numbers of positive and negative charged residues and show similar isoelectric points (PI) of 9.98 *vs*. 10.52 and hydrophobicity profiles.

However, they are not highly homologous based on the primary sequence analysis (Figure 1a). Hence, even though they are both classified as “linkers”, the character of each linker is markedly different. This implies that the role of linkers cannot be predicted solely based on their amino acid composition or the length of the linker. The interaction with structured domains is another key determinant of the allosteric role of linkers. Moreover, the sequence identity and homology of the whole CBD-A and CBD-B are limited to 37% and 53%, respectively (Figure 1b), and such inter-CBD differences can further contribute to the different roles of CBD-interacting linkers.

5.2 Comparative Analysis of Functional Linkers in PKA *vs.* HCN

The central question addressed by this thesis is how does cAMP-binding to a folded domain (CBD) result in the control of functional sites in an adjacent mostly unstructured linker. As discussed above Chapters 2 and 3 address this question for the linkers N-terminal to PKA CBD-A and CBD-B, respectively, while Chapter 4 addresses this question for the linker N-terminal to the HCN CBD. For these three types of linkers, we show that cAMP controls function by promoting at least partial structuring in the adjacent N-terminal region. This occurs in the first place by cAMP selectively stabilizing the active *versus* inactive state of the CBD due to the cAMP-selectivity for the former state. In the second place, once the active CBD state is stabilized, the resulting stabilization of the adjacent linker is modelled by the allosteric thermodynamic cycle for the linker - CBD coupling shown in Figure 2. It should be noted that in Figure 2, the definition of “structured linker” is different in HCN *vs.* PKA. For HCN, “structured

linker" means a linker in a folded tetramer, while for PKA "structured linker" denotes a monomeric linker but interacting with the adjacent domain.

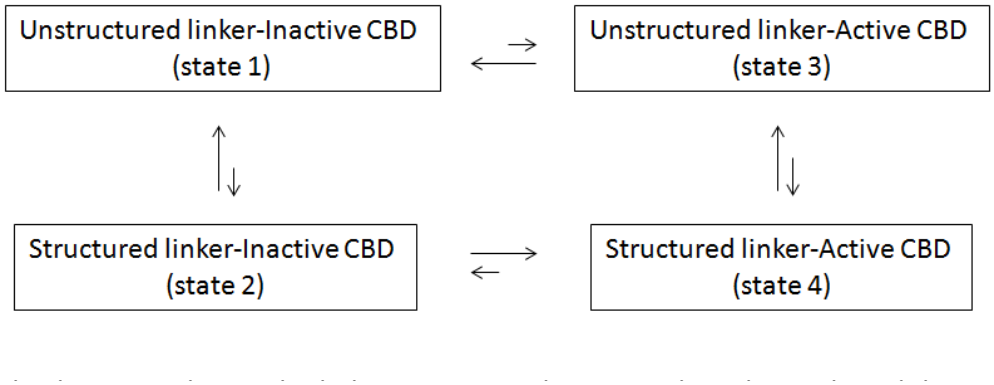

Figure 2: Simplified four-state thermodynamic cycle for the allosteric control of linkers by the adjacent CBDs. The arrows denote dynamic conformational equilibria.

In both HCN and PKA, the linker - CBD coupling arises by selectively stabilizing the diagonal states (i.e. 1 & 4) *vs*. the anti-diagonal states (i.e. 2 & 3). However, the mechanism underlying the selective stabilization of states 1 & 4 *vs*. 2 & 3 is different in HCN and PKA. In the case of PKA, this is achieved by the preferential interaction of the linker with the active *vs*. inactive state of the adjacent domain, resulting in a lower free energy of states 1 & 4 *vs*. 2 & 3, respectively. In the case of HCN, states 2 and 3 are destabilized relative to the other states by either steric clashes (state 2) or the intrinsic tendency of the linker to form structured tetramers (state 3). So in both HCN and PKA, states 1 & 4 exhibit lower free energy than 2 & 3, respectively, but for PKA this is mainly the result of selectively stabilizing 1 & 4, while for HCN this is mainly the result of selectively destabilizing 2 & 3. In conclusion, PKA and HCN exhibit similar net results in terms of free energy differences, but different underlying structural mechanisms. This model focuses mainly on the primary mechanism at play in each system, and it should be noted that currently we cannot rule out the presence of secondary linker-control

mechanisms (e.g. PKA-like mechanism for HCN or HCN-like mechanism for PKA). In addition, the primary mechanism outlined by the thermodynamic cycle above may not be specific for cAMP-receptors and apply to other systems (1-3) different from HCN and PKA.

5.3. New open questions and leads

The work presented in this thesis may have implications for both our basic understanding of allostery and the pharmacology of cAMP signaling. The understanding of the conformational switches that control HCN and PKA helped define general concepts and paradigms for how small ligands control protein-protein interfaces. In addition, the comparative analysis of the key eukaryotic cAMP receptors analyzed in this thesis will facilitate the design of novel highly selective cAMP-analogs with therapeutic potential for cardiovascular, metabolic and neurological disorders. For example, in the following sections we provide preliminary data to show how cAMP analogs can be exploited for selective CBD inhibition.

5.3.1 Interaction between Cyclic-di-NMPs and HCN4

Cyclic-di-nucleotide monophosphates (c-di-NMPs) were first found at concentrations of 5–10 μM in bacterial species, where they have been reported to serve as pivotal bacterial second messengers, regulating cellulose biosynthesis, bacterial growth, cellular adhesion, cell-surface interactions and biofilm formation (4-6). However, c-di-NMPs have recently been shown to participate in mammalian signaling pathways as well (7). In humans, c-di-NMPs, which are either produced endogenously in response to foreign DNA or derived from bacterial

infections, bind the trans-membrane protein STING (stimulator of interferon genes) and trigger the innate immune system by activating the expression of interferon genes (7). In addition, in 2014 Lolicato et al. reported that c-di-NMPs directly bind the tetramerization region of HCN4 and are potent inhibitors of HCN4 modulation by cAMP (8). This implies that the c-di-NMPs may work not only as a host defense trigger, but also as effector molecules in mammalian signaling systems. However, the structural and energetic basis for the binding of c-di-NMPs to HCN4 is currently unknown.

In order to understand how c-di-NMPs bind HCN4, we have expressed and characterized the tetramerization region of HCN4 (HCN4 A'-D'). We also examined the binding of c-di-GMP to this construct. HCN4 A'-D', *i.e.* HCN4 (521-588), was expressed and purified similarly to the HCN4 constructs used in Chapter 4. Size exclusion chromatography analysis (Superdex200) showed that HCN A'-D' elutes earlier at higher concentrations (Table 1), suggesting that HCN A'-D' forms oligomers in solution.

Table 1: Analytical Size Exclusion Chromatography profile of HCN4 (521-588)

Injection conc (mg/ml)	0.5	1.0	5.0
Elution volume (ml)	18.18	18.03	17.52

We then acquired HN-HSQC spectra of HCN4 A'-D' in the absence and presence of c-di-GMP to map at residue resolution the effect of c-di-GMP binding. The apo *vs.* holo HSQC comparison revealed dramatic changes in intensity and also minor chemical shift changes (Figure 3a). This result is consistent with c-di-GMP binding the HCN4 tetramerization region (HCN4 A'-D'). The Saturation Transfer Difference (STD) spectra also confirmed the binding of

c-di-GMP in HCN4 A'-D' (Figure 3b), however it is possible that c-di-GMP binds self-associated forms of HCN4 A'-D' (*e.g.* dimers or tetramers). Since Lolicato et al. reported that the binding of c-di-GMP inhibits the activation of HCN4 channels by cAMP, this tetramerization region could serve as a new drug target in future. In addition, HCN4 A'-D' would be a useful tool for further analyses, as it still preserves similarities to full length HCN in terms of oligomerization and c-di-GMP binding.

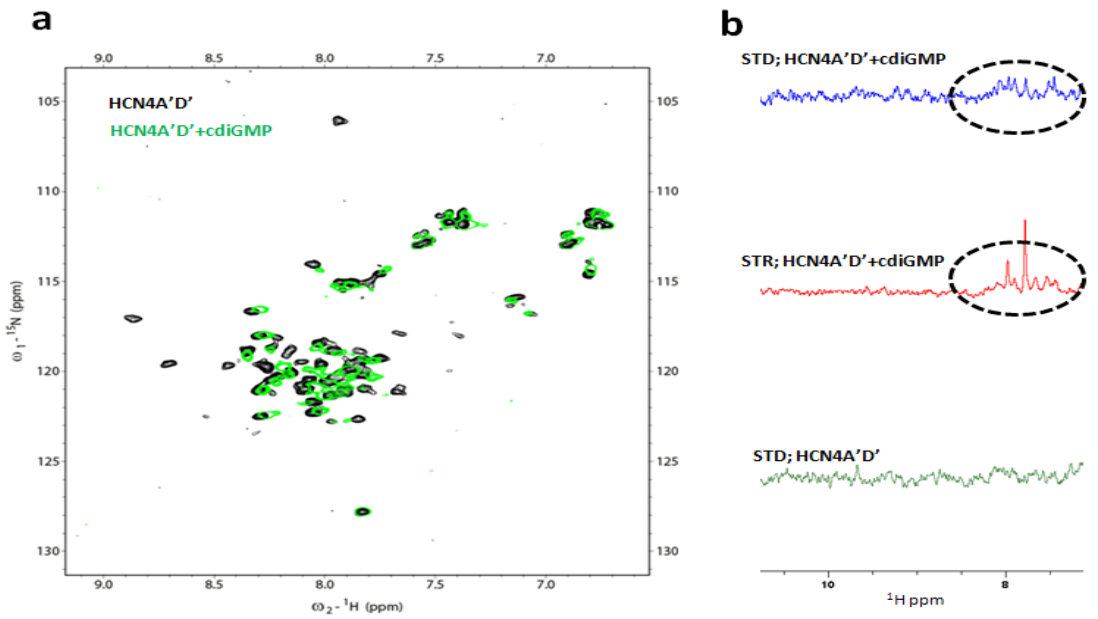

Figure 3: Binding of c-di-GMP to HCN4 A'-D'**a)** $^{1}H^{15}N$ HSQC spectra of 0.1 mM HCN4 A'-D' acquired in the absence (black) and presence (green) of 0.5mM c-di-GMP**. b)** Saturation Transfer Difference (STD) and STR with c-di-GMP.

5.3.2 Rp-cAMPS and PKA interaction

Structures of several end-point conformations of PKA RIα have been solved by X-ray crystallography (9,10). These structures have provided molecular insights into the cAMP binding pocket and R-C interface, as well as provided details of the distinct active and inactive-conformational states. However a structural basis for Rp-cAMPS functioning as an

inverse agonist and mechanistic details of cAMP-dependent activation of PKA, specifically by mediating conversion of the holoenzyme (H) to the cAMP-bound (B) conformation are still unclear. For example, the crystal structure of CBD-A bound to Rp-cAMPS is similar to the H-state (11), while the crystal structure of the two-domain construct CBD-A-B bound to Rp-cAMPS resembles the B-state (12). Moreover, Rp-cAMPS acts as antagonist in full length R with kinase assay, but in the absence of Mg^{2+} and ATP, Rp-cAMPS acts as an agonist (13). Considering that Rp-cAMPS is the only known antagonist of PKA, it is essential to understand the mechanism of action of Rp-cAMPS, which is an allosteric kinase inhibitor as it does not bind the PKA catalytic subunit (C) but only the C-bound regulatory subunit (R). We plan to use the CHESCA method and our findings in Chapter 3 to understand the agonism and antagonism mechanism of Rp-cAMPS.

5.4 References:

1. Kanelis, V., R.P. Hudson, P.H. Thibodeau, P.J. Thomas, and J.D. Forman-Kay. 2010. NMR evidence for differential phosphorylation-dependent interactions in WT and DeltaF508 CFTR. EMBO J. 29: 263–77.

2. López-Alonso, J.P., E.D. de Araujo, and V. Kanelis. 2012. NMR and fluorescence studies of drug binding to the first nucleotide binding domain of SUR2A. Biochemistry. 51: 9211–22.

3. Mazhab-Jafari, M.T., C.B. Marshall, M.J. Smith, G.M.C. Gasmi-Seabrook, P.B. Stathopulos, F. Inagaki, L.E. Kay, B.G. Neel, and M. Ikura. 2015. Oncogenic and RASopathy-associated K-RAS mutations relieve membrane-dependent occlusion of the effector-binding site. Proc. Natl. Acad. Sci. U. S. A. 112: 6625–30.

4. Römling, U., and D. Amikam. 2006. Cyclic di-GMP as a second messenger. Curr. Opin. Microbiol. 9: 218–28.

5. Römling, U., M. Gomelsky, and M.Y. Galperin. 2005. C-di-GMP: the dawning of a novel bacterial signalling system. Mol. Microbiol. 57: 629–39.

6. Ross, P., R. Mayer, and M. Benziman. 1991. Cellulose biosynthesis and function in bacteria. Microbiol. Rev. 55: 35–58.

7. Danilchanka, O., and J.J. Mekalanos. 2013. Cyclic dinucleotides and the innate immune response. Cell. 154: 962–70.

8. Lolicato, M., A. Bucchi, C. Arrigoni, S. Zucca, M. Nardini, I. Schroeder, K. Simmons, M. Aquila, D. DiFrancesco, M. Bolognesi, F. Schwede, D. Kashin, C.W.G. Fishwick, A.P. Johnson, G. Thiel, and A. Moroni. 2014. Cyclic dinucleotides bind the C-linker of HCN4 to control channel cAMP responsiveness. Nat. Chem. Biol. 10: 457–62.

9. Su, Y., W.R. Dostmann, F.W. Herberg, K. Durick, N.H. Xuong, L. Ten Eyck, S.S. Taylor, and K.I. Varughese. 1995. Regulatory subunit of protein kinase A: structure of deletion mutant with cAMP binding domains. Science. 269: 807–813.

10. Kim, C., C.Y. Cheng, S.A. Saldanha, and S.S. Taylor. 2007. PKA-I holoenzyme structure reveals a mechanism for cAMP-dependent activation. Cell. 130: 1032–1043.

11. Badireddy, S., G. Yunfeng, M. Ritchie, P. Akamine, J. Wu, C.W. Kim, S.S. Taylor, L. Qingsong, K. Swaminathan, and G.S. Anand. 2011. Cyclic AMP analog blocks kinase activation by stabilizing inactive conformation: conformational selection highlights a new concept in allosteric inhibitor design. Mol. Cell. Proteomics. 10: M110.004390.

12. Wu, J., J.M. Jones, X. Nguyen-Huu, L.F. Ten Eyck, and S.S. Taylor. 2004. Crystal structures of RIalpha subunit of cyclic adenosine 5’-monophosphate (cAMP)-dependent protein kinase complexed with (Rp)-adenosine 3',5'-cyclic monophosphothioate and (Sp)-adenosine 3',5'-cyclic monophosphothioate, the phosphothioate analogues of cA. Biochemistry. 43: 6620–6629.

13. Dostmann, W.R., and S.S. Taylor. 1991. Identifying the molecular switches that determine whether (Rp)-cAMPS functions as an antagonist or an agonist in the activation of cAMP-dependent protein kinase I. Biochemistry. 30: 8710–8716.